PLANAR SEMICONDUCTOR NANOWIRES ON HIGH-INDEX SUBSTRATES

This thesis has been submitted
by
GUNJAN NAGDA
to
The PhD school of the Faculty of Science
University of Copenhagen

Center for Quantum Devices
Copenhagen, Denmark
April 2023

THESIS ADVISOR:
Prof. Jesper Nygård
CO-SUPERVISORS:
Prof. Thomas Sand Jespersen
Dr. Daria V. Beznasyuk

[...] elementary does not mean easy to understand.
Elementary means that very little is required to know
ahead of time in order to understand it,
except to have an infinite amount of intelligence.

— Richard Feynman

Summary

Engineering materials especially at the nanoscale plays an important role in the development of quantum technologies. To that effect, in-plane selective area growth (SAG) of III-V nanowires (NWs) is a scalable and versatile materials platform that holds great promise for nanoelectronics and photonics applications. However, achieving the requisite material characteristics demands a meticulous optimization of the crystal quality. This critical aspect cannot be overlooked, given the significant impact it has on device performance and functionality. As such, crystal quality optimization through in-plane SAG has become a topic of keen research interest in the scientific community, as it holds the potential to unlock novel and exciting applications.

The first part of the thesis gives a brief introduction to the concepts of crystal growth associated with the work in this thesis along with experimental methods implemented. This includes a description of the crystal symmetry, adatom kinetics to be considered during SAG and resulting crystal shapes. The methods of SAG substrate fabrication, atomic force microscopy (AFM), molecular beam epitaxy (MBE) and electron microscopy are briefly explained.

The second part of this thesis presents the study of MBE grown GaAs NW arrays on GaAs substrates. For GaAs homo-epitaxy, the effect of in-plane alignment is studied. The misalignment of SAG NWs as a result of the tolerances associated with substrate fabrication on the NW morphology is studied via AFM. The facet roughness of the NWs is used as a measure of the structural quality. The use of Sb as a surfactant during GaAs growth is found to have no effect on the nominally aligned NWs, however, it is found that reducing the NW length allows for accommodating a small degree of misalignment. Further, the possibility of engineering the cross-sectional shapes of GaAs NWs by choice of substrate in-plane and out-of-plane orientations is presented. To that effect, novel high-index substrates such as $(2\,1\,1)$ and $(3\,1\,1)$ have been used to grow the NWs. It is found that the polarity of the substrate, use of Sb as a surfactant and varying SAG mask dimensions can also modify the NW shape in some cases. This opens up the possibility to obtain NWs with desired combinations of facets and corresponding shapes.

The third part of the thesis presents hetero-epitaxy of InAs/GaAs NWs grown on $(3\,1\,1)$A substrates. The structural reproducibility of these NWs across very large arrays has been quantified by performing AFM on 180 NWs. Varying the growth time and the SAG mask dimensions results in a variety of NW morphologies. The effect of

intentional in-plane misalignment on the NW morphology is also studied and found to change with varying NW width. The NW morphologies obtained via AFM are also supplemented with electron microscopy methods to analyze the crystal quality and the In and Ga composition for select dimensions. Finally, the observed structural reproducibility is substantiated by electrical transport measurements on NW based field effect transport (NWFET) devices fabricated in a large scale multiplexer/de-multiplexer set-up operating at cryogenic temperatures. The set-up allows for addressing 128 individual nominally identical NWs on a single chip and requires 8192 NWFET devices to function. Additionally, using this set-up, measurements are also conducted on NWs with varying SAG mask dimensions and in-plane orientations and the resulting transport characteristics are found to be directly correlated with the structural and crystal quality of the NWs.

The final part consists of final remarks regarding the entirety of the thesis and presents some ideas for future exploration.

Resumé

Tekniske materialer, især på nanoskala, spiller en vigtig rolle i udviklingen af kvanteteknologier. Til den effekt er in-plane selektiv arealvækst (SAG) af III-V nanotråde (NW'er) en skalerbar og alsidig materialeplatform, der lover meget for nanoelektronik og fotonikapplikationer. Men opnåelse af de nødvendige materialeegenskaber kræver en omhyggelig optimering af krystalkvaliteten. Dette kritiske aspekt kan ikke overses, i betragtning af den betydelige indvirkning, det har på enhedens ydeevne og funktionalitet. Som sådan er optimering af krystalkvalitet gennem in-plane SAG blevet et emne med stor forskningsinteresse i det videnskabelige samfund, da det rummer potentialet til at låse op for nye og spændende applikationer.

Afhandlingens første del giver en kort introduktion til begreberne krystalvækst forbundet med arbejdet i dette speciale sammen med eksperimentelle metoder implementeret. Dette inkluderer en beskrivelse af krystalsymmetrien, adatomkinetikken, der skal tages i betragtning under SAG og resulterende krystalformer. Metoderne til SAG-substratfremstilling, atomkraftmikroskopi (AFM), molekylærstråleepitaksi (MBE) og elektronmikroskopi forklares kort.

Anden del af denne afhandling præsenterer studiet af MBE dyrkede GaAs NW arrays på GaAs substrater. For GaAs homo-epitaksi studeres effekten af in-plane alignment. Fejljusteringen af SAG NW'er som et resultat af tolerancerne forbundet med substratfremstilling på NW-morfologien studeres via AFM. Facetruheden af NW'erne bruges som et mål for den strukturelle kvalitet. Anvendelsen af Sb som et overfladeaktivt middel under GaAs-vækst har vist sig ikke at have nogen effekt på de nominelt justerede NW'er, men det har vist sig, at reduktion af NW-længden giver mulighed for at rumme en lille grad af fejljustering. Yderligere præsenteres muligheden for at konstruere tværsnitsformerne af GaAs NW'er ved valg af substrat i-plan og out-of-plan orientering. Til det formål er nye højindekssubstrater såsom (211) og (311) blevet brugt til at dyrke NW'erne. Det har vist sig, at polariteten af substratet, brug af Sb som overfladeaktivt middel og varierende SAG-maskedimensioner også kan modificere NW-formen i nogle tilfælde. Dette åbner mulighed for at opnå NW'er med ønskede kombinationer af facetter og tilsvarende former.

Den tredje del af afhandlingen præsenterer hetero-epitaxi af InAs/-GaAs NW'er dyrket på (311)A-substrater. Den strukturelle reproducerbarhed af disse NWs på tværs af meget store arrays er blevet kvantificeret ved at udføre AFM på 180 NWs. Variering af vækstiden og SAG-maskens dimensioner resulterer i en række NW-morfologier.

Effekten af tilsigtet in-plan misalignment på NW-morfologien er også undersøgt og fundet at ændre sig med varierende NW-bredde. NW-morfologierne opnået via AFM er også suppleret med elektronmikroskopimetoder for at analysere krystalkvaliteten og In- og Ga-sammensætningen for udvalgte dimensioner. Endelig er den observerede strukturelle reproducerbarhed underbygget af elektriske transportmålinger på NW-baserede felteffekttransportanordninger (NWFET) fremstillet i en storskala multiplexer/de-multiplexer-opsætning, der opererer ved kryogene temperaturer. Opsætningen giver mulighed for at adressere 128 individuelle nominelt identiske NW'er på en enkelt chip og kræver 8192 NWFET-enheder for at fungere. Ved hjælp af denne opsætning udføres der desuden målinger på NW'er med varierende SAG-maskedimensioner og in-plane orienteringer, og de resulterende transportegenskaber viser sig at være direkte korrelerede med NW'ernes strukturelle og krystalkvalitet.

Den sidste del består af afsluttende bemærkninger vedrørende hele afhandlingen og præsenterer nogle ideer til fremtidig udforskning.

Publications

The thesis incorporates the findings of publications/manuscripts [2] - [5], presented in a logical and comprehensive fashion. In certain instances where they offer the most appropriate explanation of the idea, some sections have been directly quoted or slightly altered from their original sources.

[1] Martin Espiñeira Cachaza, Anna Wulff Christensen, Daria Beznasyuk, Tobias Særkjær, Morten Hannibal Madsen, Rawa Tanta, **Gunjan Nagda**, Sergej Schuwalow, and Peter Krogstrup. "***Selective area growth rates of III-V nanowires***." In: *Phys. Rev. Mater.* 5.9 (Sept. 2021), p. 094601. ISSN: 2475-9953. DOI: 10.1103/PhysRevMaterials.5.094601.

[2] **Gunjan Nagda**, Daria V. Beznasyuk, Jesper Nygård, and Thomas Sand Jespersen. "***Effect of in-plane alignment on selective area grown homo-epitaxial nanowires***." In: *Nanotechnology* (Apr. 2023). ISSN: 0957-4484. DOI: 10.1088/1361-6528/acca27.

[3] Dāgs Olšteins, **Gunjan Nagda**, Damon J. Carrad, Daria V. Beznasiuk, Christian E. N. Petersen, Sara Martí-Sánchez, Jordi Arbiol, and Thomas Sand Jespersen. "***Cryogenic Multiplexing with Bottom-Up Nanowires***." In: *arXiv* (Apr. 2023). DOI: 10.48550/arXiv.2304.12765. eprint: 2304.12765.

[4] **Gunjan Nagda**, Dāgs Olšteins, Sara Martí-Sánchez, Daria V. Beznasiuk, Damon J. Carrad, Christian E. N. Petersen, Jesper Nygård, Jordi Arbiol, and Thomas Sand Jespersen. "***Dimension dependent electrical transport in planar InAs nanowires***." Manuscript in preparation.

[5] **Gunjan Nagda**, Daria V. Beznasiuk, Jesper Nygård, and Thomas Sand Jespersen. "***Shape engineering of in-plane semiconductor nanowires***." Manuscript in preparation.

Acknowledgments

I thank Peter Krogstrup for giving me the opportunity to work and live in this beautiful city, work in a beautiful lab with beautiful people. After an unconventional start at a lab situated away from QDev, amidst a global pandemic and difficult circumstances, I have managed to find my way to working with **Jesper Nygård**. I thank you for welcoming me into your wonderful group midway into my thesis, for always being available (even across countries), and for making me feel that what I do matters. Your guidance has helped me become a better scientist.

Thomas Sand Jespersen, you are an academic angel, I believe, sent specially to teach me (and every student who has and will have the chance to work with you) everything I have learnt in the 2 years that I have known you. From teaching me to value all data, to comfortably question everything, to think about the details, to then write about them in a pedagogical way and to always work at becoming a better scientist, you have been a ray of sunshine on the days that have felt darkest.

Daria Beznasyuk, you are a kind soul, who I have been lucky to work with, after moving to the world of nanowires. You have been by my side from the beginning, patiently taught me what I did not know, supported me through challenging times and 100% of the times made me feel better about failures, professionally and personally. Thank you for believing in me and also making me understand that if we try, we will always find an answer.

Dags Olsteins, collaborating with you solidified my confidence in the materials I grew. You have always patiently answered all my questions about statistics that I had supposedly learnt 10 years ago, showed me all the shortcuts in Illustrator and participated in my rants about most things. Your presence next door will be missed because I need to find another person who will answer my questions with your no-judgement approach.

Martin, Anna, Toby: thank you for always being willing to help and for sharing your infinite wisdom about SAG and for writing comprehensive theses that I have memorized by now. Cake Thursdays are still sorely missed.

Dorthe, Jeanette, Maria, Lena, Ingrid and Brian: I would like to thank all of you for making the most important part of this journey, also so seamless. There has never been a problem that you have not helped me with instantaneously.

Michaela, Alisa: It has been a pleasure to work alongside you. Your creativity and excitement for science is so inspiring. Life at QDev would have been quite dull without having you around. I hope to continue our friendship, no matter the distance.

Damon, Asbjørn, Joachim, Alex, Rasmus, Shiv: I see you as the veteran experts of QDev, who have infinite wisdom to share, if only someone asked. Often enough I have asked, and you have answered wisely. I aspire to have this wisdom some day. Thank you for always offering support no matter the problem I approached you with. I am glad to continue working alongside you, and thankful for your friendship.

Will, Oscar, Tsung-Lin, Fabrizio, Serwan: thank you for the conversations, where I always came out smarter at the other end.

Jennifer, Tommy, Judith, Sole: You have become my family away from family. My actual parents seem to think that you have adopted me and I think they are relived. (so am I)

Harry, Steffen, Zhenhai: I honestly do not think I could have survived this without you. You are the most wonderful and supportive colleagues, and somehow even better friends. I will forever be thankful that the universe conspired to bring you into my life (maybe Python gods were involved). Everyone deserves cheerleaders like you in their life, and I can only hope that I have been as good a friend to you as you have been to me. I love you.

Rikhav, Nisha, Rajal, Amarabati, Eric, Noel, Nishita, Krishna, Pooja: Our long distance relationship continues and I am so thankful to each and every one of you for your continued love, support, wisdom and empathy while I continue to be bad at responding to your texts, forgetting your birthdays and almost always only calling you because I have a problem or a joke so *specific* that no one else in this world would understand but you.

Daniel, wir haben schwierige Zeiten durchgemacht, aber das ändert nichts an dem Einfluss, den du auf mein Leben hattest. Danke.

Linnea, I thank you for the guidance and support you have provided me throughout our time together. Your insights and expertise have been invaluable in helping me navigate through some difficult times. I am so grateful to have had the opportunity to work with you and appreciate all that you have done for me.

Suman Ghosh, Dr. Shyamala Bodhane: thank you for fostering my curiosity when I was so young, you are the reason I am still studying, somewhat happily. I also thank **Thomas Schäpers**, who continued the fostering during my time in Jülich/Aachen.

Mummy, Pappa, Nanima, Masi, Veda, Masa, Mama, Nana: you are my world. This thesis would not have been possible without your infinite support, unconditional love and everlasting ability to motivate me. You made me who I am, and for that I will forever be grateful.

Contents

1

Introduction

In 1959, Richard Feynman delivered a lecture that would lay the foundation for the field of nanotechnology [1]. His words inspired a new era of research focused on understanding and manipulating matter at the atomic and molecular scale. Feynman's vision was clear: with unprecedented control over materials, revolutionary advancements in fields such as medicine, energy production, and electronics could be made possible.

Feynman's emphasis on materials science as a critical component of his vision cannot be overstated. It is through the study of materials that we investigate the properties and behaviors of substances and how they can be engineered to achieve specific functions. Alongside Moore's law [2], with the advent of nanotechnology, we are now able to manipulate materials at the atomic level [3] and even electronic level [4] to create entirely new ways to manipulate material properties.

Quantum materials research has become an exciting and rapidly growing field, with a multi-faceted interest. In quantum physics, nanomaterials are being used to create novel materials with unique electronic and optical properties. For instance, graphene, a two-dimensional material, has attracted significant attention due to its remarkable properties such as high mobility and tunable electronic properties [5]. Additionally, quantum dots have the potential to revolutionize the field of quantum computing due to their ability to trap individual electrons and control spin states [6]. A fundamental understanding of exotic states of matter [7] that can be tailored as a result of remarkable technological breakthroughs, is now possible and can help us better understand the basic principles of physics and chemistry governing matter at the nanoscale. There has also been a rampant increase towards applications to quantum information processing [8] and eventual integration with existing CMOS technology. In semiconducting engineering, the properties of nanomaterials can be finely tuned to develop new devices with improved efficiency, speed, and sensitivity. For example, carbon nanotubes are being studied for their potential to replace silicon in electronic devices [9] due to their high conductivity and flexibility and integration of more than $10,000$ devices in single functional chips has already been realized [10].

With an abundance of available materials and hardware platforms at our disposal [11], pushing the respective technologies towards their full potential in applicable settings demands a constant pursuit of breakthroughs and inventive approaches towards enhancing the very foundation of the materials that underpin them. Irrespective of the application, in order to realize the potential of quantum materials, demonstration of reproducibility and scalability of these materials is imperative, to ensure that the experiments designed to characterize the materials can be replicated by other researchers, confirming the validity and reliability of the findings. This makes the over-arching goal of enabling the development of practical applications and large-scale manufacturing and integration into useful inventions, more realistic.

1.1 Selective area grown materials: *State of the art*

The epitaxial growth of materials, in particular of III-V semiconductor nanostructures, from the bottom-up onto a host substrate represents a highly effective methodology for generating a diverse range of geometries, suitable for implementation in nanoscale electronic, photonic, and opto-electronic device applications. Figure 1.1 is adapted from a review about such applications based on selective area epitaxy of III-V semiconductors [18] and presents the multiple approaches to growth of nanostructures. The common approach is shown in Fig. 1.1a where a substrate of choice is processed via nano-fabrication techniques to host growth within pre-determined regions. The growth techniques, choice of materials and design decide the structural and transport characteristics of the resulting nanostructures, ranging from an array of out-of-plane vapor-solid-liquid (VLS) NWs to in-plane networks and junctions of NWs/nanosheets. Figure 1.1b shows scanning electron microscopy (SEM) micrographs from various published studies where selective area epitaxy was implemented to achieve nanostructures in specific geometries for various semiconductors. For in-plane epitaxy in most cases, the nanostructure geometry is associated with and limited by the crystal structure of the host substrate and the desired material to be grown, along with the symmetries associated, and correspondingly most arrows in the figure correspond to high-symmetry in-plane directions.

In the context of this thesis, the selective area growth of in-plane nanostructures will henceforth be referred to as SAG. SAG of III-V materials has thus far proven to be a flexible and a potentially scalable method for obtaining deterministic and reproducible in-plane NWs as a platform for nano-technologies [18]. In particular, SAG using molecular beam epitaxy (MBE), typically defined by lithographic techniques not only allows precise control of the position and size of NWs and the creation of large scale arrays and networks, but under

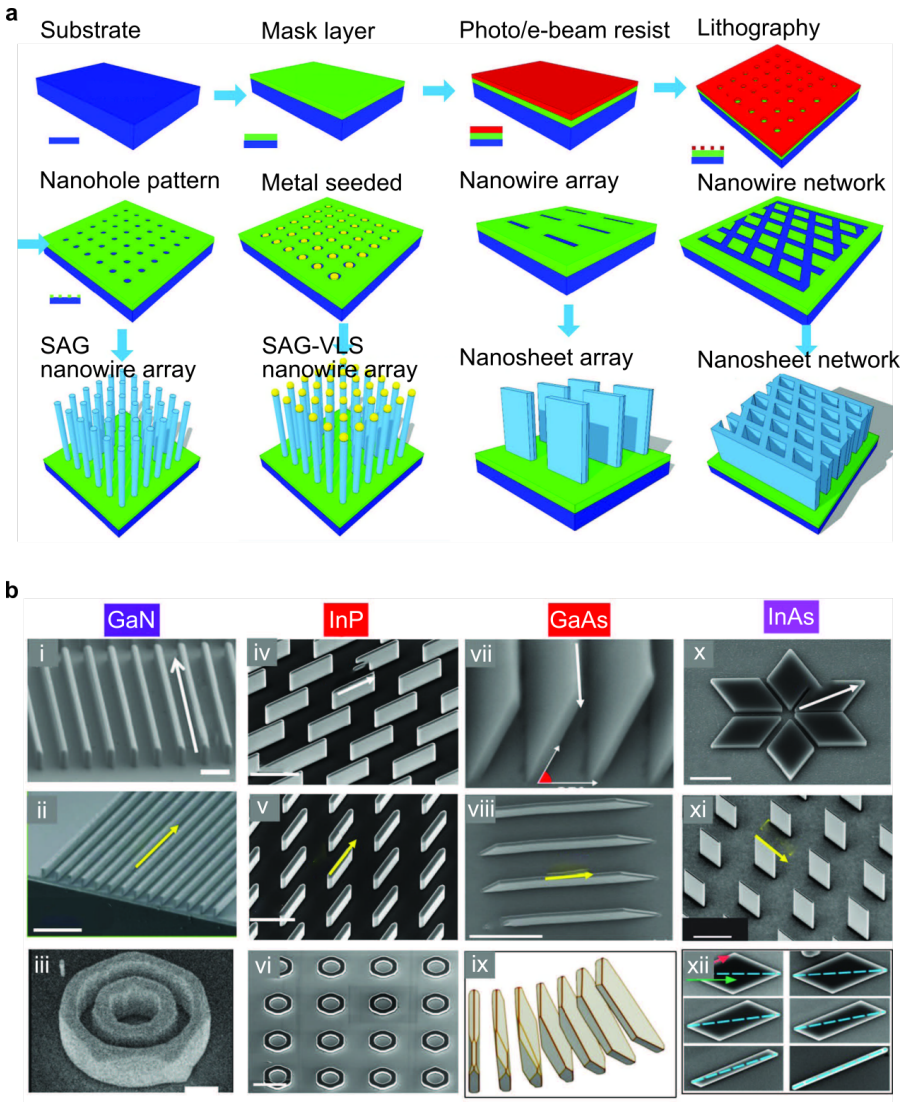

Figure 1.1: a A schematic illustration of steps involved in various ways of implementing selective area epitaxy of materials, resulting in growth of nanowire and nanosheet arrays and networks. **b** SEM micrographs of GaN [12, 13], InP [14], GaAs [15, 16] and InAs [17] nanostructures realized in various studies. Both sub-figures are adapted from Yuan *et al* [18].

optimized growth conditions, also results in a very high quality of said structures. Unlike conventional metal catalyzed VLS NWs, the SAG approach obviates time consuming and uncontrolled pick-and-place steps in device fabrication and enables large scale integration of nanostructures into complex device geometries [19].

The structural quality of SAG nanostructures depends on the substrate orientation [20], lattice mismatch between the substrate and the grown material [21], pre-growth substrate annealing methods [21], and the thermodynamics and kinetics during crystal growth [22]. SAG us-

ing MBE of semiconductors such as Si has already been reported four decades ago [23] and for GaAs SAG, facet formation and evolution on GaAs(0 1 1) [24, 25] has been studied and various models of growth mechanisms have been proposed [15, 22, 26, 27]. SAG of InAs NWs [20] and nanostructures [14] on InP substrates using chemical beam epitaxy has been reported, demonstrating different cross-sectional shapes and facets dependent on the substrate symmetry and growth parameters. InAs SAG NWs grown on surfactant mediated GaAs(Sb) [19] and/or InGaAs [21] buffer layers showed an enhanced crystal quality and improved electron mobility as compared to non-optimized crystals. However, formation of homogeneous group-III alloys still remains a challenge owing to facet dependent incorporation [28] and differing behaviour of group-III elements on the dielectric mask [22].

The effect of substrate fabrication related tolerances on the structural characteristics of the SAG NWs has not been reported yet. More importantly, the effect of structural disorder on the electrical transport is valuable information that allows for improving crystal growth for NW based devices. Although the correlation between structural disorder and electrical characteristics has not yet been quantified for SAG NWs, it is known that nanoscale changes in faceting of NWs modify the current density in NW devices [29]. Additionally, growth of subsequent transport-active InGaAs and InAs layers on such imperfect NWs will likely result in strain inhomogeneity locally within the crystal which has been reported to have a direct effect on the resistivity [30].

The effect of the using high-index substrates on the NW geometry has yet to be established. It is also not know whether the previously established growth parameters optimized for SAG on standard substrates, can be extended to other substrate orientations. The choice of using A- and B-polar substrates, combined with the effect of using Sb as a surfactant, also remains to be compared. Further, information about the composition and strain relaxation mechanism for the subsequent growth of ternany compounds such as InGaAs and heteroepitaxy of InAs on high-index substrates is also interesting to study for applications is electrical transport measurements.

The promise of scalability associated with SAG NWs and NW networks has not been demonstrated beyond a few proof-of-principle based experiments. It also remains to be verified whether NWs are indeed identical within large scale arrays despite the expected reproducibility of the SAG technique. Thus, there remain a multitude of challenges that need to be addressed based on the choice of material platform and associated applications. Perhaps more importantly, there also exist a multitude of unexplored avenues that could lead to better results.

1.2 Thesis objectives and organization

One of the main objectives of this thesis has been to investigate the use of high-index substrates for SAG of GaAs and InAs NWs using MBE. This included the use of GaAs substrates that are not commonly used for crystal growth, i.e., (211)A, (211)B, (311)A and (311)B. It is found that the use of this variety of substrates and choice of in-plane orientations along with the effect of surfactants during growth of GaAs NWs generates a matrix of cross-sectional shapes that are governed by their corresponding symmetries. The second objective was to study the effect of substrate fabrication related tolerances on the NW morphology. Even with the use of Sb as a surfactant during GaAs growth, it is found that NWs above a certain length exhibit steps on the facets as a result of mis-orientation with respect to the high-symmetry in-plane directions. The third main objective has been to demonstrate that the NWs grown using the SAG approach can be extended to very large arrays. Subsequent structural and electrical characterization of InAs NWs grown on GaAs buffer layers has been carried out by conducting AFM and by fabricating NW based field effect transistor devices that are measured at cryogenic temperatures, respectively. To that effect, the thesis is divided in 4 parts, arranged in the following way:

1. Background

   This part is divided into 2 chapters:

   a) Chapter 2 gives a brief introduction to most of the concepts required to understand the crystal synthesis in terms of the SAG approach. More specifically, the details of the kinetics to be considered during SAG of semiconductor NWs are presented. An understanding of the cross-sectional shape of the NWs as a result of the symmetries of the host substrate and the associated free surface energies is discussed.

   b) Chapter 3 gives an introductory understanding of the experimental techniques associated with the results obtained. A general method of substrate fabrication for SAG, basics of MBE growth and the primary characterization techniques such as atomic force microscopy (AFM) and electron microscopy are presented.

2. Homo-epitaxy of GaAs

   This part is divided into 2 chapters:

   a) Chapter 4 overlaps with Publication [2] [31]. It is based on a detailed study the effect of in-plane alignment of the GaAs SAG NWs grown on (211)B substrates. The origin

of fabrication related tolerances that impact the alignment of the NWs is addressed. The effect of the unintentional but unavoidable misalignment with respect to the high-symmetry in-plane directions on the NW morphology is measured using AFM. The structural quality is found to be dependent on the NW length for the nominally aligned NWs. The effect of Sb as a surfactant is tested. Material incorporation and facet evolution dependent on the in-plane alignment is also presented.

b) Chapter 5 demonstrates the varying cross-sectional shapes of GaAs NWs. This is achieved by the choice of substrate orientation, in-plane orientation as well as use of Sb as a surfactant. The effect of substrate out-of plane and in-plane orientations is found to be mostly governed by the crystal symmetries associated, whereas use of Sb as a surfactant is also found to affect NW faceting in some cases. Moreover, the choice of varying mask dimensions for any of the substrates allows to track an evolution of NW growth. AFM is used as the primary tool for structural characterization of NWs, with supplementary information from transmission electron microscopy for select NWs.

3. Hetero-epitaxy of InAs

This part is divided into 2 chapters:

a) Chapter 6 is a detailed study of the structural characteristics of InAs/GaAs(Sb) dual layers NWs grown on GaAs(3 1 1)A substrates. AFM is the primary tool to obtain NW topography from 180 nominally identical NWs to demonstrate the reproducibility of the NW geometry across a large array of NWs. Structural characteristics of NW with varying SAG mask dimensions such as 9 different widths and in-plane orientations are also quantified with the use of the topographical data. Misalignment from high symmetry in-plane orientations even on the order of 0.5° is found to have detrimental effect on the NW facet roughness. A select few NW dimensions are further studied using electron microscopy techniques to obtain information about the composition, strain relaxation and quality of the InAs/GaAs(Sb) interface.

b) Chapter 7 addresses the electrical transport characteristics of the InAs/GaAs(Sb) dual layer NWs grown on GaAs(3 1 1)A substrates discussed in the previous chapter. A multiplexer-de/multiplexer set-up is realized to enable large scale characterization of the NWs. The characteristics that define material quality such as electron mobility is extracted from

NW based field effect devices. The variation in device characteristics such as threshold voltage along with the mobility is presented with a statistical significance. Finally, measurements of field effect devices based on NWs with varying SAG mask dimensions shows a substantial correlation with the NW structure and crystal quality.

4. Final remarks

   This part contains the final chapter with concluding remarks from the entirety of the thesis. Some ideas based on the findings in this thesis are proposed as a follow-up to these experiments to understand the material properties better.

Part I

Background

This part presents the concepts of crystal growth to be considered in context with the selective area growth approach utilised in the experiments of this thesis. A complete description of semiconductor growth is not intended to be presented here due to the extensive nature of the topic. Instead, a guide to the necessary terminology and concepts required to interpret the results has been provided. A basic understanding of the experimental methods used is also presented.

2

Crystal Synthesis

III-V semiconductors are a family of materials made up of group III and group V elements that exhibit semiconducting properties. The two main crystal structures that these semiconductors show are space group F$\bar{4}$3m or commonly known as zincblende (ZB) and space group P63mc or commonly known as wurtzite (WZ). This chapter presents the details of the crystallographic structure, especially the high-index surfaces and the growth mechanisms to be considered for the synthesis of NWs shown in this thesis.

2.1 Crystal structure

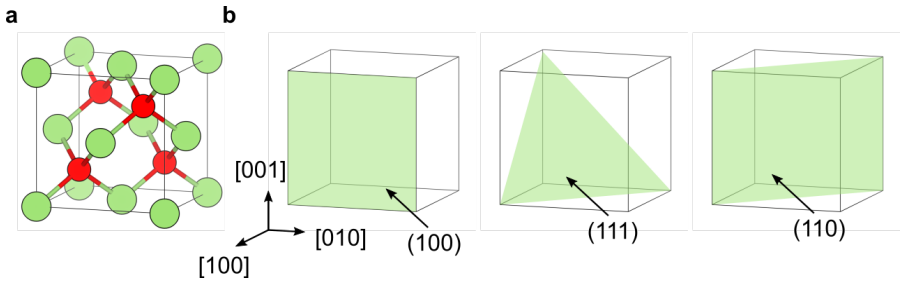

Figure 2.1: a Schematic representation of the zincblende (ZB) crystal structure. **b** Position of some important planes and their Miller indices for a cubic crystal structure.

The periodic arrangement of atoms in a crystal determines its crystal structure, and the smallest repeating group of atoms with all symmetry elements is the unit cell. There are seven fundamental lattice systems defined by the angle between their lattice directions and their relative size. The cubic system is the most symmetrical, with all angles between lattice parameters being 90°, and all lattice parameters having the same length. The bulk crystal structure of most III-V semiconductors is the zincblende (ZB) structure, except for some III-nitrides that have a different structure [32]. From Fig. 2.1a, the ZB structure can be visualized as two interpenetrating face-centered cubic (FCC) systems with the second lattice diagonally shifted along a quarter of the unit cell. It includes an extra atom at the center of each face of the unit cell, in addition to the atoms at the vertices. The atomic arrangement is equivalent to a dual base FCC diamond structure with carbon atoms substituted by group III (green) and group V (red) atoms. The schematic for the crystal structure was made using the software Vesta [33]. The name "zincblende" is derived from its archetype, ZnS. GaAs, InAs, InP and InSb are examples of group III-V compounds that have a ZB crystal structure.

Figure 2.1b highlights the position of some important planes within the ZB unit unit cell. Directions and planes in a crystal lattice are characterized by Miller indices, which are sets of integers. Crystal directions are written as whole number multiples $[h\,k\,l]$ of the lattice parameter and represent unit distances rather than actual distances. Crystal planes are written as $(h\,k\,l)$ and are defined by the orthogonal crystal direction $[h\,k\,l]$. Crystal directions and planes can be grouped into families written as $\langle h\,k\,l\rangle$ and $\{h\,k\,l\}$, respectively. The $\langle h\,k\,l\rangle$ family includes all directions with the same length, for e.g., $[1\,0\,0]$, $[0\,1\,0]$, and $[0\,0\,1]$, belong to the $\langle 1\,0\,0\rangle$ family of crystal directions. Similarly, the $\{h\,k\,l\}$ family includes all planes with the same defining crystal direction, such that $(1\,0\,0)$, $(0\,1\,0)$, and $(0\,0\,1)$ belong to the $\{1\,0\,0\}$ family of crystal planes.

2.2 High-index surfaces

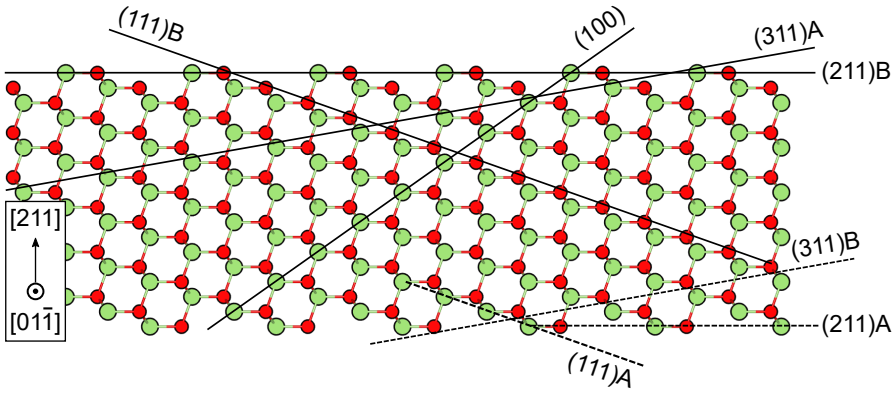

Figure 2.2: Ball and stick model of an ideal, bulk truncated GaAs crystal along the $[0\,1\,\bar{1}]$ direction. The lines indicate the $(1\,0\,0)$, $(1\,1\,1)$, $(2\,1\,1)$ and $(3\,1\,1)$ planes. Figure made using the software Vesta [33].

Figure 2.2 shows the atomic arrangement of an ideal, bulk truncated GaAs crystal along the $[0\,1\,\bar{1}]$ zone axis, with the $(1\,0\,0)$, $(1\,1\,1)$, $(2\,1\,1)$ and $(3\,1\,1)$ planes as labelled. The $(1\,1\,1)$ plane is a polar surface where the position of the Ga or As atom at the surface determines whether it is A- or B-polar, respectively. The $(2\,1\,1)$ surfaces contain equal number of Ga and As atoms and the Ga–As bond of the surface atoms is parallel to the surface. However, they derive their polarity from the nature of the atom with a broken bond in the second layer which is an As atom for $(2\,1\,1)$B (solid line at the top) and a Ga atom for $(2\,1\,1)$A (dashed line at the bottom). These atoms lie along the $(1\,1\,1)$ plane. Low energy electron diffraction (LEED) [34], scanning tunneling microscopy (STM) [35] and ab initio total-energy calculations using density functional theory [35, 36] all report that the $(2\,1\,1)$ surfaces are unstable even under surface reconstruction and instead exhibit facets, most commonly along the $\{1\,1\,0\}$, $\{1\,1\,1\}$ and $\{1\,1\,3\}$ planes. However, the faceting depends largely on the preparation conditions.

For $(3\,1\,1)$ surfaces on the other hand, the Ga–As bond of the surface atoms is titled. Therefore, there is a Ga atom in the topmost layer of the $(3\,1\,1)$A surface (solid line at the top) and an As atom for $(3\,1\,1)$B surface (dashed line at the bottom), making these surfaces polar too. Theoretical calculations unanimously conclude that the $(3\,1\,1)$A surfaces exhibit a very low surface energy under surface reconstruction and thus, are very stable [36, 37] along with experimental confirmation from STM and reflection high-energy electron diffraction (RHEED) [38]. $(3\,1\,1)$B surfaces are also found to be stable in some studies [39, 40].

2.3 Epitaxial interface

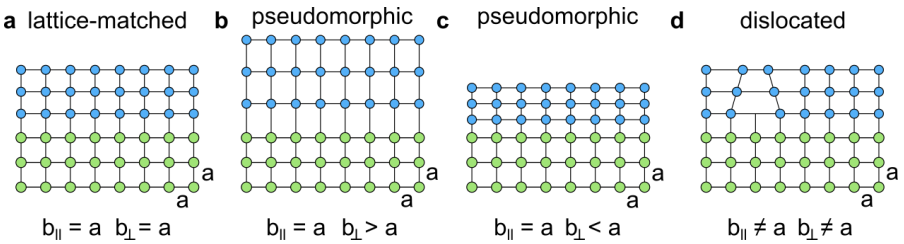

Figure 2.3: Schematic of a free standing crystalline structure consisting of two layers with a common interface: **a** A strain-free interface in the case of lattice-matched layers $a = b$. Pseudomorphic growth where elastic strain accommodate a small lattice-mismatch of either **b** $b_\perp \neq a$ or **c** $b_\parallel \neq a$. **d** Large lattice-mismatch induced formation of a misfit dislocation which results in broken atomic bonds as a strain minimization mechanism. Figure adapted from the book 'Epitaxy of Semiconductors' by Udo Pohl [41].

The growth of desired crystalline materials often requires a host substrate, which makes the study of epitaxial interfaces important. It is easier to create an epitaxial interface when two materials have similar crystal properties. However, due to factors such as lattice mismatch, diverging thermal-expansion coefficients, and differing crystal structures, materials usually do not match perfectly [42]. Figure 2.3 demonstrates the atomic arrangement at hetero-epitaxial interfaces of materials with increasing lattice-mismatch. The lattice mismatch f, is the relative difference between lattice constants of the two materials, usually expressed as

$$f = \frac{a - b}{a}$$

A strain-free interface can be formed in homo-epitaxy, and sometimes in hetero-epitaxy of well-matched materials, where the lattice constants of the combined materials are identical. However, in most cases, the lattice constants of two interfacing materials are different. Low levels of lattice mismatch can be accommodated by elastic strain (see Fig. 2.3b and c), where the epitaxial film deforms to match the lattice constant of the substrate. This can cause an opposing lattice distortion perpendicular to the interface to keep the unit cell volume constant. This type of growth is known as pseudomorphic.

As seen in Fig. 2.3d, as the lattice mismatch increases further, it is energetically favorable to form edge-type misfit dislocations, which break atomic bonds in exchange strain minimization [43]. As the film thickness of a material combination with a lattice mismatch increases, the strain energy also increases, eventually resulting in the formation of misfit dislocations [44, 45]. The critical thickness at

which plastic deformation occurs depends on the degree of lattice mismatch. Although the formation of misfit dislocations can relieve some of the strain, residual strain usually persists. In Chapter 6, results from hetero-epitaxy of InAs-GaAs have been presented, where there is a considerable lattice mismatch of $\sim 7.7\%$. As a result, all samples feature misfit dislocations near the interface due to the induced strain. Additionally, residual elastic strain dependent on the NW dimensions is also observed.

2.4 Fundamental growth modes

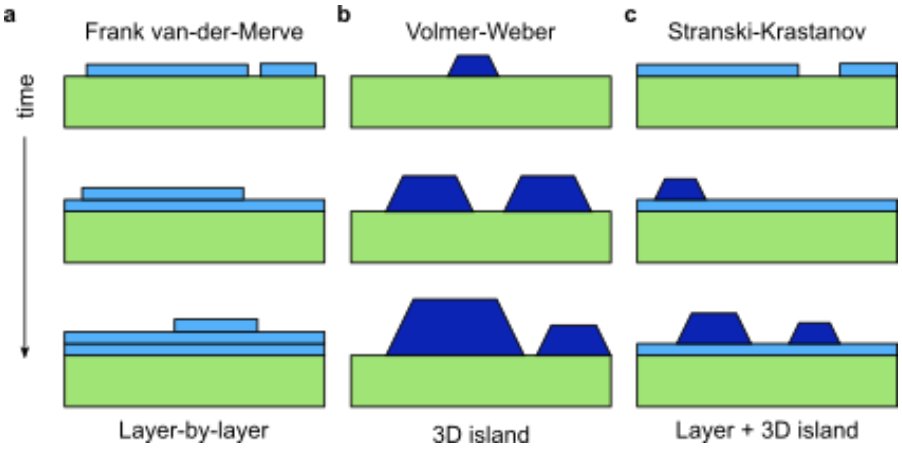

Figure 2.4: A schematic representation of the three fundamental growth modes are distinguished, each named after their original investigators. Figure adapted from the book 'Epitaxy of Semiconductors' by Udo Pohl [41].

The growth of crystalline thin films can occur in different modes, depending on the growth conditions and the properties of the material and substrate. This section provides a very basic introduction to the key differences across the different modes, primarily to introduce the terminology required to refer to results obtained in this thesis. Figure 2.4 shows a schematic of the three fundamental growth modes in epitaxy: 2D layer-by-layer growth (a), 3D island growth (b), and a mixed-mode growth (c).

2D layer-by-layer growth occurs when the adatoms (atoms or molecules that land on the substrate surface) diffuse and align with the crystal structure of the substrate. The adatoms attach to the substrate surface, and subsequently, more adatoms attach to the first layer, forming a continuous layer with an atomically flat surface. This mode is also known as the Frank-van der Merwe mode, and it occurs when the interfacial energy between the substrate and the deposited material is lower than the cohesive energy of the deposited material [46].

3D island growth mode occurs when the adatoms do not have a strong affinity to the substrate surface, and instead, they form three-dimensional clusters or islands on the substrate. The islands grow by absorbing more adatoms and coalescing with each other. This mode is also known as the Volmer-Weber mode, and it occurs when the interfacial energy between the substrate and the deposited material is larger than the cohesive energy of the deposited material [47].

Mixed-mode growth occurs when the growth mode switches from 2D layer-by-layer to 3D island growth as the thickness of the film increases. In the initial stages of growth, 2D layer-by-layer growth is dominant (also known as a wetting layer), however with increasing thickness, the built up strain within the film makes it energetically favorable for the adatoms to form islands instead of a continuous layer. The growth mode then transitions to 3D island growth. This mode is also known as Stranski-Krastanov growth, and it occurs when the interfacial energy between the substrate and the deposited material is close to the cohesive energy of the deposited material [48].

In terms of homogeneity, 2D layer-by-layer growth mode is preferable because it results in a continuous and uniform film with an atomically flat surface. This mode allows for the precise control of the film thickness and composition, which is essential for many applications in electronics and optoelectronics. However, incomplete wetting of the substrate by the film material is to be expected in almost every system [49]. On the other hand, 3D island growth mode and mixed-mode growth mode result in a non-uniform film with islands or clusters of different sizes and shapes. The film surface may also be rough due to the coalescence of the islands [50], unless a crystal re-orientation occurs during growth [51]. These modes are typically used to create nanostructures or to induce strain in the film, which can affect its physical and electronic properties. Therefore, the choice of growth mode depends on the specific application and the desired properties of the film [52]. If homogeneity is critical for the application, 2D layer-by-layer growth mode is preferred. However, mixed-mode growth has been successfully utilized for growth of self-assembled in-plane Ge NWs [53, 54].

2.5 Selective area growth

Selective area growth (SAG) is a promising growth technique that has been widely investigated due to its potential for control, scalability, and flexibility in growing large arrays and networks [19, 29, 55, 56]. Although the concept of SAG was first introduced decades ago [23, 24], it has recently gained renewed attention, due to the unique advantages it offers over other growth techniques, such as the ability to design and scale the structures grown. The SAG platform involves covering the growth substrate with an amorphous mask layer, such as SiO_2,

and opening windows selectively via electron beam lithography for growth to occur (details about substrate fabrication are presented in Section 3.1).

The SAG process relies on the principle of selectivity, where growth is maintained within the exposed regions of the substrate. Achieving complete selectivity is challenging, as it requires a delicate balance of desorption and surface diffusion on both the mask and the substrate. The range of parameters required for complete selectivity is referred to as the selectivity window, which imposes restrictions on the growth control parameter space. SAG utilizes an overpressure of the group V flux, limiting the growth by the group III flux and its kinetics. A comprehensive study has been performed to determine the selectivity window for GaAs [57, 58] and is an on-going process for different materials and smaller dimensions [55, 59, 60].

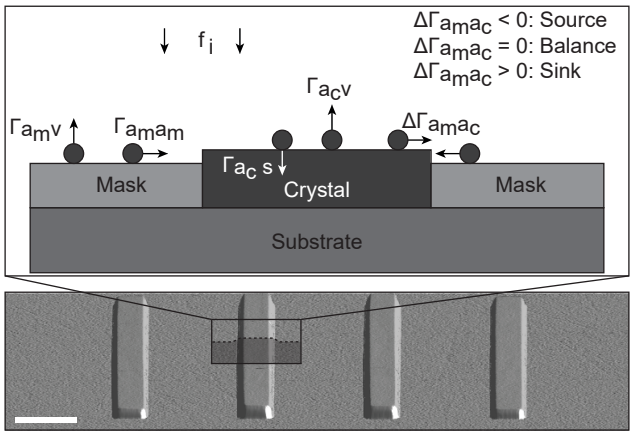

Figure 2.5: Top, A schematic representation of the adatom transitions to consider during selective area growth. Bottom, AFM micrograph of an array of 4 $[0\,1\,\bar{1}]$-oriented NWs on GaAs$(1\,0\,0)$, scale bar represents 500 nm. Figure adapted from Publication [1] [22].

Figure 2.5 depicts the different adatom transitions to be considered for SAG of III-V materials. The transitions state kinetics of the adatoms ($\Gamma_{\alpha\beta}$) from initial state α and final state β can be described by the Arrhenius equation [61]

$$\Gamma_{\alpha\beta} = \rho_\alpha \exp\left(-\frac{\delta g_{\alpha\beta}}{k_B T_{sub}}\right)$$

where k_B is the Boltzmann constant, ρ_α is the adatom density at the initial stage and $\delta g_{\alpha\beta}$ if the activation energy required for the transition to the final state. The different transitions involve adatom diffusion on the SiO_2 mask ($\Gamma_{a_m a_m}$), growing crystal surface ($\Gamma_{a_c a_c}$), at a mask-crystal boundary ($\Gamma_{a_m a_c}$), incorporation into the crystal solid phase ($\Gamma_{a_c a_s}$) or nucleation to solid phase on the mask ($\Gamma_{a_m a_s}$). Adatom desorption from the mask ($\Gamma_{a_m a_v}$) and crystal ($\Gamma_{a_c a_v}$) to vapor also occurs, where the

former is controlled by the substrate temperature (T_{sub}) and the latter is effectively ignored in this study. The exact geometrical and physical constraints of this model are presented in detail in Publication [1] [22]. The essential outcome of considering these transitions, i.e., the relevant term for controlling the growth rate is the flux across the mask-crystal boundary,

$$\Delta\Gamma_{a_m a_c,i} = \Gamma_{a_m a_c,i} - \Gamma_{a_c a_m,i}$$

If $\Delta\Gamma_{a_m a_c,i} < 0$, the SAG growth mode is referred to as *source*, since the flux of adatoms from the surrounding mask to the growing crystal is less than the flux of adatoms from the crystal to the mask. The SAG growth mode is referred to as *sink* if $\Delta\Gamma_{a_m a_c,i} > 0$. For the growth parameters considered in this study (see Section 6.4), Ga is observed to be in the sourcing mode, whereas In has been observed to operate in the sink mode as has already been observed [22]. Thus, this term is the effective selective area growth rate that differentiates the material incorporation in SAG NWs from to planar growths with no mask.

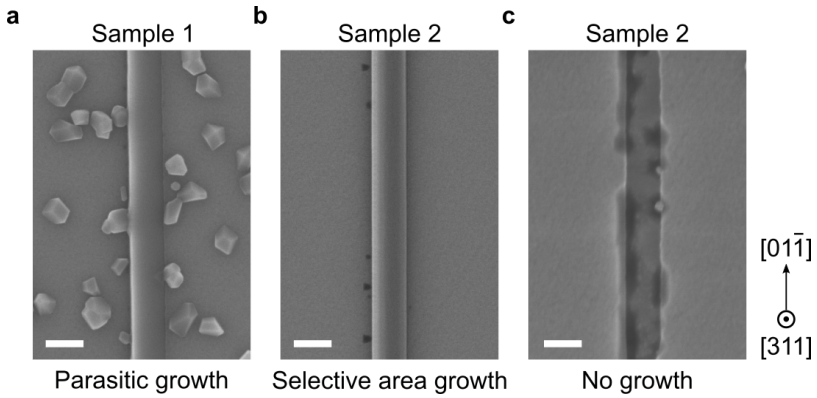

Figure 2.6: SEM micrographs of $[0\,1\,\bar{1}]$-oriented GaAs NWs from: **a** Sample 1 shows parasitic growth on the SiO_2 mask. **b** and **c** Sample 2 with NW growth and no growth, respectively.

Figure 2.6 shows $[0\,1\,\bar{1}]$-oriented GaAs NWs with identical mask opening widths. NWs in (a) and (b) are located approximately in the middle of an array consisting of 50 NWs. Sample 1 (a) shows NW growth along with parasitic growth on the SiO_2 mask, referred to as crystallites. This is only used for a representative purpose, the reason for the parasitic growth has not been confirmed and could be related to the growth parameters not chosen to be within the selectivity window. Sample 2 (b) shows NW growth occurring selectively only within the mask opening. Sample 2 (c) shows a region where only an isolated mask opening was designed, and no growth is observed. This is possible in the case where $\Delta\Gamma_{a_m a_c,i}$ is negative enough to override the growth within the exposed substrate. This shows that despite the

growth parameters chosen to be well within the selectivity window for Sample 2, the choice of mask dimensions also has a significant impact on the NW growth. The details of the dependence of mask dimensions such as NW width (W) and inter-wire distance, pitch (P) on material incorporation within the NWs has been studied for NWs grown on standard GaAs$(1\,0\,0)$ substrates [22].

2.6 Crystal shapes

Equilibrium crystal shapes describe the specific shapes that crystals adopt when they are grown under particular conditions, and they are influenced by the balance between surface energy (γ) and the energy associated with the crystal lattice structure. The surface energy is the energy required to create a new surface in a crystal and depends on the crystallographic orientation of the surface. The lattice energy, on the other hand, is the energy associated with the crystal lattice structure and is related to the inter-atomic interactions in the crystal. The equilibrium shape of a crystal is the shape that minimizes the total energy of the crystal system, which is the sum of the surface energy and the lattice energy. The equilibrium shape is the shape that minimizes the total energy of the crystal system. The Wulff construction is a geometric construction that enables one to determine the equilibrium shape of a crystal from crystallographic data and the surface energies of the crystal faces [41]. The crystal shape is composed of flat surfaces called crystallographic faces that correspond to the planes of the crystal lattice. Each face has a specific orientation and surface energy. The equilibrium shape of a crystal is the shape that includes all the crystallographic faces with the lowest surface energy, while the crystallographic faces that are not present in the equilibrium shape have a higher surface energy and are less stable.

Determining the equilibrium shape of a crystal can be achieved theoretically or experimentally. Theoretical methods utilize first principle calculations [62] that can have different outcomes for different models [63], and cannot account for the changes caused during actual growth, or hetero-epitaxial growth [64]. Thus, feedback from experimental methods is required and involves growing crystals under controlled conditions and observing and analyzing their shapes.

Under the constraint of SAG, the shape of nanostructures depends on the substrate symmetry [20] dimensions of the mask design parameters such as width, length and the proximity to another NW (pitch); and growth parameters such as substrate temperature, V/III ratio, use of surfactants, growth rates [22] as well as growth time, surface reconstruction [65] and surface diffusion of adatoms [66]. Under thermodynamic considerations, the shape of the crystal is decided by the stability of the facets it can possess [60, 67]. However, this approach neglects the very active adatom kinetics of the growth process.

This makes it important to be able to predict the shape and of the nanostructures in order to tailor experiments based on them.

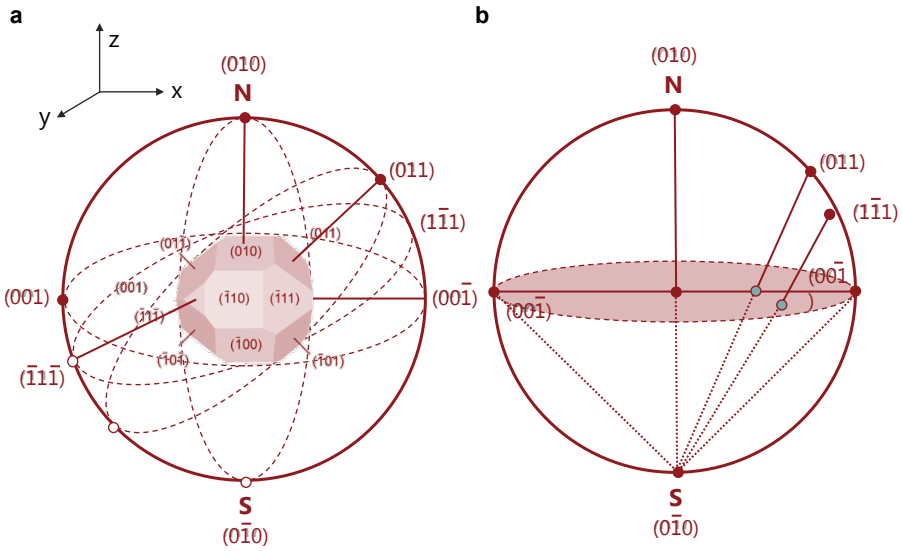

Figure 2.7: a A schematic representation of a cubic crystal that exhibits multiple facets. Normals from the facets are mapped onto a sphere, and as shown in **b**, subsequently mapped on the North or South pole (N or S), creating the stereographic projection (shaded circle).

A stereographic projection is a tool used in crystallography to visualize crystal orientations and their angular relationships projected onto a two-dimensional plane. Figure 2.7a shows a cubic crystal at the center of a sphere (the stereographic sphere) where the normals to each of the crystal faces are mapped onto the sphere in an array of points referred to as *poles*. Each point on the sphere therefore represents a crystal face or plane (and is labelled with the corresponding Miller index). This is depicted in a simplified way in Fig. 2.7b, with the shaded circle replacing the crystal, known as the the equatorial circle. Mapping any point from the sphere onto the north or south pole (N or S), intersects the equatorial circle, and this circle containing the angular relations of the different facets for a particular zone axis, is known as the stereographic projection. The choice of N or S will later correspond to A-polar or B-polar surfaces.

The dot product between the Miller indices of the NW direction and any possible facet showing translational symmetry along the NW axis must be zero, and this information is summarized in stereographic projections.

Here, the WinWulff software [68] is used to plot the SP of the $(1\,0\,0)$ and $(2\,1\,1)$ zone axes as shown in Fig. 2.8a and b, respectively. Each circle represents increments of 10°, with the outermost corresponding to 90° with respect to the substrate zone axis. The position of each pole on and around these circles depicts the angle at which that particular

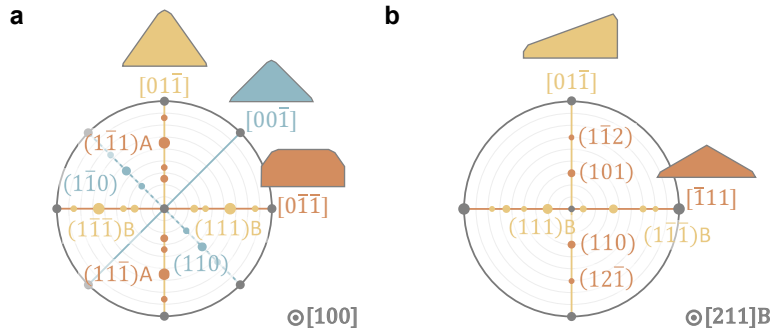

Figure 2.8: Stereographic projections along different zone axes depicting the angular relationship between crystal faces of a ZincBlende (ZB) crystal. The poles represent facets $(h\,k\,l)$, and the pole diameter is proportional to its d-spacing. The angle with respect to the substrate starts from 0° in the center and increases linearly to 90° at the perimeter, with each circle representing an increment of 10°. The directions along the outermost circle correspond to the high-symmetry in-plane NW orientations. The expected faceting of such NWs is indicated by the poles occurring along the normal to the NW direction, marked by the same color. Schematics of the cross-sectional shape of the NWs are shown alongside the high-symmetry directions for **a** $(1\,0\,0)$ substrate, **b** $(2\,1\,1)$B substrate.

plane exists with respect to the zone axis (substrate orientation) as well as in between the planes themselves. It should be noted that the spot diameter is set to be proportional to the d-spacing of an $(h\,k\,l)$ pole. This is a rough approximation, however low hkl-index reflections (i.e., large d-values) often have stronger intensities than higher hkl-index reflections (i.e., smaller d-values). Thus, the high-symmetry in-plane orientations along which nanostructures can be expected to grow homogeneously for the respective zone axes are depicted on the outermost circle.

For example, there are 2 high-symmetry orientations for the $(2\,1\,1)$ zone axis, namely the $[0\,1\,\bar{1}]$ and $[1\,\bar{1}\,\bar{1}]$ and NWs grown along these directions can possess all the facets that lie on the line orthogonal to it. The $[0\,1\,\bar{1}]$-oriented NW thus exhibits an asymmetric cross-section due to the angles associated with the $\{1\,1\,1\}$ type facets it can potentially manifest. The schematics of the NW cross-sections depicted in Fig. 2.8a [19, 21] and b are only representative for a set of mask design and growth parameters.

3

Experimental Methods

The success of the SAG process depends heavily on the precise and consistent fabrication of the mask layer, which must be done without causing any damage to the underlying substrate when creating windows to define the NW growth regions. Therefore, it is necessary to use various characterization techniques to evaluate the outcome and quality of the growth.

In this chapter, the experimental techniques that were employed for both the pre-growth fabrication of the substrates and the post-growth characterization of the resulting samples are presented. These techniques were carefully selected to ensure the accuracy and reliability of the data obtained, and to provide a comprehensive understanding of the growth process.

The pre-growth fabrication techniques included the deposition of the mask layer, electron beam lithography, and etching to create the necessary windows. The post-growth characterization techniques included scanning electron microscopy (SEM), transmission electron microscopy (TEM), electron energy loss spectroscopy (EELS), and atomic force microscopy (AFM).

Through the use of these techniques, valuable insights into the growth process and the resulting samples can be obtained. This information is critical feedback for the optimization of the SAG mechanism and the development of more efficient and effective NW growth.

3.1 Substrate fabrication

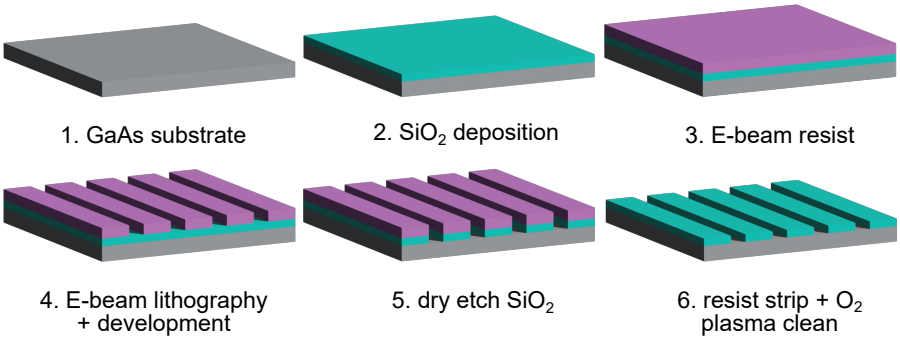

Figure 3.1: Schematic of substrate fabrication for SAG.

The steps involved in substrate fabrication for SAG are shown in Fig. 3.1.

- 1. An epi-ready semi-insulating 2 inch GaAs substrate which is 350 μm thick is used in this study.
- 2. 10 nm of SiO_2 is deposited onto the GaAs substrate using plasma enhanced chemical vapour deposition as a masking layer.
- 3. 300 nm of CSAR13 resist [69] is spin coated onto the substrate
- 4. Standard electron beam lithography (EBL) and subsequent development is performed to expose regions on the SiO_2 mask
- 5. The exposed regions are then etched using an inductively coupled plasma of a mixture of tetrafluoromethane (CF_4) and molecular hydrogen (H_2) thereby exposing the GaAs substrate.
- 6. The resist is removed using standard cleaning procedures and the substrate is thoroughly cleaned using O_2 plasma before transfer to the MBE chamber.

The SAG mask design used in this study consists of arrays of rectangles with varying length (L), width (W), inter-wire distance (P) and in-plane orientation (θ).

3.2 Molecular beam epitaxy

Molecular beam epitaxy (MBE) is a highly versatile crystal growth technique for epitaxial layers of various materials, including compound semiconductors such as InAs and GaAs. MBE was first developed in 1958 and has since undergone substantial improvements [70] in epitaxial growth with the aid of understanding growth kinetics, and in-situ growth monitoring using reflection high-energy electron diffraction

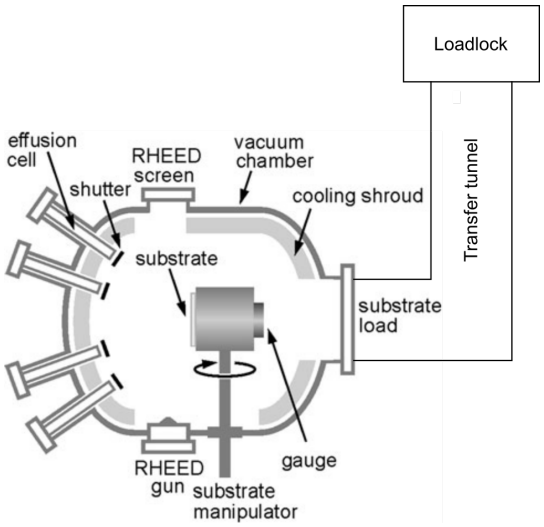

Figure 3.2: Schematic of a typical MBE chamber showing the most important components as labelled. Figure adapted from the book 'Epitaxy of Semiconductors' by Udo Pohl [41].

(RHEED). Growth in MBE takes place in an ultra-high vacuum (UHV) environment, with base pressures in the range of 10^{-11} mbar, enabling the use of high-purity materials through directional molecular beams of evaporated or sublimated sources without the need for a carrier gas.

The samples presented in this work were grown in a Varian GEN II system. Figure 3.2 depicts a schematic of an MBE system representative of the one used in this study, with the most important components labelled. During growth, the substrate is mounted on a temperature-controlled stage capable of rotation and faces the material sources. Here, we use solid source effusion cells for the elements of chemical groups III and V. The effusion cells are surrounded by heating coils which are used to heat the source and thus emit the material for growth, with shutters in front of the cells ensuring that material beams can be shut off within a tenth of a second, allowing for precise control of material deposition with mono-layer precision. The beam equivalent pressure and the substrate temperature (T_{sub}) are used to control the overall growth rate. T_{sub} can be reliably measured using a pyrometer, and the temperature of the effusion cells (which determines the beam flux) is calibrated by a beam flux gauge behind the stage. The substrate manipulator in this MBE system can be rotated such that the gauge sits in the exact location of where the substrate would be, thus ensuring very precise flux measurements.

To maintain the high level of purity inside the MBE system, a series of interconnected chambers are used, which allows for cleaning of the introduced sample by heating (in the loadlock) and removal of native oxide layers (transfer tunnel) from the surface of the III-V

semiconductor substrate before growth. Also, a liquid nitrogen (LN_2) cooling shroud is installed at the walls of the UHV chamber, which acts as a cold trap, improving the vacuum (background pressure) and adsorbing all the remaining atoms that are not absorbed by the sample. This generates temperature gradients of hundreds of degree celcius within the chamber to offer the cleanest possible growth conditions with atomic flux mean free paths of $\sim 1\,\mathrm{m}$ [71].

A RHEED setup within the MBE chamber allows for the in-situ monitoring of growth. It consists of an electron gun pointed at a grazing angle on the substrate. The RHEED pattern created by the diffracted electrons describes the surface or the first few MLs of the growing structures, providing information on the formation of planes of atomic roughness, as well as crystal information such as the lattice parameter, which can be used to determine the incorporation rate of different materials into compound structures [72]. RHEED is difficult to perform for SAG because majority of the substrate is covered with the amorphous SiO_2, however, in this case it is still very useful for calibration of growth rates.

3.3 Atomic force microscopy

Atomic force microscopy (AFM) is used as the primary tool for obtaining the topography of SAG substrates pre-MBE growth to determine the cleanliness of the sample, and post-MBE growth to study the SAG NWs in this work.

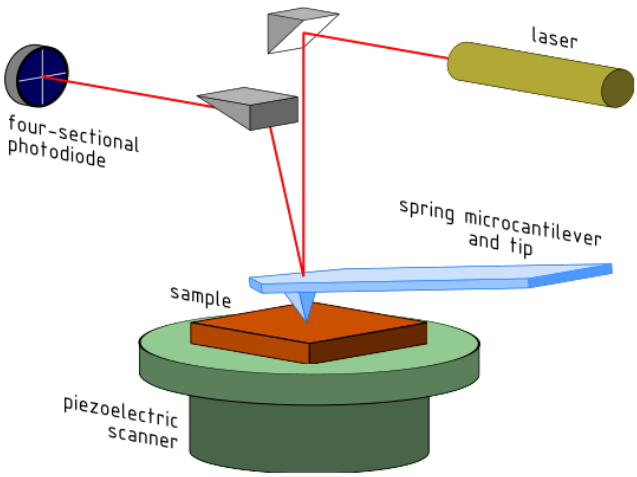

Figure 3.3: Schematic of a typical atomic force microscope (AFM) with optical detection of the deflection of a micro-cantilever. Figure adapted from Wikipedia [73].

AFM is a type of scanning probe microscopy that can image the surface of a material with sub-nanometer resolution in some cases.

The AFM probe, which is typically a small cantilever with a sharp tip, is brought into very close proximity to the surface being imaged, allowing the tip to interact with the material's surface forces. As the tip is scanned over the surface, the interaction forces between the tip and the surface are measured, and this information is used to create a high-resolution topographical image of the surface.The set-up for atomic force microscopy consists of a tip attached to a cantilever with a reflective backside, a laser, and a quadrant photo detector as seen in Fig. 3.3. A feedback loop (not depicted here) controls the motion of the cantilever through a piezo-element, depending on the mode of operation. The forces sensed by the scanning probe vary depending on the tip-sample distance and can be long- or short-range. The Lennard-Jones potential [74] is often used to model atomic forces and is a first-order approximation described by the function

$$U_{\mathrm{LJ}} = -4U_{\mathrm{o}}\left[\left(\frac{R_{\mathrm{a}}}{r}\right)^{12} - \left(\frac{R_{\mathrm{a}}}{r}\right)^{6}\right] \tag{3.1}$$

A graphical representation of the Lennard-Jones potential can be seen in Fig. 3.4. At $r = R_a$, the potential is zero and has a minimum value of U_{o} at the dashed line. U_{LJ} ranges from repulsive forces in the highlighted region on the left of the dashed line to attractive forces on the right as seen in Fig. 3.4, indicating the forces experienced by the probe. At large distances, the potential goes to zero as expected, reflecting the range limit of the forces. The regime of operation depends on the imaging mode, with contact mode operating in the repulsive regime and tapping mode in the attractive regime.

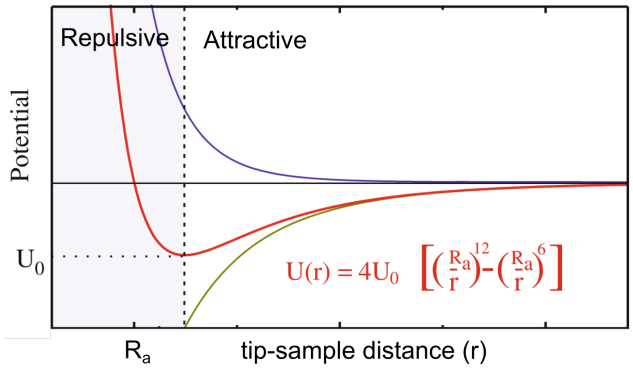

Figure 3.4: The Lennard-Jones potential U_{LJ}, which is zero at $r = R_a$ and has a minimum value of U_{o}. The highlighted region (left) represents repulsive forces and the region on the right represents attractive forces experienced by the probe. The potential goes to zero at large distances, indicating the range limit of atomic forces. Figure adapted from the textbook 'Scanning Probe Microscopy' by Bert Voigtländer [74].

A Bruker Dimension Icon AFM system operating in the ScanAsyst Air (SAA) has been utilized to measure all samples in this thesis. Bruker's AFM systems offer the SAA imaging mode, an intermediate contact mode that makes contact with the sample while oscillating the cantilever above the surface [75]. During imaging, force-distance curves are acquired at every measured point. SAA operation involves oscillating the cantilever at a low frequency of $(1 - 2\,\mathrm{kHz})$ relative to its resonance frequency, causing the tip to snap in and out of contact with the surface, resulting in force curves that are sensitive and optimally operated using a soft cantilever. Force-distance curves provide information about the quality of the sample by measuring adhesion as the tip snaps out of contact. In SAA, the AFM system automatically adjusts the imaging parameters such as the scan speed, the set-point (the distance between the tip and the surface), and the gain (the sensitivity of the feedback loop) based on the properties of the sample being imaged. As the probe scans over the surface, the system monitors the interaction forces between the tip and the surface, and adjusts the imaging parameters in real time to optimize the image quality. A detailed description of scanning artefacts, analysis of the force-curve [76] data has been presented in Anna Wulff Christensen's Master thesis [77].

Some key terms essential to operating the AFM tool are listed below:

- Cantilever: A small, flexible beam used as the AFM probe. The cantilever is typically made of Si or SiN, and is coated with a thin layer of metal to make it conductive.
- Tip: The sharp end of the cantilever, which interacts with the material being imaged. The tip is typically made of a hard material, SiN in this case.
- Piezoelectric scanner: A device that can move the AFM probe with very high precision. The scanner is typically made of a stack of piezoelectric crystals that can expand or contract in response to an applied voltage, allowing for precise movement of the probe in the all three directions.
- Feedback loop: A mechanism that keeps the distance between the tip and the surface constant during imaging. As the probe scans over the surface, the interaction forces between the tip and the surface change, and the feedback loop adjusts the position of the piezoelectric scanner to keep the distance between the tip and the surface constant.
- Force spectroscopy: A technique used to measure the interaction forces between the tip and the surface. The cantilever is typically oscillated at a fixed frequency, and the amplitude of the oscillation is measured as the tip interacts with the surface.

By analyzing the change in amplitude as a function of distance between the tip and the surface, the interaction forces can be measured.

- Scan rate: The scan rate is the speed at which the AFM probe scans over the surface being imaged. The scan rate is typically expressed in units of distance per unit time (nm/s). The scan rate can affect the quality of the image, with faster scan rates resulting in lower resolution images, but with a higher risk of damaging the sample.
- Resolution: The resolution of an AFM image is the smallest feature size that can be resolved by the imaging system. The resolution is determined by several factors, including the size of the tip, the interaction forces between the tip and the surface, and the noise in the measurement. The resolution is typically expressed in units of distance (e.g. nm), and can range from a few nm to sub-Å resolution, depending on the specific AFM system.
- Samples/line: The number of samples per line is the number of data points collected along a single scan line. This parameter affects the level of detail in the image, with higher numbers of samples per line resulting in more detailed images, but also requiring longer scan times and generating larger datasets.

In general, optimizing these parameters involves a trade-off between imaging speed and image quality. Higher scan rates can produce faster images but may result in lower resolution, while higher resolutions and numbers of samples per line will produce more detailed images but may require longer scanning times. The AFM operating parameters using Bruker's SAA mode of operation have been presented in the Appendix C.

3.4 Electron microscopy

Electron microscopy is a technique used to study the structure and composition of materials at the atomic scale. This technique uses a beam of electrons instead of light to image the sample, providing a much higher resolution than traditional light microscopy. The electron beam has a much shorter wavelength (in the order of picometers) than light, which allows for imaging of much smaller features. Simply put, the electron energy, sample thickness, type of detector are some of the key factors that differ in the different electron microscopy techniques.

Figure 3.5 shows a schematic of a scanning electron microscope. SEM is a type of electron microscopy that involves scanning a focused electron beam over the sample's surface. The electrons in the beam interact with the atoms in the sample, and this interaction produces

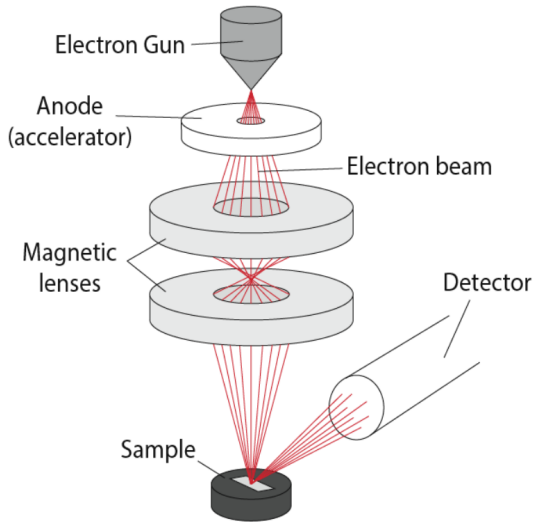

Figure 3.5: A simplified schematic of a scanning electron microscope, indicating the important components involved in operation. Figure adapted from [78].

signals that are detected and used to form an image. The following modes of electron microscopy were not conducted by me. The details of the mode of operation can be found in standard textbooks [79, 80]. Hence only a brief description of the kind of information that can obtained from different techniques that were used in this thesis to analyse the crystal structure of the SAG NWs has be been presented in the following:

Transmission Electron Microscopy (TEM) involves transmitting a beam of electrons through a thin sample (a lamella of the sample is prepared using focused ion beam [81]) to produce an image of the sample's internal structure. TEM can provide high-resolution imaging of the internal structure of materials, including their crystal structure and defects [82]. TEM is particularly useful for studying the atomic structure of materials, as it can provide information on crystal defects and other nanoscale features.

High-Angle Annular Dark-Field Scanning Transmission Electron Microscopy (HAADF-STEM) is a specialized type of STEM that uses a high-angle annular dark-field detector to image the sample. HAADF-STEM is particularly useful for studying the atomic structure and composition of materials, as it can provide information about the atomic number of individual atoms and their arrangement in the sample. In HAADF-STEM, the detector detects scattered electrons at high angles, which produces a bright image of heavy elements and a dark image of light elements.

Geometric phase analysis (GPA), dilatation and rotation maps are advanced techniques used in electron microscopy to study the crystallographic orientation and deformation of materials at the atomic scale.

These methods involve the analysis of diffraction patterns produced by the interaction of electrons with the crystal structure of the material, and they are particularly useful for understanding the mechanical and structural properties of materials. Using GPA, stacking faults can be identified by the presence of extra spots or streaks in the diffraction pattern that do not correspond to any known crystallographic planes. These extra spots or streaks are caused by the scattering of electrons at the stacking faults, and their presence indicates the presence of a stacking fault in the crystal. There are other types of crystal deformities that can be identified using these techniques. For example, dislocations, which are lattice defects that result from the deformation of the material, can be visualized in GPA analysis as bright lines in the diffraction pattern.

Dilatation and rotation maps are advanced imaging techniques that can provide information about the local strain and deformation of a material. These techniques involve the comparison of atomic positions between different images to calculate the displacement of atoms and the resulting deformation. Dilatation maps can reveal areas of the material that are under stress or have undergone plastic deformation, while rotation maps can reveal the presence of grain boundaries and the distribution of rotations in the crystal structure. Dilatation and rotation maps can also reveal the presence of stacking faults. In a dilatation map, a stacking fault will appear as a region of high strain where there is a change in the stacking sequence. In a rotation map, a stacking fault will appear as a region where there is a change in the crystallographic orientation.

Details about the lamella preparation and TEM operating parameters are presented in Appendix D.

Part II

Homo-epitaxy of **GaAs**

The selective area growth of homo-epitaxial pure GaAs and surfactant-mediated GaAs(Sb) nanowires is presented in this part. The significance of considering fabrication related tolerances for nanowire design is discussed. The nanowire length is found to be have an effect on the morphology of the nominally aligned nanowires. The results of nanowires grown on novel high-index substrates discussed. It is found that the substrate out-of-plane and in-plane orientation, polarity, and the use of Sb as a surfactant during GaAs growth can be leveraged to engineer the nanowire shape. Moreover, the effect of varying the SAG mask dimensions allows for the tracking of the GaAs growth stages.

4

Effect of in-plane alignment

The results presented in this chapter overlap with publication [2] [31]:

Effect of in-plane alignment on homoepitaxial nanowires
G Nagda, D V Beznasyuk, J Nygård, T S Jespersen
Nanotechnology (2023)

4.1 Introduction

SAG is lithographically defined, making it technically possible to define a template with a very large degree of flexibility and along any in-plane direction. It is therefore important to understand the influence of substrate symmetry for the resulting crystal growth. The scalability of SAG comes with the price of NWs being epitaxially connected to the substrate along the entire length. This makes the crystals highly sensitive to interface and surface quality and this remains an ongoing challenge to be overcome compared to out-of-plane NW growth. Further, as discussed below, the tolerances of materials and processes lead to some degree of uncertainty in aligning SAG patterns to the symmetry of the substrate and the consequences need to be addressed.

This chapter presents a systematic study of the effect of mis-orientation on MBE grown homoepitaxial GaAs and surfactant mediated GaAs(Sb) SAG NWs on GaAs(2 1 1)B. Under optimized growth conditions, the structure of SAG NWs is found to be dependent on the substrate symmetry and limited by the mis-orientation between the NW axis and the high symmetry directions of the substrate. This mis-orientation is unavoidable due to the tolerance of substrate manufacturing and fabrication methods. Although such tolerance and mis-orientation is small, its effect is amplified in growth of long SAG NWs due to the epitaxial registry between NW and substrate. As will be seen in the following sections, increasing mis-orientation leads to increasing formation of discrete crystal steps on the NW facets. The effect NW length and the use of Sb as a surfactant are studied in order to determine their influence on the NW morphology, to circumvent the effect of misalignment.

4.2 Experiment

Using a previously established range of parameters ensuring growth on the exposed GaAs substrate without parasitic growth on the SiO_2 mask [55], GaAs and GaAs(Sb) NWs are grown at a substrate temperature of $T_{sub} = 600°\,C$ and a Ga growth rate of 0.1 ML/s for 30 min corresponding to $\approx 50\,nm$ of planar GaAs growth on a GaAs(1 0 0) substrate. An As/Ga ratio of 9 and Sb/Ga ratio of 3 is used for GaAs and GaAs(Sb) growths, respectively, ensuring growth rates determined by the Ga flux. Figure 4.1 shows a top-view atomic force micrograph of a section of a circular array of GaAs(Sb) NWs grown on GaAs(2 1 1)B. Since there is no parasitic growth observed on the SiO_2 surrounding the NWs, it is concluded that the influence of the substrate orientation on the selectivity window is not significant and implies that the growth conditions used for this sample lie well within the already established selectivity window for GaAs growth on GaAs(1 0 0) [55].

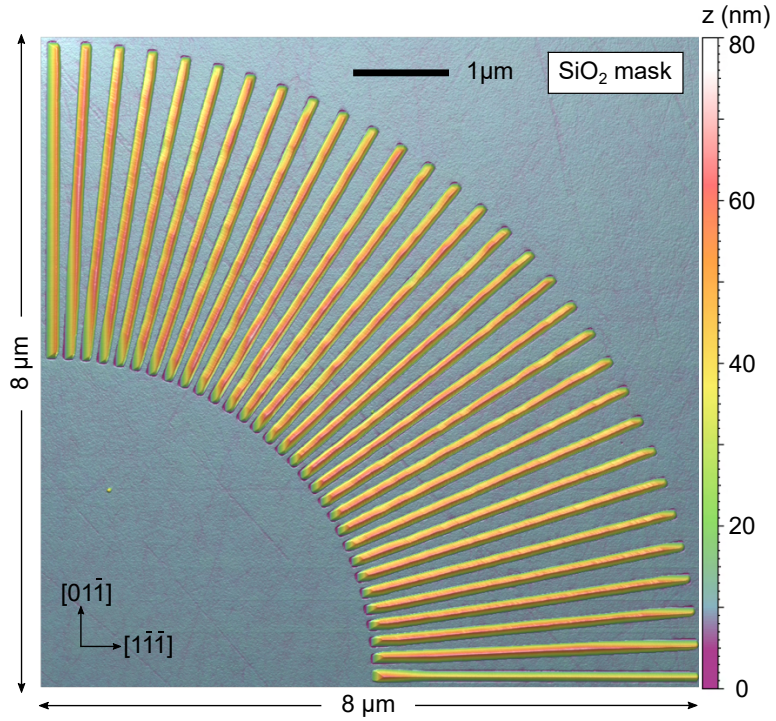

Figure 4.1: Top-view atomic force micrograph of GaAs(Sb) NWs grown on GaAs(2 1 1)B. No parasitic growth is observed on the SiO_2 mask.

For this study, a GaAs(2 1 1)B substrate with a diameter of 2 inches was processed with identical patterns repeated on four quarters. The pattern consists of NW openings with different lengths and angles. Following the fabrication, the wafer was cleaved into quarters and two samples were grown; one with GaAs and one with GaAs(Sb). The samples thus have the same fabrication-related tolerances, and the resulting $[1\,\bar{1}\,\bar{1}]$-oriented NWs were systematically characterized using scanning electron microscopy (SEM) and atomic force microscopy (AFM). Individual steps on the NW facets were identified by performing AFM along the NW. Details of the AFM operating parameters are included in Appendix C.

The $[1\,\bar{1}\,\bar{1}]$ oriented NWs on GaAs(2 1 1)B which exhibit a symmetric cross-section bound by $\{1\,1\,0\}$ facets are investigated to study the influence of mis-orientation and quantify the structural morphology of the NW in terms of facet roughness (S_q). Information about material incorporation in SAG NWs is obtained by studying the volume dependence of the NWs on the in-plane orientation. Changing cross-sectional shapes of the NWs oriented between high-symmetry in-plane orientations provides information about the facet evolution. The effect of NW length on the morphology shows that for a given mis-orientation, there is a length scale for which the discontinuities in the NW facets are minimized. It is found that as previously reported for standard $(1\,0\,0)$ substrates [19], Sb also has a surfactant effect during GaAs growth on the $(2\,1\,1)$B orientation. A smoother NW surface

can be achieved for largely misaligned NWs, however, it is found to have a negligible effect at small misalignment. Such information may be used for directing design of e.g. electrical devices sensitive to crystal imperfections.

4.3 Origin of misalignment

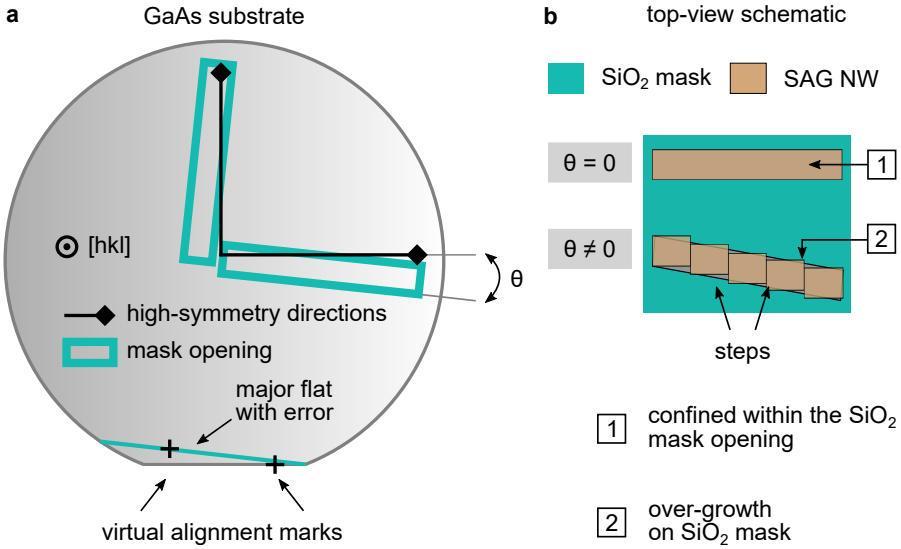

Figure 4.2: a Top-view schematic of a substrate indicating typical errors in out-of-plane orientation (color gradient) and the orientation of the major flat (green line) along with the co-ordinate system used for lithographic processes. **b** Top-view schematic of SAG NWs that are aligned (no steps) and misaligned (with steps) with respect to a high-symmetry in-plane orientation.

A typical GaAs substrate received from the manufacturer comes with a margin of error with respect to the specified out-of-plane (substrate surface) and in-plane (major flat) orientations. This is illustrated in the top-view schematic in Fig. 4.4b where the the color gradient depicts a hypothetical error in the out-of-plane orientation relative to the specifications (ϕ) from left to right and the green line illustrates the supplied major flat which is mis-oriented by an angle θ with respect to the actual crystal direction. An out-of-plane mis-orientation ($\phi \neq 0$) leads to step edges on the surface. While this is beneficial for planar growth since it promotes the layer-like growth [83], it might also lead to height variations in NWs grown in-plane.

Figure 4.3 shows the height maxima (z_{max}) of $[1\,\bar{1}\,\bar{1}]$-oriented GaAs and GaAs(Sb) NWs along a length of 4μm, from AFM data. The NW height at approximately the top facet, along the entire length shows that excluding the end facets, the GaAs(Sb) NW maintains the same height along a length of 4μm as opposed to the pure GaAs NW. A possible explanation for this is that for the GaAs case, there might

be more nucleation sites and hence simultaneous crystal growth at multiple sites might lead to inhomogeneity in the amount of material incorporated. Thus, out-of-plane mis-orientation is not considered for the remainder of the analysis.

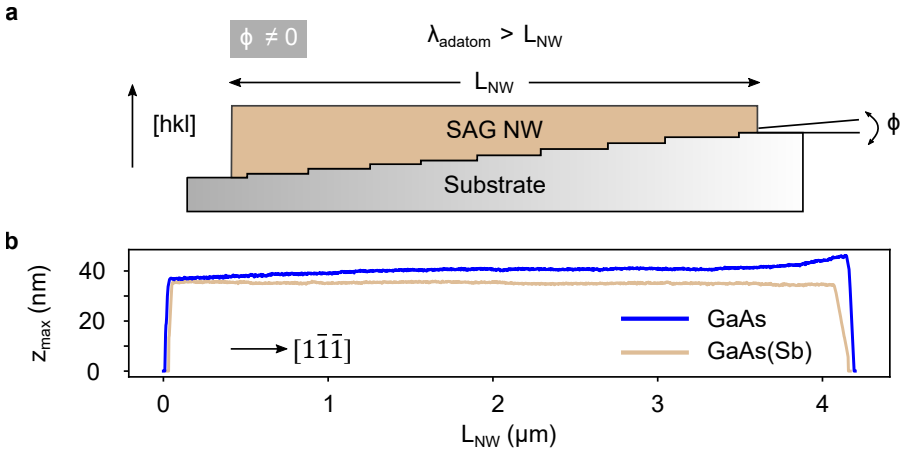

Figure 4.3: NW height (z_{max}) profile extracted at the maxima from AFM data, along a length of 4μm for both GaAs and GaAs(Sb) NWs.

For SAG NWs used in this study, the trench openings in the SiO_2 mask impose a constraint on the growth dynamics that are nanoscale in one dimension (trench width) and several microns long in the other (trench length). The NW facets that develop during growth are dependent on the orientation of the trench openings along the length. In-plane misalignment of the trench openings for NW growth is caused by external misalignment due to manufacturing errors during wafer flat grinding and internal misalignment due to the tolerance of lithographic procedures. The external misalignment for the substrates used in this study as provided by the manufacturer is maximally $\pm 0.1°$. Assuming that errors in stage movement during electron beam lithography due to thermal drift and precision of the tool itself are negligible, the major contribution to internal misalignment still comes from the error in determining the edge of the major flat which is used to align the mask design with virtual alignment marks with respect to the major flat (see Fig. 4.4b). This is because the flat grinding and polishing processes will not result in atomically flat edges and surfaces [84] leading to ambiguity in placement of the alignment marks. The maximal error in determining the major flat edge as a result of rounded edges of the substrate is estimated to be $\pm 0.4°$. Typically, the substrates from the same manufacturing batch will have the same external error and the varying internal error in between different lithographic runs and the total misalignment will be the combined result of both, i.e., $\pm 0.5°$. The resulting trench openings will thus be misaligned with respect to the high symmetry in-plane directions.

Due to the epitaxial connection between the substrate and the SAG NW, misalignment of the NW results in sections of the NW over-

growing on the SiO_2 mask, in order to maintain the NW facets with low surface energy. Since the crystal does not grow epitaxially on the SiO_2 mask, the overgrowth occurs in segments, as illustrated in the top-view schematic in Fig. 4.4c of a perfectly aligned NW and one that has a misalignment with respect to the high-symmetry in-plane direction. The distance at which it becomes energetically unfavourable for the crystal to grow on the mask, the NW facet forms a step towards the trench axis and this repeats along the NW length.

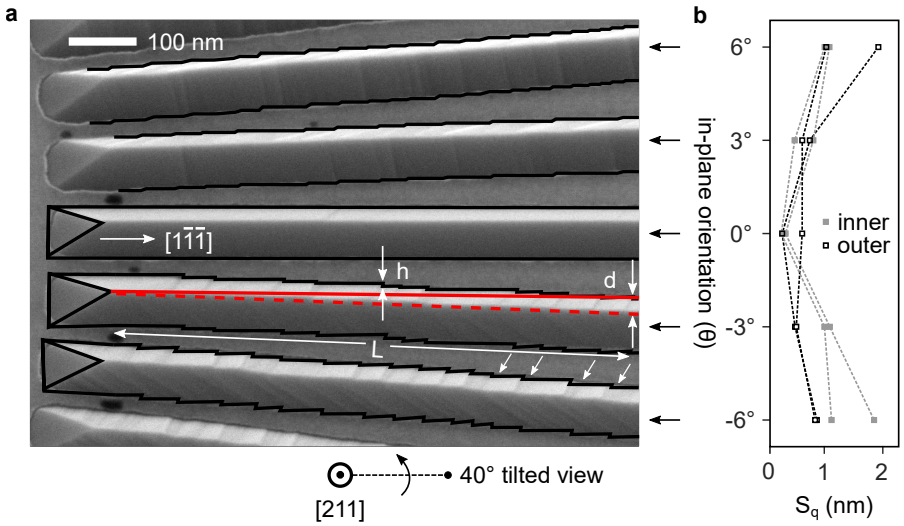

Figure 4.4: a a 40°-tilted SEM image of a series of GaAs(Sb) NWs oriented along the $[1\bar{1}\bar{1}]$ direction and in increments of 3° on GaAs(2 1 1)B. The overlaid schematic highlights the geometric parameters relevant for calculating the angle of mis-orientation. **b** Facet roughness S_q for the inner (outer) NW facets facing toward (away from) the $[1\bar{1}\bar{1}]$-oriented NW as a function of in-plane orientation.

Figure 4.4a shows a 40°-tilted SEM image of GaAs(Sb) NWs on GaAs(2 1 1)B. The middle NW is nominally aligned along the $[1\bar{1}\bar{1}]$ direction and bound by {1 1 0}-type facets. The surrounding NWs are oriented along $\theta = \pm 3°, \pm 6°$. The NWs aligned at 3° and 6° show growth in segments separated by steps on the inclined facets (indicated by arrows, and emphasized by the black outline) and these segments become shorter with increasing mis-orientation. In the following, a NW segment of length L (excluding the end facets) is considered, where the step-height along the facet is denoted as h and number of steps as n (Fig. 4.4a). The angle of mis-orientation θ for a NW can be deduced using geometry: $\theta = tan^{-1}(\frac{d}{L})$ where the total step displacement, $d = h' \times n$, where h' is the projection of h onto the substrate plane. The parameters n and h were determined through careful analysis of high-resolution AFM topographic maps.

Image processing tools within Python are used for AFM data analysis. A typical AFM image of approximately $[1\bar{1}\bar{1}]$-oriented NWs on a GaAs(2 1 1)B substrate is shown in Fig. 4.5a. Such an image is used

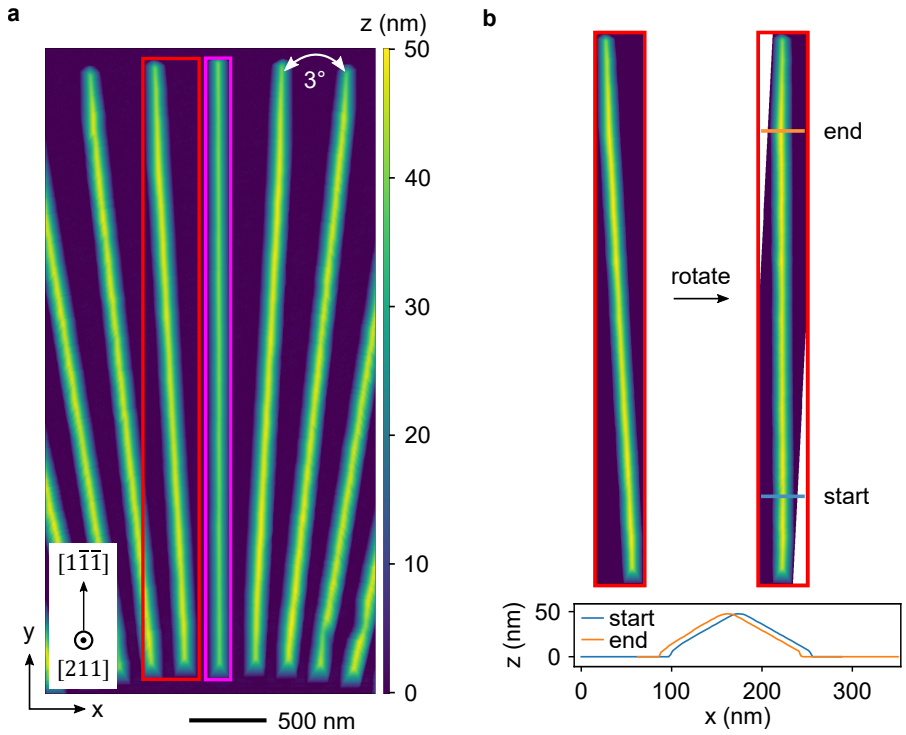

Figure 4.5: NW detection from AFM data and step-height analysis **a** A typical AFM image of approximately $[1\bar{1}\bar{1}]$-oriented NWs on a GaAs(2 1 1)B substrate. Using Python image analysis, the NWs are detected as individual objects for further analysis. **b** An intentionally 6° misoriented NW (left), the same NW rotated to align the y axis (right), cross-sectional profiles (bottom) at the two ends of the NW depict the overgrowth of the NW on the SiO_2 mask as a result of the in-plane misorientation.

to obtain information about the NW topography such as step height h and number of steps n. Most of the image processing tools were obtained from scikit-image processing [85]. As an example, the NW highlighted in the red box in Fig. 4.5a is considered. Using a rotation function, it is aligned to the vertical axis as shown in Fig. 4.5b. Overgrowth on either side of the mask opening can be seen by comparing profiles across the width at the two ends of the NW in Fig. 4.5b (bottom).

Next, the $[1\bar{1}\bar{1}]$-oriented NW (depicted in the magenta box in Fig. 4.6a) is considered to estimate the degree of misalignment. This requires accurately measuring the number of steps formed on the NW facets. A series of 10 line profiles taken along one of the facets of the NW (black arrow) are offset to the mean value and plotted in Fig. 4.6b panel **(i)**.

The step height extracted from such a profile is inaccurate due to: an overall slope along the length of the NW due the height variation along the length, an additional slope induced by the tilted line profile [86]. Correcting the profile for the overall slope by subtracting the

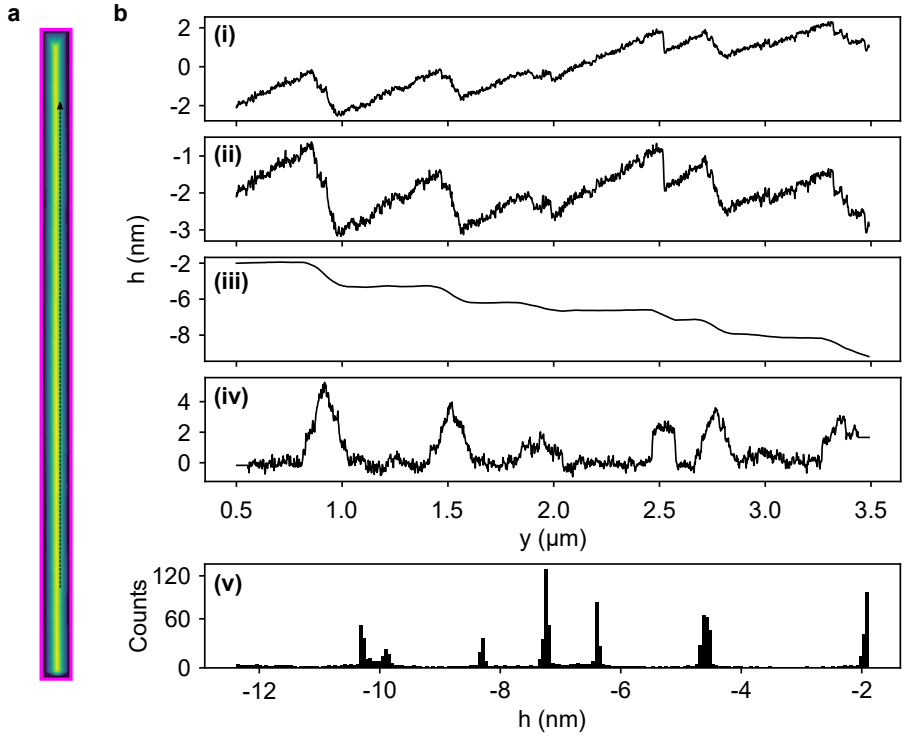

Figure 4.6: a Nominally aligned NW under consideration to estimate the degree on misalignment. **b**(i) A typical averaged profile along one facet of the NW, (ii) overall slope subtracted from the mean profile, (iii) profile rotated such that the facets are aligned horizontally, (iv) differentiated profile from (iii), (v) corresponding histogram of profile in (iii).

line-fit from the data shown in panel **(i)**, results in the profile showed in panel **(ii)** of Fig. 4.6b. Further, smoothing the data over 101 points using the Savitzky Golay filter [87] and using a rotate function until the terraces are horizontal, results in a profile shown in panel **(iii)** of Fig. 4.6b. The sharpness of its corresponding histogram shown in panel **(iv)** is used as a way to attain accurate rotation of the profile, as well as the total displacement d. Differentiating the profile data from panel **(iii)** and results in panel **(iv)** on which a peak finding function is used to gives n. This method is implemented on all the AFM data presented in this study.

Using this, $\theta = 0.26° \pm 0.04°$ is obtained as a misalignment of the nominally $[1\,\bar{1}\,\bar{1}]$-oriented NW from the real $[1\,\bar{1}\,\bar{1}]$ direction of the substrate. Here the error is due to the accuracy of $\Delta d = 2\,\text{nm}$ in measuring the total step displacement. The value for θ is thus consistent with the tolerances of experimentally determining the in-plane orientation of the substrate.

The step density on the NWs facets is also quantified as the root mean square (RMS) facet roughness (S_q), which is extracted using AFM. Figure 4.4b depicts S_q for the inner (outer) NW facets facing toward (away from) the $[1\,\bar{1}\,\bar{1}]$-oriented NW as a function of in-plane ori-

entation. Increasing number of steps with increasing mis-orientation results in a larger S_q and is minimized for the nominally $[1\,\bar{1}\,\bar{1}]$-oriented NW. Two ways to minimize S_q are proposed: finding the length scale for which NWs can grow step-free despite an in-plane misalignment and secondly, the use of Sb as a surfactant during GaAs growth to suppress step formation. In the following section, the effect of in-plane orientation on material incorporation and facet evolution of GaAs(Sb) NWs grown on GaAs$(2\,1\,1)$B is investigated.

4.4 Material incorporation and facet evolution

Electrical characteristics of SAG NWs have been known to depend on the structural characteristics such as NW and facet orientations [20]. The faceting of NWs depends on the substrate symmetry and growth conditions and in turn also affects the growth dynamics. Thus, the effect of in-plane orientation on the material incorporation in NWs is investigated next.

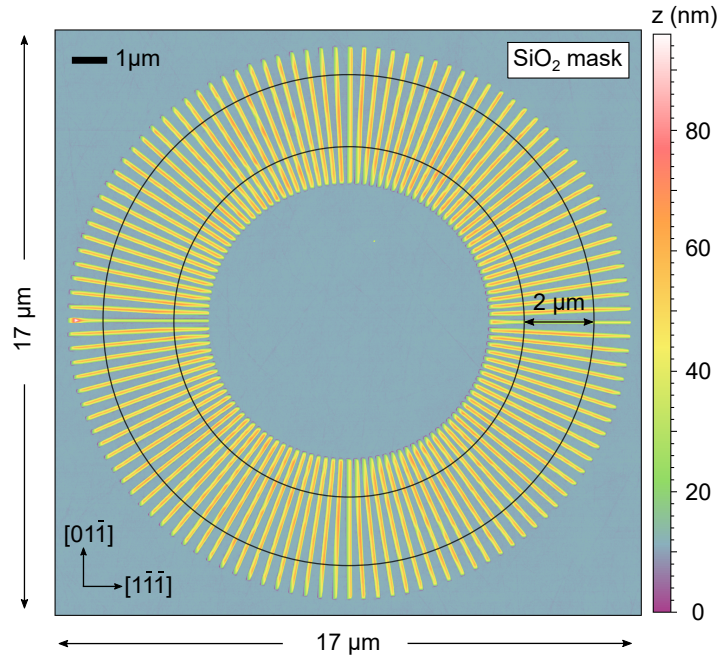

Figure 4.7: a A $17 \times 17\,\mu m^2$ AFM topography of 120 GaAs(Sb) NWs that are positioned in a circular array. The SiO_2 mask is levelled to be at zero, and the NW volume is extracted from a 2μ m long segment of the NWs (the region in between the two circles).

We obtain a $17 \times 17\,\mu m^2$ AFM scan that includes the entire circular array of 120 GaAs(Sb) NWs (see Fig. 4.7a). To eliminate the possibility of scanning artefacts, the array is imaged twice, parallel to the $[1\,\bar{1}\,\bar{1}]$ and the $[0\,1\,\bar{1}]$ direction. The image is then levelled such that the SiO_2 mask resides at zero. The volume is extracted from a $2\,\mu$m long segment from approximately the middle of the NWs (the region

in between the two circles). This is to minimize contributions from varying incorporation at the NW ends, the end facets and the effects of varying inter-wire distance along the length of the NWs, on the volume. The 120 NWs that are positioned in a circular array such that NWs along $\theta = 0°$, 90°, 180° and 270° correspond to $[1\bar{1}\bar{1}]$, $[01\bar{1}]$, $[\bar{1}11]$ and $[0\bar{1}1]$ respectively. Figure 4.8a shows a polar plot of the NW volume normalized to the smallest volume, V_0 (corresponding to the $[1\bar{1}\bar{1}]$–oriented NW) as a function of angle. All 120 NWs are included in a single $17 \times 17\,\mu m^2$ scan. To check for artifacts due to the AFM scan direction, the measurement was performed parallel to $[1\bar{1}\bar{1}]$ and $[01\bar{1}]$ directions.

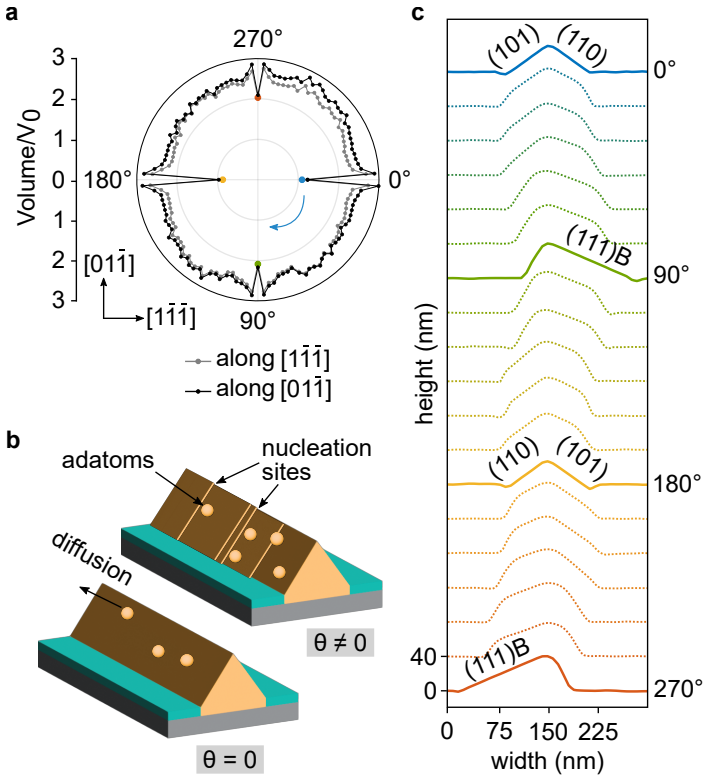

Figure 4.8: Material incorporation in NWs oriented along different in-plane directions. **a** Polar plot depicting the individual NW volume of 120 GaAs(Sb) NWs grown on GaAs(2 1 1)B normalized to the volume of a $[1\bar{1}\bar{1}]$-oriented nanowire, as a function of in-plane orientation. **b** Schematic of a NW aligned (smooth facets) and misaligned (facets with steps) with respect to a high-symmetry in-plane direction. **c** Waterfall plot of cross-sectional profiles of NWs that are oriented 15° apart. The dominant facets are as labelled and the profiles are color coded to their respective normalized volumes in **a** and are extracted along the direction of the blue arrow in **a**.

As seen in Fig. 4.8a, the NW volumes extracted from both scan directions follow a similar trend. The volume is significantly smaller for NWs oriented along the high-symmetry orientations. With increasing

mis-orientation, the NWs exhibit increasing step density (as seen in Fig. 4.4a). Since nucleation at step edges minimises the surface free energy by incorporation of additional adatoms within the growing crystal [88], these NWs incorporate more material as each step acts as a nucleation site for incoming adatoms (see schematic in Fig. 4.8b). The activation energy for diffusion and desorption is higher at a nucleation site, thus increasing the probability that adatoms will instead accumulate and nucleate. This is consistent with the dramatic increase in volume of misaligned NWs as seen in Fig. 4.8a. Furthermore, the neighboring NWs experience an increased flux due to the expelled adatoms from the aligned NWs. This further increases the volume of the NWs next to the aligned NWs and may explain the small decay for further mis-oriented NWs.

Figure 4.8a also shows that the $[1\,\bar{1}\,\bar{1}]$–oriented NWs incorporate less material compared to the $[0\,1\,\bar{1}]$-oriented NWs. This can be attributed to a longer Ga adatom diffusion length along the $\langle 1\,1\,1\rangle$ directions [89] which causes a fraction of the incoming adatoms to diffuse along the NW length and be expelled onto the SiO_2 mask in the early stages of NW growth where the $\{1\,1\,0\}$ facets have not developed yet. As the NW grows with increasing time and starts developing facets, the resulting material incorporation is a combined result of the adatom diffusion length along the $\langle 1\,1\,1\rangle$ directions (NW axis) as well as the $\{1\,1\,0\}$ planes (NW facets as seen in Fig. 4.8c).

To visualize the facet transformation of the NWs dependent on the in-plane orientation, an AFM topographical profile across the approximate center of the length of the NWs spaced 15° apart, starting from the $[1\,\bar{1}\,\bar{1}]$–oriented NW is extracted (Fig. 4.8a). The blue arrow in Fig. 4.8c corresponds to the direction along which the profiles were extracted. NWs oriented along high-symmetry directions exhibit well defined facets dictated by Wulff construction [90] thereby minimising the surface free energy of the crystal. The mis-oriented NWs exhibit a mixture of different facets along with increased material incorporation. Note that the $(1\,1\,1)$B facet tends to develop for NWs already at $\approx 15°$ deviations from the $[1\,\bar{1}\,\bar{1}]$-oriented NWs despite having a higher surface free energy as compared to the $(0\,1\,1)$ facet for pure GaAs [91]. This can be attributed to the surfactant effect of Sb during GaAs growth [92]. The development of different facets along with differing adatom diffusion length and density of nucleation sites further complicates the interpretation of material incorporation within the mis-oriented NWs.

4.5 Effect of nanowire length

For a given substrate after a fabrication run for SAG, since the error in defining the NW trenches is fixed, the resulting step density on the NW facets must also be constant. However, the free surface at the

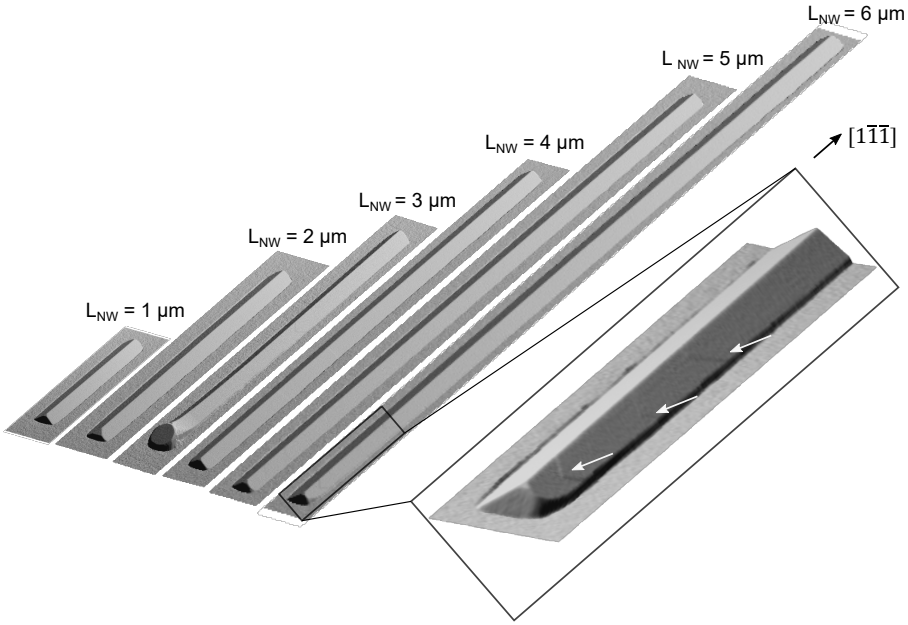

Figure 4.9: 3D AFM topography of $[1\,\bar{1}\,\bar{1}]$-oriented GaAs(Sb) NWs on GaAs(2 1 1)B with length $L_{NW} = 1 - 6\,\mu$m. A NW with $L = 6\,\mu$m exhibits steps on the facets highlighted by the white arrows in the close-up.

ends of the trench may allow for a larger degree of overgrowth on the SiO_2 mask, thus allowing for a larger tolerance towards misalignment. Thus, to find the length scale for which it is possible to obtain a NW with smooth facets without steps, nominally $[1\,\bar{1}\,\bar{1}]$-oriented GaAs(Sb) NWs with $L_{NW} = 1 - 6\,\mu$m and $W_{NW} = 150\,$nm were grown. AFM topography of the NWs is presented in Fig. 4.9. End facets of the NWs are excluded from the segment that is used to calculate n. An example of steps (highlighted with white arrows) visible on one of the facets is presented for the case of $L_{NW} = 6\,\mu$m in the inset.

AFM was performed on a total of 16 NWs and the corresponding n on both facets are tabulated in Fig. 4.10b. As expected, the number of steps on the NWs is linearly dependent on the NW length and the resulting dependence of n along both NW facets is presented in Fig. 4.10a. However, performing a linear fit on the n dependence averaged for both facets, it can be seen that it does not extrapolate to zero at $L = 0\,\mu$m but instead at a finite length L^*. Thus for NWs shorter than L^*, NWs exhibit no steps. To eliminate the possibility of a statistical anomaly, AFM was performed on multiple NWs for $L_{NW} = 1\,\mu$m, where 10 out of 11 NWs show no steps at all. Performing a linear fit on the n dependence including all 16 NWs, $L^* = 0.96 \pm 0.18\,\mu$m is obtained. The slope of the fit gives us a step density in the middle of an arbitrarily long NW to be $1.41 \pm 0.07\,\mu\text{m}^{-1}$. The value of L^* depends on the misorientation – $\theta = 0.26° \pm 0.04°$ in the present case – and is thus specific to the sample and fabrication run.

a

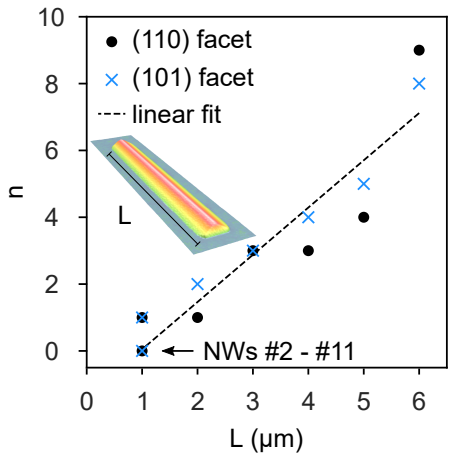

b

NW #	L (μm)	$n_{(110)}$	$n_{(101)}$
1	1	1	1
2	1	0	0
3	1	0	0
⋮	⋮	⋮	⋮
11	1	0	0
12	2	1	2
13	3	3	3
14	4	3	4
15	5	4	5
16	6	9	8

Figure 4.10: a Number of steps (n) as a function of NW length (L). A linear fit is performed and extrapolated to obtain a length L^* for which NWs with no steps can be obtained. **b** A list of NWs with different L and the corresponding n on either facets. 10 out of 11 1μm long NWs exhibit no steps.

Figure 4.11a shows a top-view AFM image of a series of GaAs(Sb) NWs oriented along the $[1\,\bar{1}\,\bar{1}]$ direction and in increments of 3° on GaAs(2 1 1)B. The region highlighted in the black box shows the NWs facets at the ends have fewer to no steps compared to the middle. For NWs oriented at $\theta = \pm 3°, \pm 6°$ from the $[1\,\bar{1}\,\bar{1}]$ direction, the maximum NW height (z_{max}) at all points along the NW length is used as an indicator of the in-plane orientation of the NW. The position of z_{max} of the misaligned NWs with respect to that of the $[1\,\bar{1}\,\bar{1}]$-oriented NW, $\Delta x(z_{max})$, along the NW length is presented in Fig. 4.11b. This shows a tendency for the ends of misaligned NWs to overgrow more on the SiO_2 mask with few to no steps and gradually align towards the $[1\,\bar{1}\,\bar{1}]$ direction. This confirms that free surface at the ends of the trenches allows for a larger degree of over-growth on the SiO_2 mask and thus allows for a larger tolerance towards misalignment.

It should be emphasized that the quantitative results obtained here can be extended towards homoepitaxial growth of NWs on both conventional and novel substrate orientations. Each substrate fabricated for SAG can be characterized post-growth to estimate the collective internal and external error in defining the NW trenches and the resulting length scale for which step-free NWs can be obtained. For experiments wherein longer SAG NWs are necessary by design, AFM characterization can be performed prior to device fabrication in order to place electrical contacts in segments of the NWs that exhibit no steps along the facets. Thus, even though it is not possible to completely eliminate the morphological imperfection in the NWs, careful design of the experiment can lead to minimized contribution from high S_q.

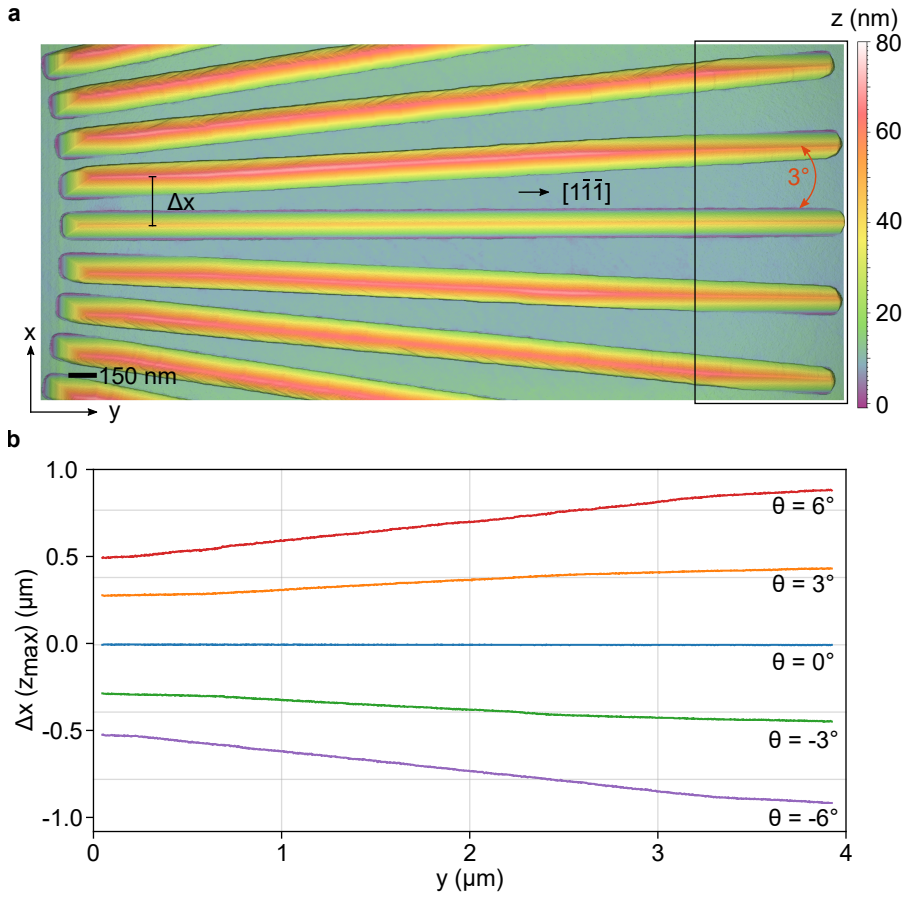

Figure 4.11: **a** Top-view AFM topography of a series of GaAs(Sb) NWs oriented along the $[1\bar{1}\bar{1}]$ direction and in increments of 3° on GaAs(2 1 1)B. The outer ends of the NWs highlighted in the black box show misaligned NWs at $\theta = \pm 3°, \pm 6°$ to over-grow more on the SiO_2 mask to gradually align towards the $[1\bar{1}\bar{1}]$ direction. **b** The distance between positions of the maximum height for all NWs $\Delta x(z_{\max})$ along the NW length.

4.6 Effect of Sb as a surfactant

Finally, the use of Sb as a surfactant is considered for reducing S_q. GaAs NWs were grown on GaAs(2 1 1)B with and without Sb and also with varying degrees of intentional misalignment with respect to the $[1\bar{1}\bar{1}]$ direction. The resulting 3D AFM topography for both GaAs and GaAs(Sb) NWs are shown in Fig. 4.12a and b, respectively. Again, the number of steps on NW facets clearly increases with mis-orientation (arrows in Fig. 4.12a and b), and the effect is more pronounced for GaAs NWs compared to the GaAs(Sb) NWs. The corresponding dependence of S_q is shown in Fig. 4.12c for inner (outer) facet facing toward (away from) the $[1\bar{1}\bar{1}]$-oriented NW. These facets exhibit different step edges due to different in-plane polarity on the substrate (details presented in section 4.7). Sb reduces S_q for $\theta \neq 0$ and thus helps reducing the effect of mis-orientation. The lowest value of

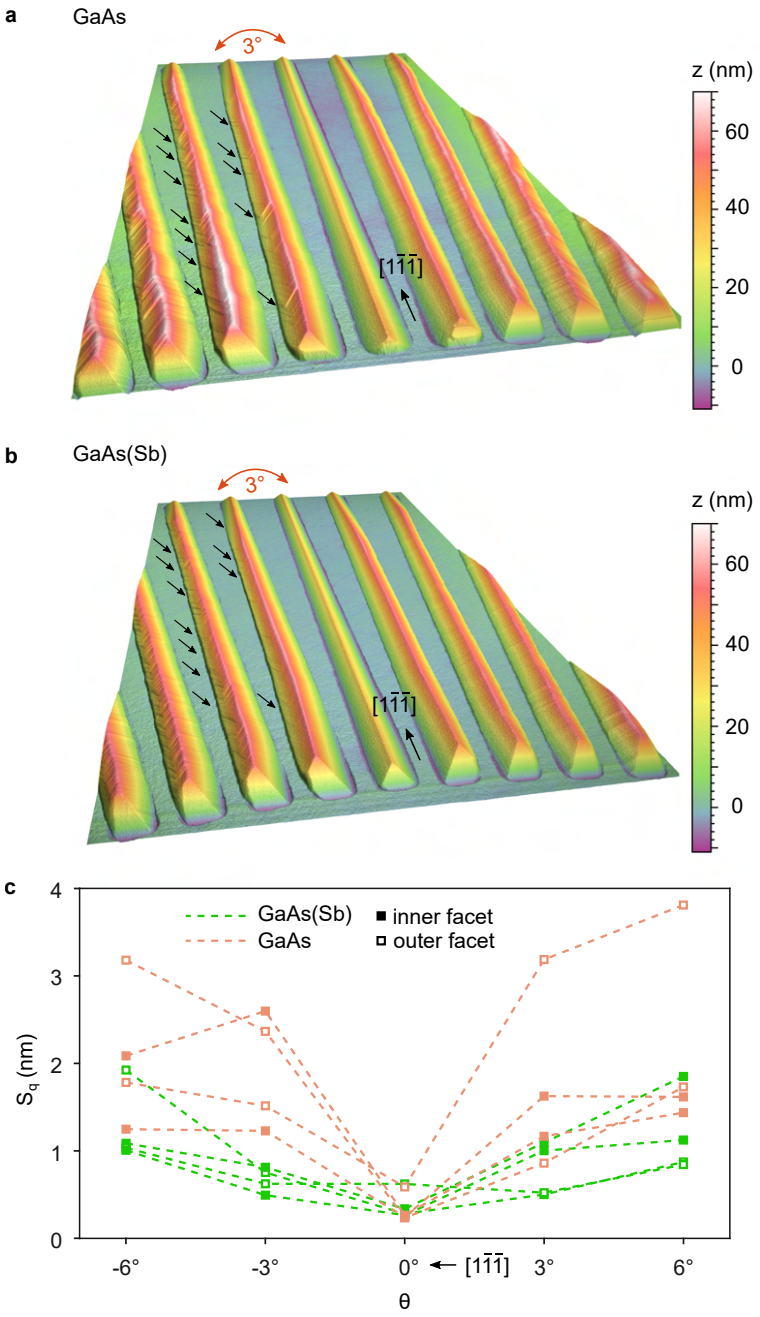

Figure 4.12: Series of **a** GaAs and **b** GaAs(Sb) NWs on GaAs(2 1 1)B oriented along the $[1\,\bar{1}\,\bar{1}]$ direction as well as NWs oriented in increments of 3° with respect to it. **c** Dependence of S_q on in-plane orientation for GaAs and GaAs(Sb) NWs. S_q is also presented for the inner (outer) facet of the misaligned NWs facing toward (away from) the $[1\,\bar{1}\,\bar{1}]$-oriented NW.

$S_q \approx 0.4\,\text{nm}$ is observed for both nominally $[1\,\bar{1}\,\bar{1}]$-oriented GaAs and GaAs(Sb) NWs and is comparable to that of a substrate prior to any fabrication processing. Thus, based on the two samples investigated for the case of $[1\,\bar{1}\,\bar{1}]$-oriented GaAs NWs on GaAs(2 1 1)B, it can be concluded that Sb does not improve the crystal quality as opposed to

GaAs(Sb) SAG NWs grown under similar conditions on conventional GaAs(1 0 0) substrates [19, 21, 22].

Surfactants are known to modify surface free energies and adatom diffusion lengths for compound semiconductors and have been employed to suppress 3D island growth [92, 93]. Despite the possible surfactant effect of locally changing the facets surface free energy during crystal growth, there is no impact on the overall cross-sectional shape of the nominally $[1\,\bar{1}\,\bar{1}]$-oriented NWs shown in Fig. 4.12. The use of Sb as a surfactant for in-plane homoepitaxial GaAs growth on GaAs(1 0 0) substrates has been reported to demonstrate a reduction in S_q [19]. A similar effect in suppression of S_q is observed in this study for largely misaligned $[1\,\bar{1}\,\bar{1}]$-oriented NWs grown on a GaAs(2 1 1)B substrate and confirms the feasibility of the method for achieving smoother facets. However, as demonstrated in the previous section, it does not guarantee NWs devoid of steps above $L_{NW} \approx 1\,\mu$m. This study demonstrates that using the NW length is a promising way to ensure minimal contribution to morphological disorder instead.

4.7 Step edges on side facets

Approximately $[1\,\bar{1}\,\bar{1}]$-oriented NWs on GaAs(2 1 1)B substrates exhibit steps on the side facets. This is shown in Fig. 4.13a and b with a top-view SEM image of the same NWs with contrast and color adjusted for visibility. The image shows that the step edges are oriented along different directions on both facets. While the reason for this is not completely clear, given the in-plane polarity of the substrate from the manufacturer, it is deduced that the inner facets exhibit B-polar $\langle 1\,1\,1\rangle$ type step edges whereas the outer facets exhibit A-polar $\langle 1\,1\,1\rangle$ type step edges. The effect of Sb on formation of the different step edges on both facets is unknown. Figure 4.13c shows an AFM topography of both facets of the NW which are levelled with respect to the $\{1\,1\,0\}$ zone axes. The levelled image is used to calculate the orientation of the step edges and it is confirmed that they are indeed the $\langle 1\,1\,1\rangle$ type step edges. There is no obvious correlation between the number of $\langle 1\,1\,1\rangle$A and $\langle 1\,1\,1\rangle$B step edges apart from an expected increase in both their numbers with increasing misalignment. It is difficult to quantify the number of step edges due to the increasing variation in step height and steps growing on existing steps.

4.8 Conclusions

In conclusion, a systematic study of the effects of small and large scale misalignment of GaAs and GaAs(Sb) SAG NWs with respect to the in-plane orientations on GaAs(2 1 1)B has been presented. It is found that a 3° misaligned NW leads to $\approx$ 300% increase in the volume

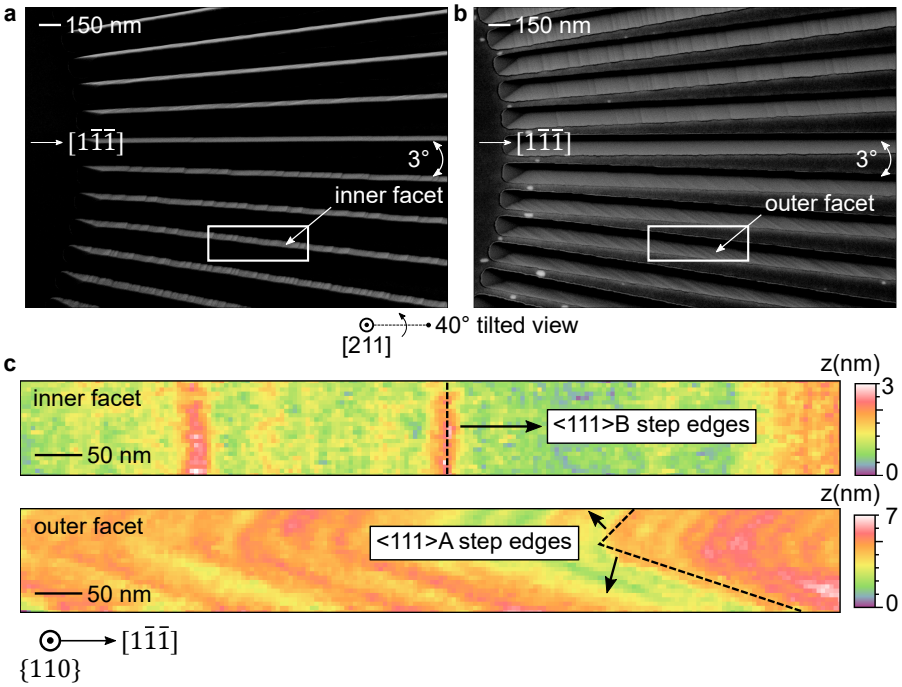

Figure 4.13: Steps edges on approximately $[1\bar{1}\bar{1}]$–oriented NWs. **a** and **b** show top-view SEM image of the same NWs where the contrast has been adjusted to enhance visibility of the step edges on inner (outer) facet facing towards (away from) the $[1\bar{1}\bar{1}]$-oriented NW. Furthermore, the colors are inverted in **b**. **c** is an AFM of the highlighted region in **a** and **b**, levelled towards the $(1\,1\,0)$ and $(1\,0\,1)$ facet respectively. The inner facet exhibits $\langle 1\,1\,1\rangle$B step edges whereas the outer facet exhibits $\langle 1\,1\,1\rangle$A step edges.

due to growth dynamics governed by adatom diffusion lengths and orientation dependent facet formation. The in-plane mis-orientation in defining trench openings within the substrate which leads to an undesired increase in facet roughness (S_q) of the NWs is important to be minimized in order to reduce structural disorder. Previously demonstrated use of Sb as a surfactant for NWs grown on standard $(1\,0\,0)$ substrates also minimizes S_q for large scale misalignment, however it is not enough to obtain step-free $[1\bar{1}\bar{1}]$-oriented NWs on GaAs$(2\,1\,1)$B. Small scale misalignment is important to be considered for device design, in particular in light of the inherent errors associated with the tolerance of substrate manufacturing and fabrication. A length scale for which NWs can tolerate an unintentional misalignment of $\theta = \pm 0.5°$ and suppress step formation is estimated to be $L \sim 1\,\mu$m. This confirms that AFM characterization of SAG NWs from a particular substrate prior to device fabrication can enable control over the crystal quality of the conducting channel by design. By virtue of the scalability of SAG, it can also be possible to make copies of the mask design for a range of in-plane orientations with $\theta = \pm 0.01°, \pm 0.02°$.. such that one of the NWs is bound to be perfectly aligned. Thus, for

experiments with strict requirements on the magnitude of disorder in the semiconducting NWs, taking into account effects of misalignment on the NW morphology, careful design of the SAG mask and structural characterization of NWs prior to device fabrication should enable control of the NW crystal quality.

5

Shape Engineering

The results presented in this chapter overlap with with manuscript [5]:

Shape engineering of in-plane semiconductor nanowires
G Nagda, D V Beznasyuk, J Nygård, T S Jespersen
In preparation

The high-angle annular dark field scanning transmission electron microscopy (HAADF-STEM) results presented in this chapter were acquired by **Dr. Sara Martí- Sánchez** and **Christian Koch** under the supervision of **Prof. Dr. Jordi Arbiol** affiliated with the Catalan Institute of Nanoscience and Nanotechnology (ICN2), CSIC and BIST, Campus UAB, Bellaterra, Barcelona, Catalonia, Spain.

5.1 Introduction

It has been demonstrated that the electrical characteristics of MBE grown InAs SAG NWs on GaAs substrates are vastly improved by introducing GaAs(Sb) buffer layers prior to InAs growth [19]. The flat top-facets of the resulting NWs are showed to allow significant elastic strain, resulting in a better field effect response due to fewer defects in the InAs channel. However, this has only been demonstrated for NWs with a particular geometry and not much is known about the dependence of the quality of the transport-active layers on the geometry of the underlying GaAs buffer layers.

In this chapter, we try to bridge this gap by demonstrating the possibility of engineering NWs with different cross-sectional shapes on non-standard (high-index) GaAs substrates. This is achieved by varying substrate out-of-plane and in-plane orientations and by use of Sb as a surfactant during GaAs growth. Growth conditions such as substrate temperature, growth rate, growth time and V/III ratio are kept identical for all growths, which allows for a systematic study of the effect of the substrate and corresponding in-plane orientation dependence. Details of the growth parameters are presented in Appendix B. The growths are performed for a variety of mask dimensions such as width (W) and inter-wire distance (pitch P), which allows for an understanding of the material incorporation and facet evolution dependent on the varied parameters. Varying mask dimensions potentially work as proxy for a temporal study, since growth for NWs with different mask dimensions will be terminated at different stages, and still be contained on the same growth substrate. This is due the dimension dependent material incorporation in the NWs [22]. The NW morphology for all growths is obtained by performing AFM. For select dimensions of the GaAs(Sb) growths on $(3\,1\,1)$A and B substrates, cross-sectional HAADF-STEM micrographs are also obtained. NWs are grown in a circular array and corresponding AFM data is used to extract NW volume and compared across all the samples.

5.2 Nanowire faceting on standard substrates

Figure 5.1a-d shows the stereographic projections of commonly reported substrate orientations. The construction of the projections and how to read them has been discussed in Section 2.6. The schematics of the NW cross-sections oriented along the high-symmetry in-plane orientations are based on the shapes that have already been reported for: InAs/GaAs(Sb) growth on GaAs$(1\,0\,0)$ [19, 21] by MBE, for InAs growth on InP$(1\,1\,0)$ and $(1\,1\,1)$B [20] by chemical beam epitaxy (CBE). As per the schematics, only the corresponding poles have been labelled for all projections, for better visibility. Although the cross-sectional shapes are only representative of the growth conditions, some observa-

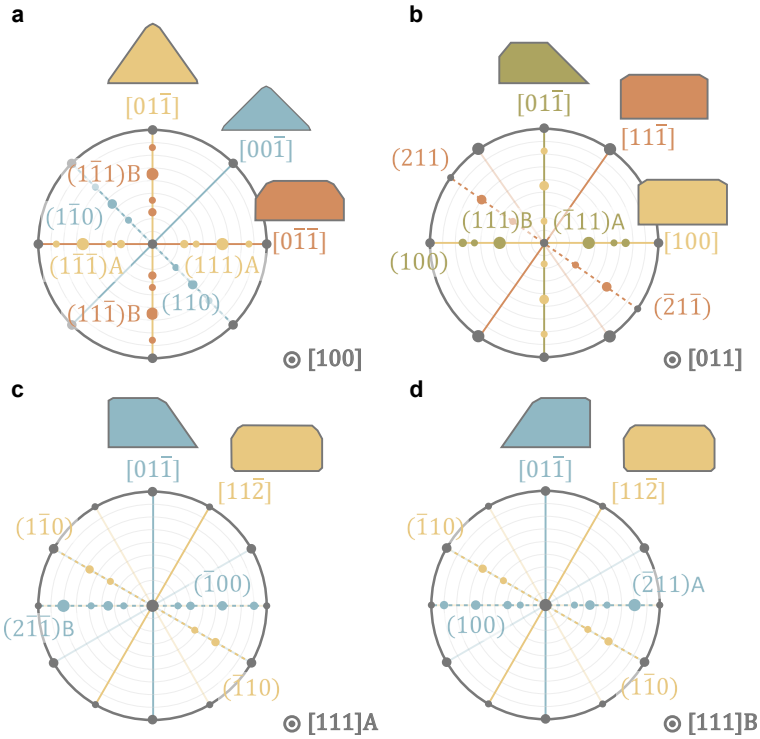

Figure 5.1: a-d Stereographic projections of standard (low-index) substrates. High-symmetry in-plane orientations are labelled at the outermost circle with a schematic of the corresponding NW cross-section, color-coded with the possible facets available. The cross-sectional shape is only representative of a particular set of growth conditions.

tions can be made. Due to the (4-fold) symmetry associated the $(1\,0\,0)$ zone axis, all NWs exhibit mirror-symmetric cross-sections. Even if certain other facets become more energetically favorable under different growth conditions, the NWs will exhibit the mirror-symmetric shapes with those facets. The same applies for NWs on $(0\,1\,1)$, $(1\,1\,1)$A and B substrates, except for the ones oriented along the $[0\,1\,\bar{1}]$ (or equivalently $[0\,\bar{1}\,1]$) direction. Due to the symmetry associated with this direction, these NWs are bound by facets that occur at non-equivalent angles, resulting in a asymmetric cross-sectional shape.

It should be noted that for $[0\,1\,\bar{1}]$ oriented NWs on $(1\,1\,1)$B substrates, a different cross-sectional shape has been observed by MBE growth [55], due to the manifestation of a $(1\,1\,\bar{1})$B facet instead of the vertical $(\bar{2}\,1\,1)$ facet. This is interesting because, the occurrence of $\{1\,1\,1\}$B facets is more likely due the lower surface energy associated with it [62] than $\{2\,1\,1\}$ type facets [35]. This demonstrates the dependence of the possible faceting on the differing surface energies associated with the different growth conditions in both experiments. Moreover, a different shape has been observed for $[0\,1\,\bar{1}]$ oriented InSb NWs on InP$(1\,1\,1)$B substrates [94], which highlights the difference

in associated surface energies for differing compounds. Although no published research exists for SAG NWs on (1 1 1)A, considering that change of polarity only corresponds to a mirrored stereographic projection, the expected schematics of the NW shapes have also been mirrored from their counterparts.

5.3 Nanowire faceting on high-index substrates

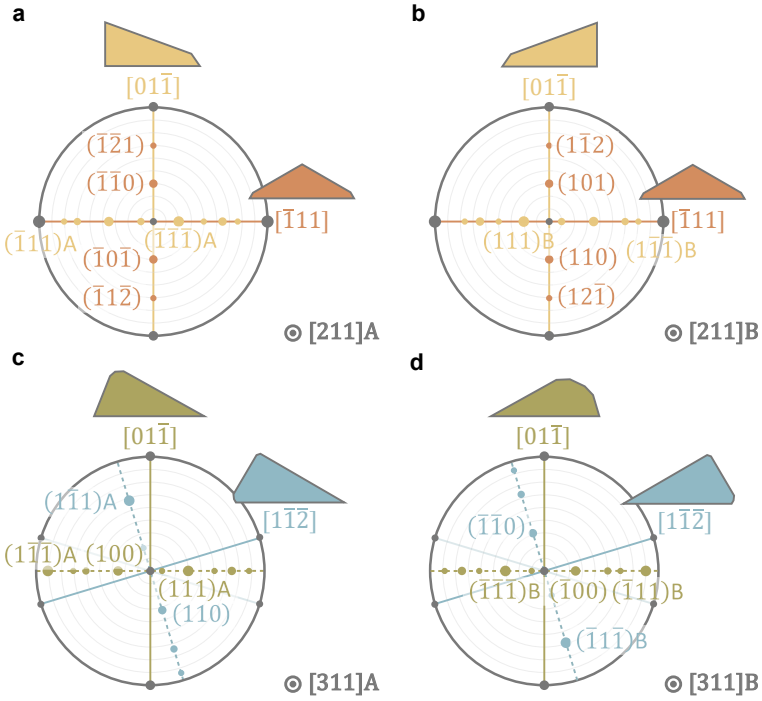

Figure 5.2: a-d Stereographic projections of high-index substrates. High-symmetry in-plane orientations are labelled at the outermost circle with a schematic of the corresponding NW cross-section, color-coded with the possible facets available. The cross-sectional shape is only representative of a particular set of growth conditions.

High-index substrates such as (2 1 1) and (3 1 1) both have a polarity associated with them. The corresponding crystal structure of these surface has been presented in the Section 5.2. Figure 5.2a-d shows the stereographic projections associated with these surfaces, with the A- and B-polar maps simply mirrored.. The corresponding schematics of the NWs along the high-symmetry in-plane orientations are color-coded with the facets they are likely to manifest. The ⟨1 1 1⟩ -oriented NWs on (2 1 1)B substrates have already been observed in Chapter 4, and are found to exhibit a mirror-symmetric cross-section bound by {1 1 0} type facets. The [0 1 $\bar{1}$]-oriented NWs on all high-index substrates have facets available at angles such that they will likely exhibit a highly asymmetric cross-section. The same would be expected

for the $\langle 1\,1\,2\rangle$-type NWs on $(3\,1\,1)$ substrates. The polarity associated with high-index substrates is an additional variable to the possible NW faceting since it is known that A- and B-polar surfaces exhibit different surface energies due the the different surface reconstruction mechanisms associated with them [36, 38, 62].

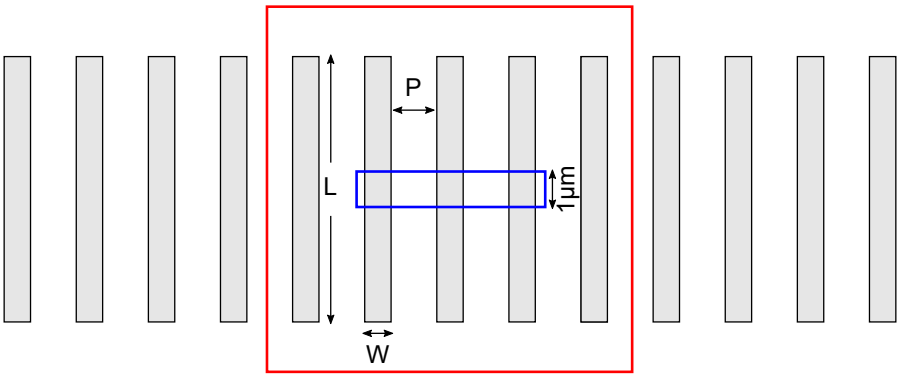

Figure 5.3: Schematic of an array of NWs, with NW length L, width W, inter-wire distance P. The red box corresponds to approximately the center of an array and the blue box corresponds to a $1\,\mu$m region at the middle of the NWs, where AFM was performed for all studies.

In the following, GaAs and GaAs(Sb) NWs grown in an array of 50 from all the high-index substrates were characterized using AFM. The SAG mask dimensions were varied such that NW arrays were grown with four different mask opening widths ($W1 - W4$) and four different pitch ($P1 - P4$) for each width, whereas the NW length ($L = 10\,\mu$m) was kept constant for all NWs. The four widths were varied from $40 - 100\,$nm in steps of $20\,$nm and the pitch was varied from $1 - 4\,\mu$m in steps of $1\,\mu$m. The actual width and pitch might vary from these values and was not accurately determined for all the samples with a systematic pre-growth characterization. Figure 5.3 shows a schematic of such arrays where the red box indicates that the NWs from approximately the middle of the array were selected, and the blue box indicates the $1\,\mu$m region from approximately the middle of the NWs that was chosen to perform AFM.

Figure 5.4a and b shows the AFM profiles of $[1\,\bar{1}\,\bar{1}]$ and $[0\,1\,\bar{1}]$-oriented GaAs and GaAs(Sb) NWs grown in $(2\,1\,1)$A and B for all different SAG mask dimensions. The AFM data was averaged over a length of $L = 10\,\mu$m and the solid lines correspond the average profile with and the colored band corresponds to the corresponding standard deviation. Each column corresponds to a different growth as labelled on top, with the pitch increasing from top to bottom as $P1 - P4$. Each of the four profiles within each box correspond to the different widths $W1 - W4$.

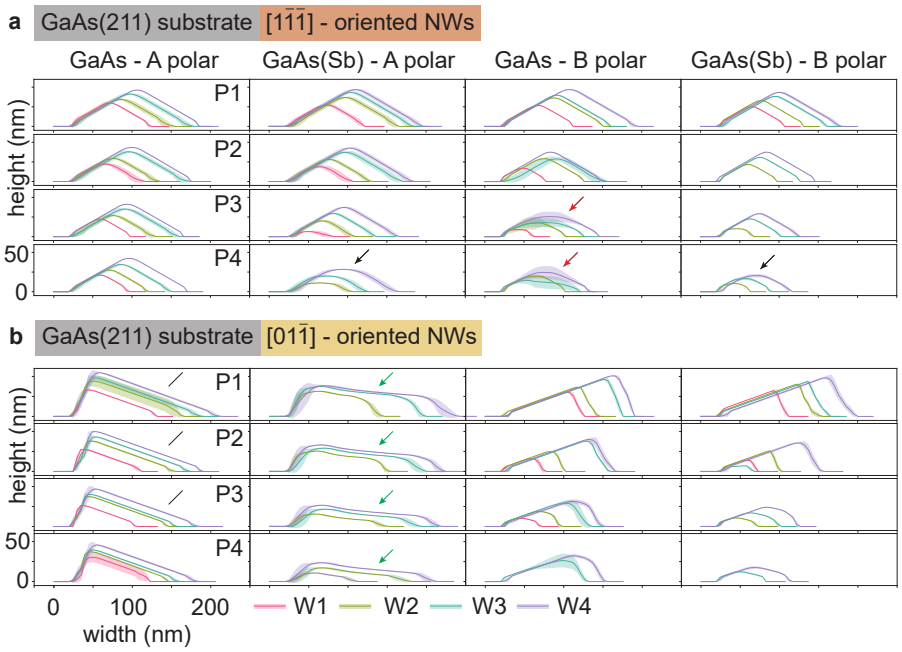

Figure 5.4: AFM topography of **a** $[1\bar{1}\bar{1}]$ and **b** $[01\bar{1}]$-oriented GaAs and GaAs(Sb) NWs on (211)A and B substrates. The columns correspond to different growths, with NWs from arrays with increasing pitch $P1 - P4$, and the 4 AFM profiles in each box corresponds to width $W1 - W4$.

First, we look at the $[1\bar{1}\bar{1}]$-oriented NWs for all growths Figure 5.4a. Despite the varying mask dimensions, substrate polarity and use of Sb as a surfactant, almost all NWs show a mirror-symmetric cross-section bound by the $\{110\}$ type facets that have been observed already for NWs considered in Chapter 4. For all samples, it can be seen that the NWs grown with a constant width at a larger pitch incorporate less material than at a smaller pitch. Similarly, NWs grown at a constant pitch with a larger width incorporate more material than with a smaller width. This becomes more evident when we look at the GaAs(Sb) NWs on (211)A (and B) substrates. The NWs at pitch $P4$ are caught at an earlier stage of growth due to less material, and when compared to their GaAs counterparts, they seem to incorporate even lesser material made evident by the not fully developed $\{110\}$ facets (see black arrows). It should be noted that the at pitch $P4$, the NWs width the smallest width $W1$ do not even grow. For GaAs NWs grown on the B-polar substrate, an unusually higher uncertainty in the NW topography is observed (see red arrows). The reason for this is not clear, however it is possible that the flat top-facet is not as stable as on the A-polar substrate. Nevertheless, for NWs with a smaller pitch, this rough top-facet disappears and is replaced by the $\{110\}$ facets. All these observations confirm that the $\{110\}$ type facets are extremely stable due to the very low surface energy associated with them [91].

Next, we look at the $[0\,1\,\bar{1}]$-oriented NWs for all growths in Figure 5.4b. Except for the GaAs(Sb) NWs, almost all NWs exhibit an asymmetric cross-section bound by the $\{1\,1\,1\}$ type facets. The AFM topography for the more vertically inclined facet is not reliable due to the inability of the method to obtain information about steep structures. Nevertheless, this tells us that the NWs indeed exhibit the vertical $\{1\,1\,1\}$ facets as expected from the stereographic projections. Perhaps the most interesting observation to be made here is the occurrence of not so sharply defined facets for the GaAs(Sb) NWs on the A-polar substrate (see green arrows). This can possibly be due to the non-reactive nature of the surfactant which is known to decrease the number of incorporation sites for incoming adatoms [95, 96]. However, the GaAs(Sb) NWs on B-polar substrates manifest $\{1\,1\,1\}$B facets despite the presence of Sb. A possible reason for this disparity between the effect of Sb on A- and B-polar surfaces, could be that the B-polar surfaces have an abundance of As, which could facilitate the growth of GaAs; whereas for A-polar surfaces which lack As, a higher As flux might be necessary to incorporate the same amount of material. Nevertheless, Sb is found to lower the material incorporation for NWs on the A-polar substrate, made evident by the lower NW height. It should be noted that NWs with width $W1$ and $W2$ did not grow for the largest pitch for B-polar substrates. This could be due to the the pitch being large enough already where no material was available to source from neighbouring NWs.

Figure 5.5a and b shows the AFM profiles of $[1\,\bar{1}\,\bar{2}]$ and $[0\,1\,\bar{1}]$-oriented GaAs and GaAs(Sb) NWs grown in $(3\,1\,1)$A and B for all different SAG mask dimensions. The AFM data was averaged over a length of $L = 10\,\mu$m and the solid lines correspond the average profile with and the colored band corresponds to the corresponding standard deviation. Each column corresponds to a different growth as labelled on top, with the pitch increasing from top to bottom as $P1 - P4$. Each of the four profiles within each box correspond to the different widths $W1 - W4$.

First, we look at the $[1\,\bar{1}\,\bar{2}]$-oriented NWs for all growths Figure 5.5a. All NWs with pitch $P1$ exhibit an asymmetric cross-section bound by $\{1\,1\,1\}$ and $\{1\,1\,0\}$ type facets. This shape correspond very well with what could be expected from the stereographic projection and taking into account the surface energies of these orientations. As we go higher in pitch from $P2 - P4$, the NWs on the A-polar substrates, exhibit a mix of these facets along with an almost flat-top facet. The fact that no high-symmetry orientations exist at that angle implies that this is an intermediate facet, where the $\{1\,1\,1\}$A and $\{1\,1\,0\}$ facets have not fully formed yet due to less material. The NWs with higher pitch on B-polar substrates however, exhibit a $\{5\,3\,1\}$ type facet instead. This is found from the HAADF-STEM micrographs for GaAs(Sb) NWs on hkl(311) substrates for a fixed width $W3$ and pitch $P2$ presented in

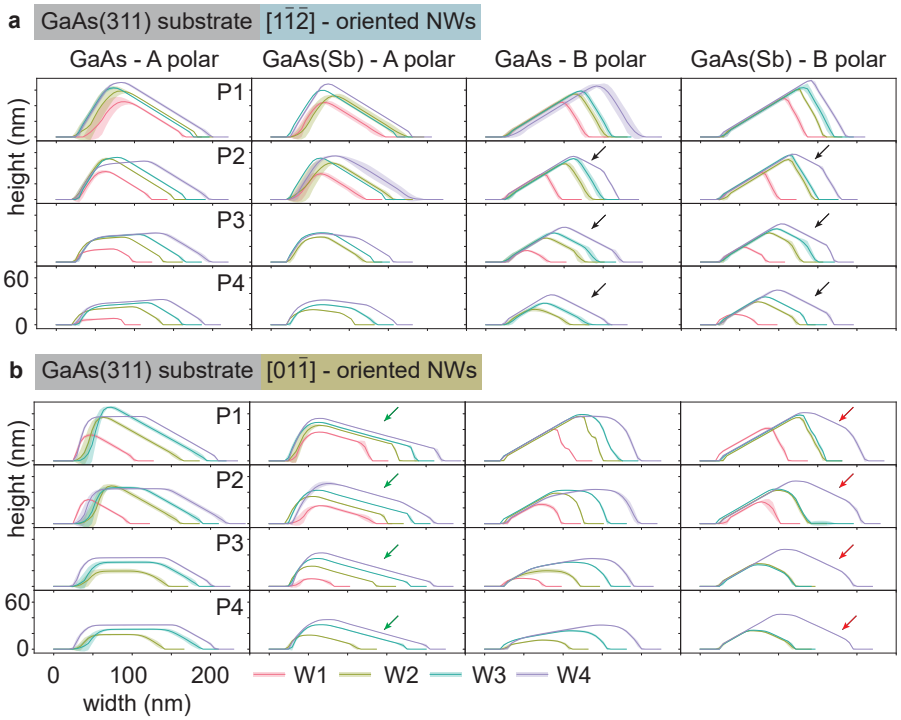

Figure 5.5: AFM topography of **a** $[1\bar{1}\bar{2}]$ and **b** $[01\bar{1}]$-oriented GaAs and GaAs(Sb) NWs on (311)A and B substrates. The columns correspond to different growths, with NWs from arrays with increasing pitch $P1 - P4$, and the 4 AFM profiles in each box corresponds to width $W1 - W4$.

Fig. 5.6, where each column corresponds to multiple NWs from the same individual array (facets labelled at the bottom of the figure). This is the only method to find the orientation for very high-order facets such as $\{531\}$, and thus the intermediate facets occurring for larger pitch on B-polar substrates cannot be identified using AFM (see black arrows).

Finally, we look at the $[01\bar{1}]$-oriented NWs for all growths Figure 5.5b. For pure GaAs NWs on the A-polar substrate, only the NWs with the smallest pitch contain enough material to exhibit the $\{111\}$A type facets. Again, the topography for the highly inclined facet is not completely representative of the actual NW geometry. For NWs with increasing pitch, an intermediate flat top-facet is observed, with a mix of the $\{111\}$A facets. Similar to the $[01\bar{1}]$-oriented GaAs(Sb) NWs on the (211)A (see Fig. 5.4b), these NWs also exhibit a very high-order (533) facets (see green arrows). This facet is identified from the HAADF-STEM data presented in Fig. 5.6. The previously proposed hypothesis for GaAs(Sb) NWs on the (211)A substrate that a lack of As slows down the growth rate, along with Sb atoms lowering nucleation sites for growth to occurs, is strengthened slightly by this consistent observation for the case of the (311)A substrate.

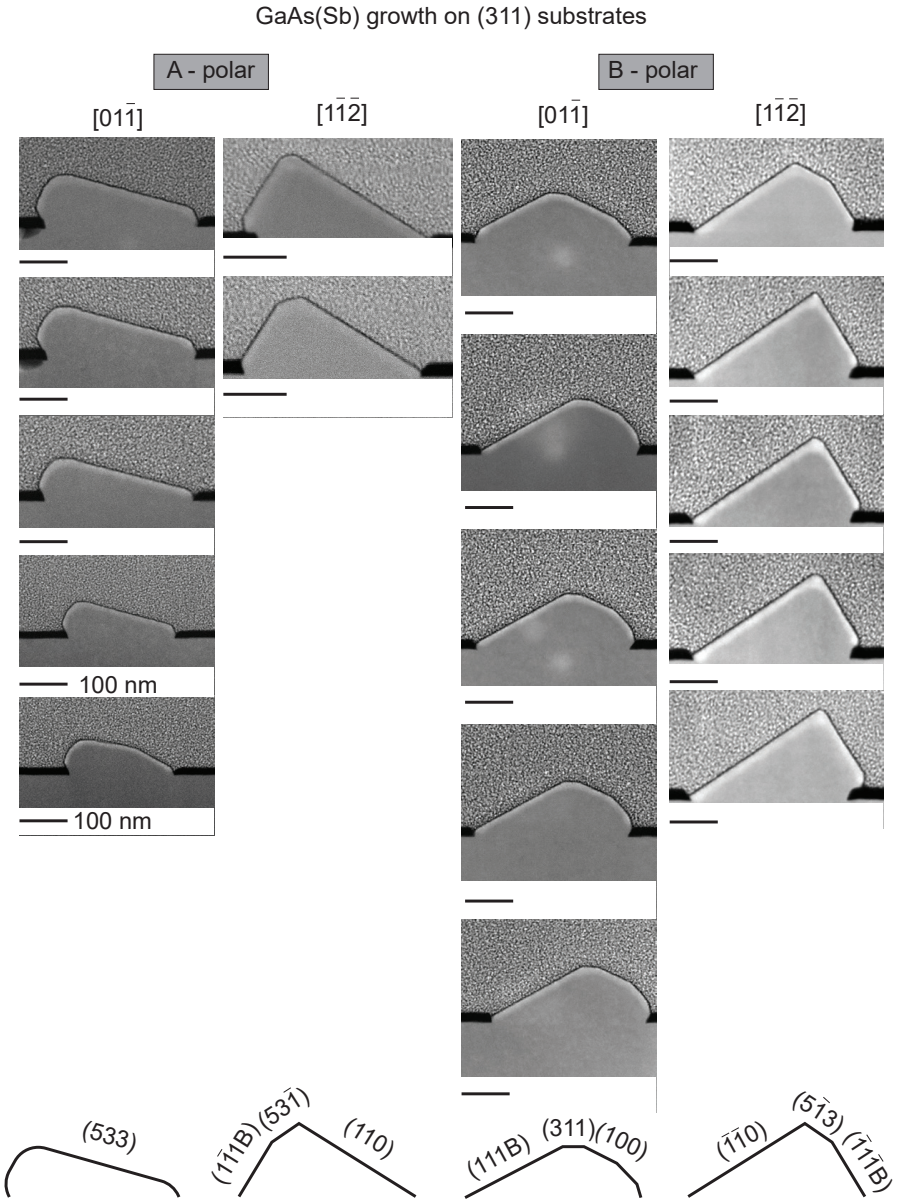

Figure 5.6: Cross-sectional HAADF-STEM micrographs of $[0\,1\,\bar{1}]$ and $[1\,\bar{1}\,\bar{2}]$-oriented GaAs(Sb) NWs on $(3\,1\,1)$A and B substrates. Each column corresponds to NWs from the same array and NW dimensions correspond to width $W3$ and pitch $P2$. Scale bars correspond to 50 nm unless specified otherwise.

It possible that a longer growth time will ultimately result in NWs bound by $\{1\,1\,1\}$A facets as is expected from the symmetry of the substrate. The intermediate facets that manifest for GaAs(Sb) NWs on B-polar substrates (see red arrows) cannot be identified using the AFM data. It should be noted that the NW faceting obtained from HAADF-STEM for the select dimensions and the AFM profiles show a good agreement.

Despite the myriad shapes exhibited by the NWs based on out-of-plane and in-plane orientations, differences arising out of substrate polarity and the use of Sb as a surfactant, the following observations have been consistent: first, NWs grown with a constant width at a larger pitch incorporate less material than at a smaller pitch, and second, NWs grown at a constant pitch with a larger width incorporate more material than with a smaller width. This confirms that the findings of material incorporation in GaAs and GaAs(Sb) NWs on standard GaAs(1 0 0) substrates in publication [22], Ga adatoms show a sourcing behaviour (see Section 2.5) at the growth conditions used in this study, with different substrates.

5.4 Material incorporation

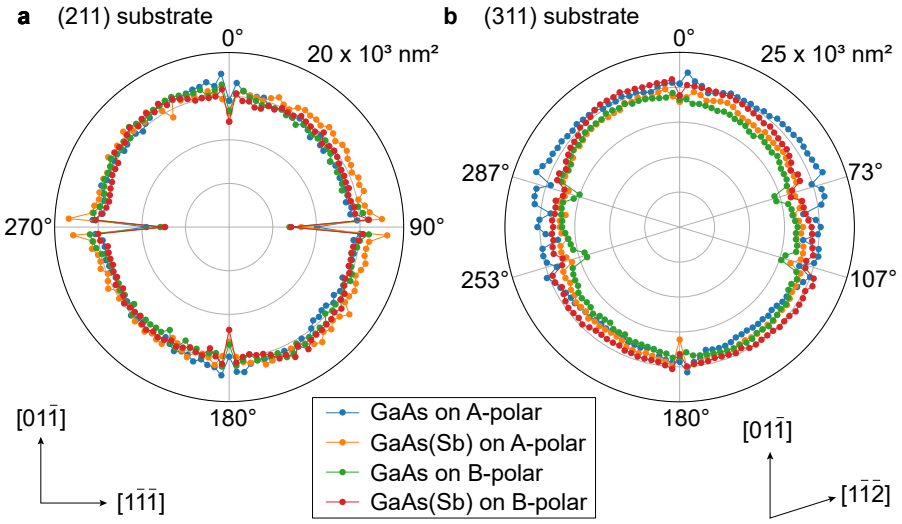

Figure 5.7: Polar plot depicting the individual NW volume of 120 GaAs and GaAs(Sb) NWs grown on **a** GaAs(2 1 1)A and B and **b** on GaAs(3 1 1)A and B as a function of in-plane orientation. All NWs are spaced 3° apart.

In this section, we analyze the NW volume from all growths on different substrates as a function of in-plane orientation. Figure 5.7a and b shows polar plots of the GaAs and GaAs(Sb) NW volume of NWs grown on (2 1 1)A (B) and (3 1 1)A (B) substrates, respectively. The method for extracting NW volume is the same as the one presented in Section 4.4. The data corresponds to 120 NWs arranged in a circular array in steps of 3°. The $[0\,1\,\bar{1}]$, $[1\,\bar{1}\,\bar{1}]$, $[0\,\bar{1}\,1]$, and $[\bar{1}\,1\,1]$ directions correspond to $0°, 90°, 180°$ and $270°$, respectively. As seen already for GaAs(Sb) NWs grown on a (2 1 1)B substrate, the NW volume shows a stark decrease for NWs oriented along the high-symmetry orientations. The reason for this trend has already been addressed in depth in Section 4.4. Interestingly, it is observed that all growths

follow the same trend. It is possible that the GaAs(Sb) NWs along the high-symmetry orientations, incorporate the least amount of material, but since the difference compared to NWs from other growths is quite small, and the fact that this data only corresponds to a single NW per orientation, it is difficult to make conclusions. Another interesting observation to be made it that the NWs in between the high-symmetry in-plane directions show no preferential material incorporation based on the substrate polarity or the use of Sb. Finally, the difference in NW volume along the two high-symmetry orientations allows to hypothesize that the relative diffusion length along the $[1\,\bar{1}\,\bar{1}]$ direction might be longer than the $[0\,\bar{1}\,1]$, but this is difficult to conclude due to the added complexity of developing NW facets.

In the case of $(3\,1\,1)$ substrates showed in Fig. 5.7b, the $[0\,1\,\bar{1}]$, $[1\,\bar{1}\,\bar{2}]$, $[1\,\bar{2}\,\bar{1}]$, $[0\,\bar{1}\,1]$, $[\bar{1}\,1\,2]$, and $[\bar{1}\,2\,1]$ directions correspond to $0°, 73°, 107°, 180°, 253°$ and $287°$, respectively. The $\langle 1\,1\,2\rangle$ directions are actually $\sim 1°$ away from the highlighted directions in the plot, and were not aligned exactly at the correct directions. Despite this, once again it is observed that the NWs aligned along high-symmetry in-plane orientations constitute a lower volume compared to all the other NWs irrespective of the substrate polarity or use of Sb. The decrease in volume of the aligned NWs does not show a stark difference between themselves when compared to the the two high-symmetry orientations of the $(2\,1\,1)$ substrates. No obvious trend is observed for the misaligned NWs based on this study. It should be noted that the overall volume for NWs on the $(3\,1\,1)$ substrates is higher than those of the $(2\,1\,1)$ substrates. This could be attributed to fabrication related differences, and growth related changes. But importantly, the data for the growths on all $(2\,1\,1)$ (and $(3\,1\,1)$) substrates can be compared meaningfully since all samples correspond to the simultaneous fabrication of substrates and were grown using the same MBE across 2 days.

5.5 Conclusions

A detailed AFM study of the NW morphology dependent on the substrate out-of-plane and in-plane orientations has been presented. It was found that the substrate polarity and the use of Sb as a surfactant also influence the shape of the NWs. Additionally, due to the SAG mask dimension dependent growth rates, the shape of the NW was further influenced by the width and inter-wire distance. This study has demonstrated that the by carefully designing the SAG mask, it is possible to experimentally determine the evolution of NW faceting. This is possible because due to the adatom kinetics governing the behaviour Ga adatoms cause NWs that are closely spaced together to share the incoming flux due to adatom diffusion on the SAG mask. Thus, increasing inter-wire distance allows to obtain NWs at an effectively earlier stage of growth. Decreasing width has the opposite

effect where, NWs width smaller widths represent a relatively later stage of NW faceting because the amount of material required to fully develop facets is less compared to larger widths. The GaAs(Sb) NW cross-sectional shapes obtained from HAADF-STEM for select NW dimensions on $(3\,1\,1)$A show good agreement with the NW topography obtained using AFM. The persistence of $\{1\,1\,0\}$ type facets on the $[1\,\bar{1}\,\bar{1}]$-oriented NWs, despite changing substrate polarity, using Sb and varying mask dimensions, confirms the stability of this non-polar surface. Moreover, it has also been demonstrated that the Sb as a surfactant has a stronger effect on both $(2\,1\,1)$ and $(3\,1\,1)$A-polar substrates for certain in-plane orientations. Finally, the NW volume dependence on the in-plane orientation has been demonstrated. It is consistently observed that NWs grown along the high-symmetry in-plane orientations exhibit lower volume than the misaligned NWs. This shows that the Ga adatoms have relatively longer diffusion lengths along those directions and are thus incorporated less into the NW growth. This is observed irrespective of the substrate polarity and use of Sb and it is beautiful to see the consistency with which Ga adatoms behave.

Part III

Hetero-epitaxy of **InAs**

The hetero-epitaxial growth of InAs nanowires mediated by GaAs(Sb) buffer layers on GaAs(311)A substrates is considered in depth. The reproducibility of the structural characteristics of the nanowires is quantified. The effect of varying SAG mask dimensions on the nanowire morphology is characterized using various microscopy methods. The reproducibility of the electrical characteristics is tested using a multpilexer/de-multiplexer set-up. The structural and electrical characteristics of the nanowires are found to be correlated.

6

Structural Characteristics

The results presented in this chapter overlap partially with manuscript [4] :

Dimension dependent electrical transport in planar InAs nanowires
G Nagda, D Olsteins, S M-Sánchez, D V Beznasyuk, D J Carrad, C E N Petersen, J Nygård, J Arbiol, T S Jespersen
In preparation

The high-angle annular dark field scanning transmission electron microscopy, corresponding geometric phase analysis, and electron energy loss spectroscopy results presented in this chapter were acquired by **Dr. Sara Martí- Sánchez** and **Christian Koch** under the supervision of **Prof. Dr. Jordi Arbiol** affiliated with the Catalan Institute of Nanoscience and Nanotechnology (ICN2), CSIC and BIST, Campus UAB, Bellaterra, Barcelona, Catalonia, Spain.

6.1 Introduction

Field effect mobility has been shown to have a dependence on the interface of the InAs NWs with the underlying substrate [97] where introducing a GaAs buffer layer enhanced the mobility. Moreover, the use of ternary InGaAs buffers atop the GaAs buffers have also showed an enhancement in the transport characteristics of the InAs channel. However, the composition of the ternary buffer and the InAs channel is highly dependent on the growth parameters and requires a systematic approach at optimization. Therefore, we consider a simplified heterostructure in this this chapter. The results of the selective area grown InAs NWs on GaAs(3 1 1)A substrates mediated by a GaAs(Sb) buffer are discussed. Extensive AFM analysis of these samples is carried out and the $[0\,\bar{1}\,1]$-oriented NWs are chosen for further detailed structural (presented here) and electrical transport measurements (presented in the following Chapter 7). Reproducibility in structural characteristics of 180 NWs is quantified using AFM as the primary tool. Furthermore, the dependence of the NW morphology on the SAG mask dimensions such as width (W) and in-plane orientation (θ) is discussed with supplementary results from HAADF-STEM and EELS of select NW dimensions. Varying W gives us the opportunity to the study the different stages of InAs growth, whereas varying θ allow us the track the influence of the unintentional mis-orientation associated with SAG substrate manufacturing as discussed in Chapter 4.

6.2 Experiment

We begin by studying the influence of growth time of the InAs layer on the resulting NW morphology. For this, 4 samples are grown. Using the substrate fabrication methods presented in Appendix A, a single 2 inch GaAs(3 1 1)A substrate was prepared for SAG, then scribed into quarters and subsequently used for the following growths where all growth parameters were kept identical except for the InAs growth time (see Fig. 6.1 and Table 6.1):

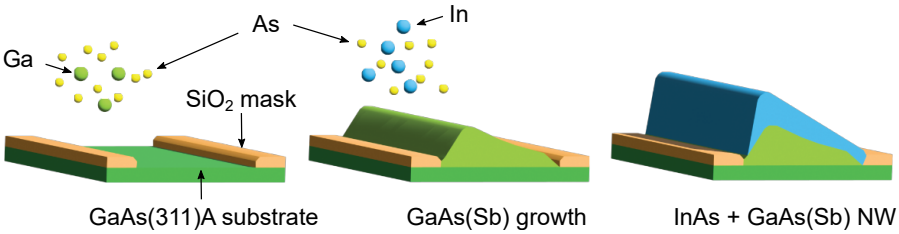

Figure 6.1: Schematic of SAG of $[0\,\bar{1}\,1]$-oriented InAs/GaAs(Sb) dual layer NWs on GaAs(3 1 1)A, representative only for a fixed set of mask dimensions and growth parameters.

Figure 6.1 shows a schematic of a typical SAG of $[0\bar{1}1]$ oriented InAs + GaAs(Sb) NWs, representative only for a certain dimension and MBE growth parameters implemented in this experiment.

Sample no.	GaAs(Sb) growth time	InAs growth time
1	30 min	– (reference sample)
2	30 min	5 min
3	30 min	10 min
4	30 min	18 min

Table 6.1: 4 samples used to study the influence of InAs growth time on the NW morphology.

All samples have been fabricated with the same SAG mask design consisting of arrays of 9 different different widths of the mask opening ($W1 - W9$) ranging from $100 - 400$ nm and in-plane orientations in a range of ($\theta = \pm 5°$) in steps of 0.5° away from the $[0\bar{1}1]$ direction. All arrays have the same pitch $P = 2\,\mu$m. The samples are also expected to have the same fabrication related tolerances. The growth parameters for GaAs and InAs growth are presented in detail in the Appendix B.

InAs growth time

In the following, the results from varying InAs growth time (see Table 6.1) are presented are discussed. AFM is used to study the $[0\bar{1}1]$-oriented NWs with three different widths corresponding to $W1 = 100$ nm, $W5 = 220$ nm and $W9 = 400$ nm from 4 samples (see Fig. 6.2). It is observed that for sample 2 with the shortest growth time of 5 min (Fig. 6.2 (top)), the InAs layer is discontinuous for all widths. Increasing the time to 10 min for sample 3 resulted in NWs with width $W5$ and above to have a discontinuous InAs layer, while thinner NWs exhibit a continuous layer of InAs as can be seen in Fig. 6.2 (middle). Increasing the InAs growth time further (sample 4, 18 min), a continuous layer is observed for widths $W1$, $W5$ and $W9$. This can be seen from the 3D AFM topographies presented in F.g 6.2 (bottom). This can be explained by the fact that due to the InAs/GaAs lattice mismatch of $\sim 7.7\%$, the InAs growth is highly strained and result in Stranski-Krastanov growth. (see Section 2.4). For smaller widths, since less amount of material is required to cover the underlying GaAs(Sb) buffer, this 3D growth has the possibility to merge and minimize the overall surface energy by formation of well-defined facets. However, for larger widths, more material would be required to achieve the same. Thus, NWs from sample 4 with the longest growth time exhibit a continuous InAs layer for a larger range of widths compared to the other samples.

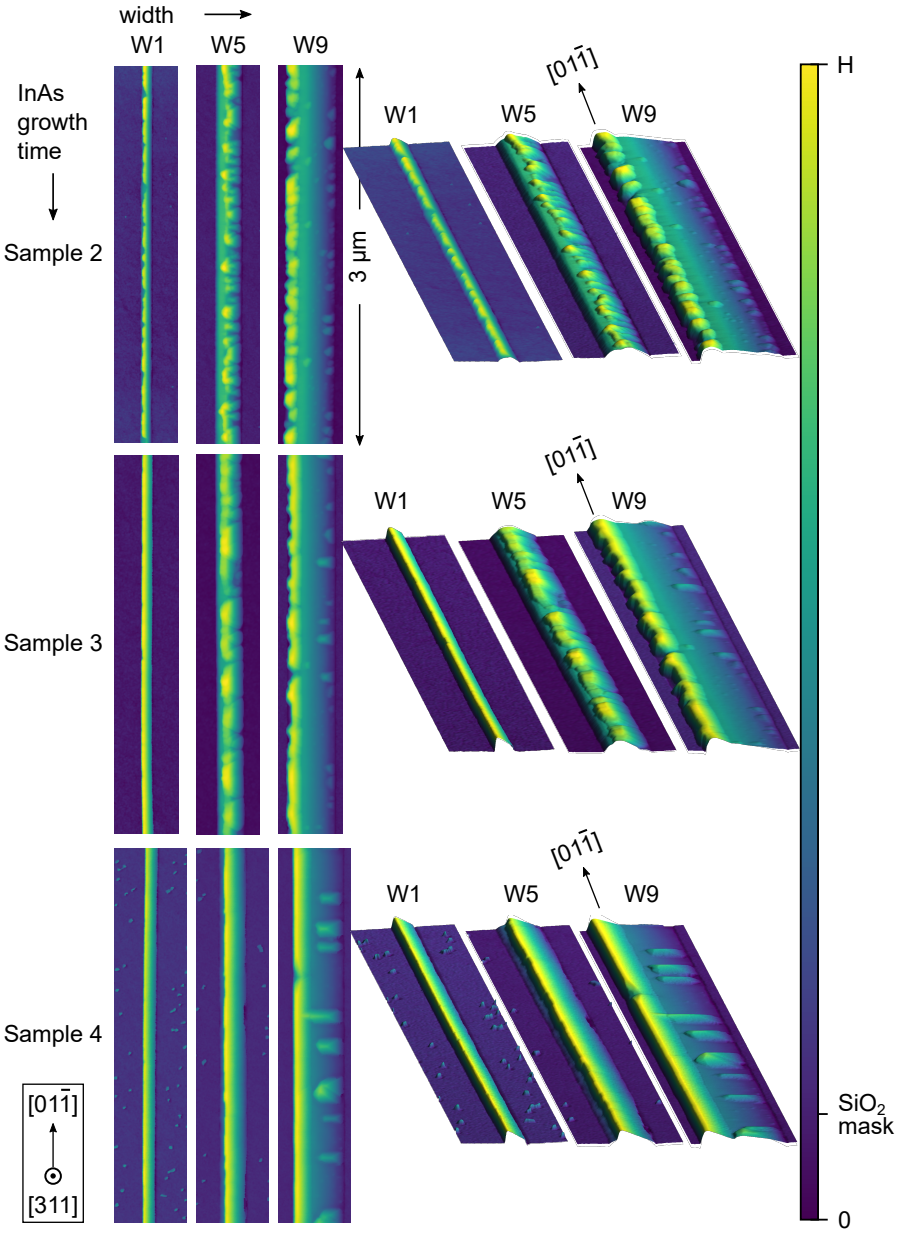

Figure 6.2: Top-view and 3D AFM topography of $[0\,1\,\bar{1}]$-oriented NWs with width $W1$, $W5$ and $W9$ from three different Samples 2, 3 and 4 (see Table 6.1). Top (middle, bottom) row corresponds to InAs growth time of 5 min (10 min, 18 min).

Nanowire volume

In the following, the incorporation of material (NW volume) dependent on the in-plane orientation is discussed. Samples 1 and 4 are considered as the two extremes, no InAs growth and longest InAs growth time, respectively. InAs/GaAs(Sb) and GaAs(Sb) NWs were grown in a circular array along all in-plane orientations on in steps of 3°, with a constant mask opening width of $W = 150\,\text{nm}$. AFM

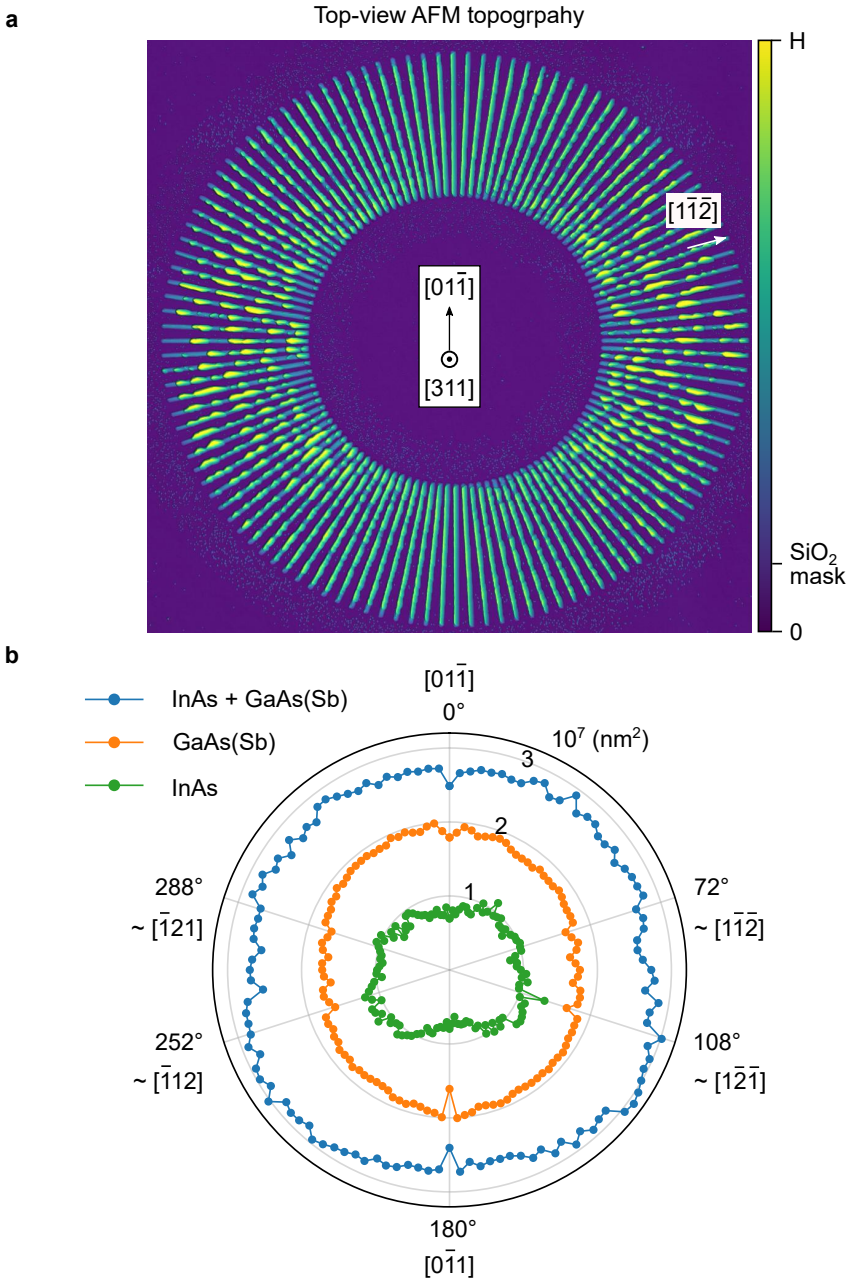

Figure 6.3: **a** Top-view AFM topography of circular array of InAs/GaAs(Sb) dual layer NWs. **b** Polar plot depicting the individual NW volume of 120 InAs/GaAs(Sb) (blue) and GaAs(Sb) (orange) NWs grown on GaAs(3 1 1)A as a function of in-plane orientation (θ) in steps of 3°. The subtracted volume gives the distribution of amount of InAs (green).

was performed on such arrays from sample 4, with the longest InAs growth time (see Fig. 6.3a) to determine if there was a preferential distribution of material. Figure 6.3b depicts the volume extracted from AFM of all 120 NWs from sample 4 and sample 1 (reference sample). The volume distribution for the GaAs(Sb) NWs shows a decrease

at 0°, 72°, 108°, 180°, 252° and 288°. These locations correspond to the high-symmetry orientations as labelled, although the ⟨1 1 2⟩ directions are 1° away from the labelled orientations. The decrease in material incorporation can be explained by the longer Ga adatom diffusion lengths along these directions. Mis-orientation from these directions results in stepped NW surfaces that act as nucleation sites for incoming adatoms and result in increased material incorporation (see Section 4.4). Away from the high-symmetry orientations, the volume distribution is approximately the same and does not reveal an underlying trend.

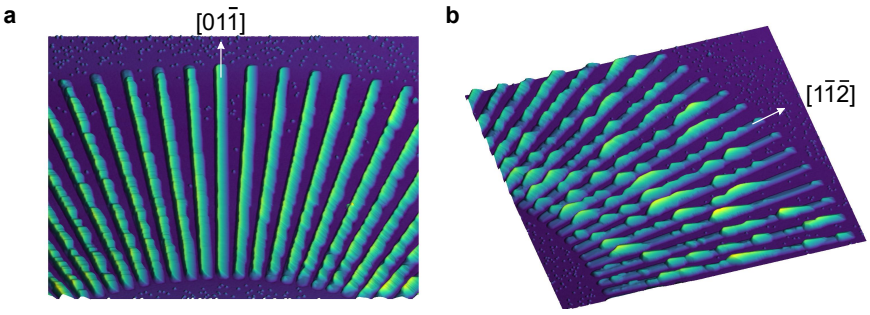

Figure 6.4: a, (b) Close-up 3D AFM topography of the [0 1 $\bar{1}$] ([1 $\bar{1}$ $\bar{2}$]) - oriented NWs, titled 45° away from the [3 1 1] zone axis. They highlight the continuous InAs morphology in case of the [0 1 $\bar{1}$]-oriented NWs whereas a high density of island growth is visible for [1 $\bar{1}$ $\bar{2}$]-oriented NWs.

The InAs/GaAs(Sb) NWs follow the same trend for the ⟨1 1 0⟩ orientations, however the ⟨1 1 2⟩ orientations show no decrease. While the [0 1 $\bar{1}$]-oriented NWs show a continuous morphology, interestingly, a high density of 3D island growth is observed along the ⟨1 1 2⟩-oriented NWs (see Fig. 6.4a and b respectively). Despite the well-defined facets of the underlying GaAs(Sb) layer for these orientations (see Section 5.2, Fig. 5.5a), the InAs layer does not follow the formation of the underlying facets and instead remains in the form of 3D islands atop the buffer layer. It is possible that the In adatom diffusion length along the ⟨1 1 2⟩ directions (NW axis) is unfavourably short and does not allow for merging of the islands, although not much research exists in relation to this hypothesis. A more likely explanation could be that since the underlying GaAs(Sb) NW exhibits a combination of polar (1 1 1)A and non-polar (1 1 0) facets, the InAs growth conditions are not optimal for simultaneous growth on either facets. It has also been shown that during MBE growth, there exists net inter-diffusion of In adatoms across [1 1 1]A - (1 0 0) facets, the direction and flux of which is highly dependent on the growth conditions [98]. It is possible that a similar preferential diffusion across the underlying facets is favoured in one direction, resulting in increasing 3D growth. For the [0 $\bar{1}$ 1]-oriented NWs, the underlying low-symmetry (5 3 3) facet is A-polar

and thus the In adatoms likely do not have to overcome a change on polarity, facilitating the diffusion of In adatoms along this direction. The distribution of the InAs/GaAs(Sb) volume away from the $\langle 1\,1\,0 \rangle$ directions can be seen in the top-view AFM topography of the array Fig. 6.3b. Subtracting the volumes to obtain the distribution of only InAs reveals no underlying trend and it can be concluded that it is distributed randomly along all NWs except the ones oriented along the $[0\,1\,\bar{1}]$ and $[0\,\bar{1}\,1]$ directions.

Nanowire faceting

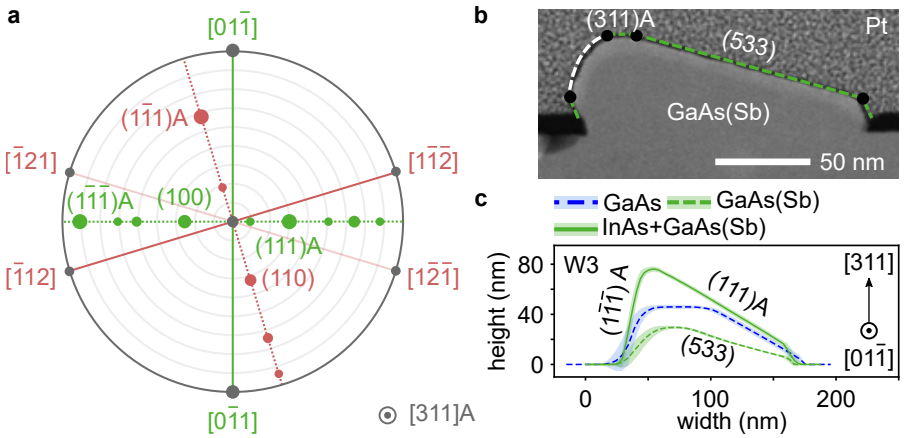

Figure 6.5: a Stereographic projection of the $[3\,1\,1]$ zone axis of a Zinc Blende (ZB) crystal. The $(3\,1\,1)$ substrate exhibits two high-symmetry in-plane orientations, of which the $[0\,\bar{1}\,1]$ oriented NWs form the basis of this study. The corresponding facets that the NWs can exhibit are given by the poles situated on the normal (dotted lines) to the NW orientation (solid lines). **b** Cross-sectional HAADF-STEM micrograph of a NW with width *W*3 with an overlaid schematic of the facet labels. **c** AFM profiles of NWs of the same dimension from the reference GaAs(Sb) sample and the InAs/GaAs(Sb) sample. Solid and dashed lines correspond to the profiles averaged along a 1 μm long segment, with the standard deviation showed as colored bands.

Figure 6.5a shows a stereographic projection that reveals the crystallographic symmetry of the $[3\,1\,1]$ zone axis of a Zinc Blende (ZB) crystal. To know more about the symmetry associated with the $(3\,1\,1)$ substrate orientation, please refer to Section 5.2. The poles on the outermost circle correspond to high symmetry in-plane orientations on the $(3\,1\,1)$ surface. There are 2 sets of families of high-symmetry orientations for the $(3\,1\,1)$ zone axis, namely the $[0\,\bar{1}\,1]$ (equivalent to $[0\,1\,\bar{1}]$) and $[1\,\bar{1}\,\bar{2}]$ (equivalent to $[\bar{1}\,1\,2]$, $[1\,\bar{2}\,\bar{1}]$, $[\bar{1}\,2\,1]$) along which NWs can be expected to exhibit well defined facets. The possible facets that the NWs can exhibit is indicated by the poles occurring along the

normal (dotted lines) to the NW direction (solid lines), marked by the same color.

As discussed in Section 2.6, the actual facets that the NWs exhibit depend on the set of of mask design parameters such as width, length and the proximity to another NW (pitch); and growth parameters such as T_{sub}, V/III flux ratio, use of surfactants, growth rates as well as growth time. Figure 6.5b shows a cross-sectional HAADF-STEM micrograph of GaAs(Sb) NW oriented along the $[0\bar{1}1]$ direction (corresponding to sample 1, see Table 6.1). They differ from the ones observed for pure GaAs growth as seen in the AFM topography presented in Fig. 6.5c. Pure GaAs NWs develop $\{1\,1\,1\}$A facets as opposed to the GaAs(Sb) NWs which manifest a very low-symmetry $(5\,3\,3)$ facet, along with a combination of multiple high-order facets that result in a rounded shape (highlighted in white dashed lines). These facets do not correspond to the expected shape associated with the symmetry of the substrate, and the possible reasons have been discussed in Section 5.2 (see Fig. 5.6). On the other hand, when InAs is grown atop the GaAs(Sb) NW, it acquires the $\{1\,1\,1\}$A facets as expected as seen in Fig. 6.5c. Even though it remains unclear why, it can be concluded that for the set of growth conditions used in this study, Sb modifies the surface energy to promote the growth of high index (low symmetry) $(5\,3\,3)$ facets.

Thus the remainder of the analysis is only performed on $[0\bar{1}1]$*-oriented NWs from sample* 4 *which exhibit well-defined facets for the InAs layer for most number of widths.*

6.3 Reproducibility

In this section, the reproducibility of the structural characteristics such as NW height (H) and facet length (F) of $[0\bar{1}1]$-oriented InAs/-GaAs(Sb) SAG NWs from sample 4 is investigated. Although the SAG NWs were defined identically, several effects lead to structural variations at different length-scales both within individual NWs and between NWs across the arrays. Stacking faults and misfit dislocations due to lattice mismatch between the underlying GaAs(Sb) and InAs along with material intermixing caused by Ga diffusion (discussed later in Section 6.4.2) during InAs growth are the causes for variations on the microscopic level in the InAs SAG NW. These effects result in variations in the NWs on the $5-10\,\text{nm}$ scale but the effects on electrical transport (dsicussed later in Chapter 7) in micro-meter scale devices can be expected to be effectively averaged. On the larger scale, etching induced line edge roughness (typically $1-2\,\text{nm}$) of the mask openings translates to structural variation of NW topography. Variations can also extend along the NW with a length scale set by the diffusion length of In and Ga adatoms due to increasing diffusion

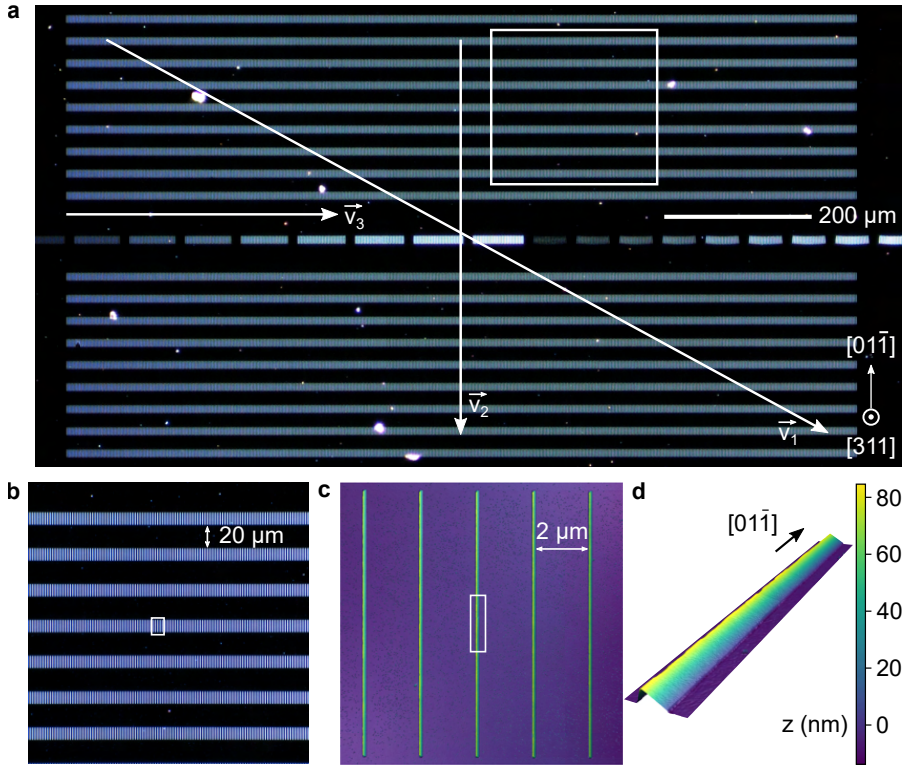

Figure 6.6: **a** Dark-field optical microscope micrograph of arrays of SAG NWs used to quantify the reproducibility in structural and electrical characteristics. Vectors $\vec{v}_1$ and $\vec{v}_2$ indicate the directions along which the AFM measurements for subsequent statistical analysis were taken. **b** Close-up of the region highlighted in **a**, the distance between each layer of NW arrays is 20 μm. **c** AFM micrograph of 5 SAG NWs, the inter-wire distance in the NW array is $P = 2\,\mu$m. **d** 3D AFM topography of a segment of a single SAG NW segment highlighted in **c**.

of adatoms from the ends of the growing crystal to the surrounding mask [22].

To investigate such variations, topographic AFM images of NWs from a large array were analyzed. Figure 6.6a and b show a dark-field optical microscope of the entire array and a close-up of the highlighted region, respectively. The NWs are arranged in 512×16 arrays with an inter-wire distance of $P = 2\,\mu$m and an inter-array distance of $20\,\mu$m. Figure 6.6c shows an AFM micrograph of 5 SAG NWs along with a 3D representation of a single NW presented in Fig. 6.6d. AFM was performed on 1 μm long segments of NWs from approximately the middle region of the NWs. The choice of the segment length corresponds to the channel length used for electrical characterization. Scans consisted of 5 NWs from each array, approximately along $\vec{v}_1$ (diagonal across the entire array), and along $\vec{v}_2$ (vertical across the entire array) as indicated in Fig. 6.6a. A total of 180 NWs were imaged

to determine a positional dependence on the structural characteristics from the $\sim 1.0\,\text{mm} \times 0.6\,\text{mm}$ large NW array.

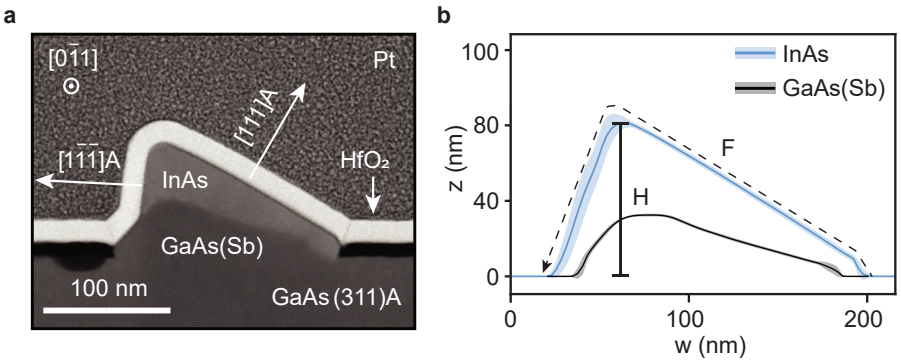

Figure 6.7: a HAADF-STEM micrograph of a cross-section of a InAs/-GaAs(Sb) SAG NW from sample 4 used for the structural and electrical characterization. The NW exhibit an asymmetric cross-section bound by $\{1\,1\,1\}$A facets. **b** The mean AFM profiles of an InAs/GaAs(Sb) NW and a GaAs(Sb) buffer layer (solid lines) averaged over 9 μm and 2 μm long NW segments respectively. The colored bands show the standard deviation. F is the measure of the facet length and H is the height measured from the SiO_2 mask to the highest point on the NW.

A cross-sectional HAADF-STEM micrograph of a $[0\,\bar{1}\,1]$-oriented dual layer InAs/GaAs(Sb) NW with SAG mask dimensions of: $W4 \sim 175\,\text{nm}$ and $L = 10\,\mu\text{m}$, is shown in Fig. 6.7a. The NWs exhibit an asymmetric NW shape bound by $\{1\,1\,1\}$A facets in the InAs region with an underlying GaAs(Sb) buffer exhibiting a combination $(5\,3\,3)$ and multiple high-order facets which result in a rounded shape. Figure 6.7b shows a typical AFM mean profile (solid lines) of the InAs/-GaAs(Sb) and GaAs(Sb) NWs averaged over length of 9 μm and 2 μm respectively. The standard deviation is depicted as the colored bands.

For InAs NWs, electronic transport at cryogenic temperatures is usually dominated by a surface accumulation layer and thus in the simplest case, the conductance is expected to be proportional to the facet length F. Figure.6.8a and b show F and the NW maximal height H respectively along the length of a single NW, excluding 500 nm from both ends to eliminate the contribution from differing end facets. The corresponding running averages shown are sampled over a 1 μm long window since this length constitutes the active element of the NW field effect transistors in the electrical devices and the effects from variations within a window smaller than the channel length will be effectively averaged.

Figure6.9a and b show F and H averaged over a 1 μm long segment from approximately the center of the NWs (180 individual NWs along the vectors $\vec{v}_1$ and $\vec{v}_2$ in Fig.6.7a). There is a similar systematic linear trend observed in $\langle H \rangle$ between the NWs along the $\vec{v}_1$ and $\vec{v}_2$

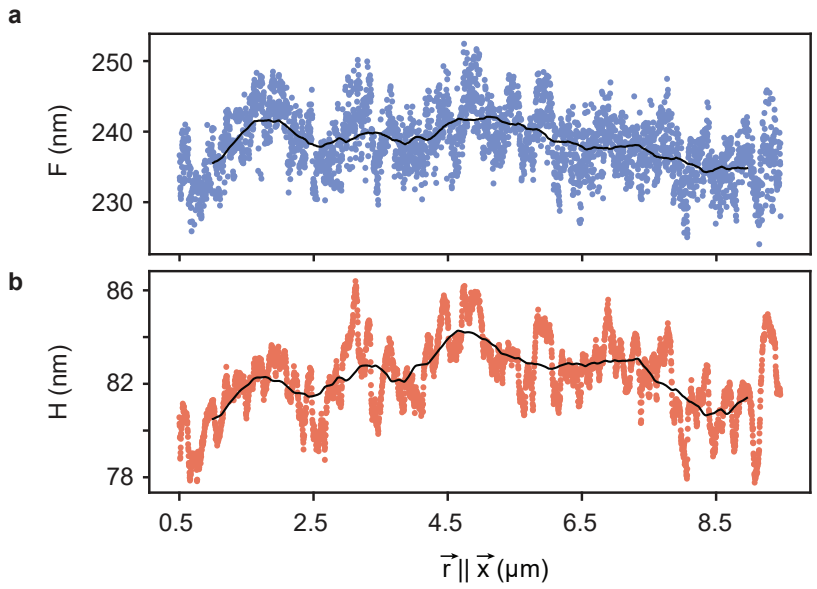

Figure 6.8: a, (b) F (H) along the length of a single NW disregarding the $0.5\,\mu$m long segments at the ends of the NW. The black line indicates the running average value over a $1\,\mu$m long window.

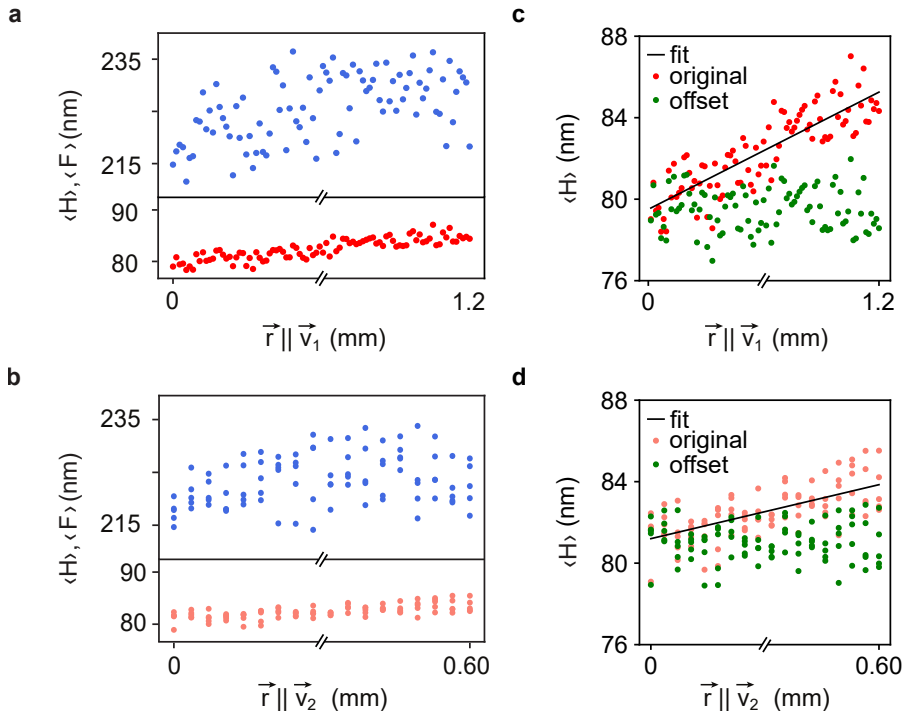

Figure 6.9: a (b) $\langle F \rangle$ and $\langle H \rangle$ over $1\,\mu$m long NW segments taken approximately along $\vec{v}_1$ ($\vec{v}_2$). **c (d)** show $\langle H \rangle$ along $\vec{v}_1$ ($\vec{v}_2$), with the original data, a linear fit and the linear fit subtracted from the original data, labelled as offset data.

directions. This systematic variation can be attributed to large scale fluctuations in the growth parameters across the substrate such as substrate temperature and material fluxes taking into account the large size of the NW array. However, the similarity in the trends in $\langle H \rangle$ along the $\vec{v_1}$ and $\vec{v_2}$ directions also means that the variation along $\vec{v_3}$ must be negligible. Thus, a linear fit is performed on the original $\langle H \rangle$ along the $\vec{v_1}$ and $\vec{v_2}$ directions to estimate the systematic variation and presented in Fig. 6.9c and d respectively. This is then offset from the original data by subtracting the linear fit. The overall slopes along $\vec{v_1}$ is 4.8 nm and along $\vec{v_2}$ is 4.6 nm.

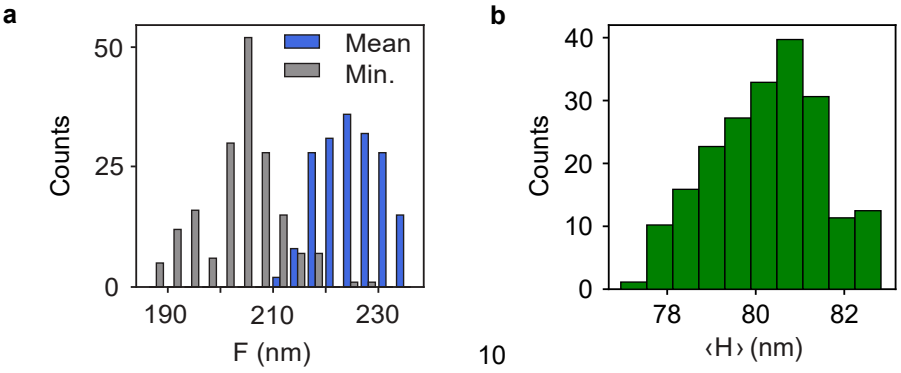

Figure 6.10: a Histograms of $\langle F \rangle$ and F_{min} across 180 NWs. **b** Histogram of $\langle H \rangle$ across 180 NWs.

The distributions of the mean and minimum F and the offset $\langle H \rangle$ of all 180 NWs within the large array are shown in Fig.6.10a and b respectively. $\langle F \rangle$ and $\langle H \rangle$ give a possible estimate of the variation of the conduction channel in the NWs while exceptionally narrow segments F_{min} can behave as bottlenecks that can limit conductance. $\langle F \rangle = 225.7\,\text{nm}$ and $\langle H \rangle = 80.2\,\text{nm}$ Although all growth and fabrication parameters were kept constant across the SAG NW array, the local variations lead to a normalized standard deviation of $\sigma_F / \langle F \rangle = 2.56\,\%$. The normalized standard deviation for the NW height on the other hand, $\sigma_H / \langle H \rangle = 1.55\,\%$, is significantly smaller. The microscopic and large-scale structural variation of nominally identical SAG NWs have the potential to influence the electrical characteristics of SAG quantum devices. Thus it is important to quantify the variations and use it as a metric to compare the quality of NWs across different samples and eventually improve structural reproducibility.

6.4 Effect of mask dimensions and orientations

After quantifying the structural reproducibility of the InAs/GaAs(Sb) SAG NWs for a fixed dimension, it is useful to consider the effect of varying mask dimensions on the NW morphology. AFM is used to study the influence of W and θ on the structural characteristics such as

cross-sectional area (A) and facet roughness (S_q). The NWs considered here have 9 varying widths ($W1$ - $W9$) which correspond to a range of $\sim 100\,\text{nm}$ to $\sim 400\,\text{nm}$. For all widths, NWs grown along the $[0\bar{1}1]$ direction and mis-oriented with respect to it by maximally $\theta = \pm 4.5°$ in increments of $0.5°$ are considered.

6.4.1 *Morphology*

Varying width

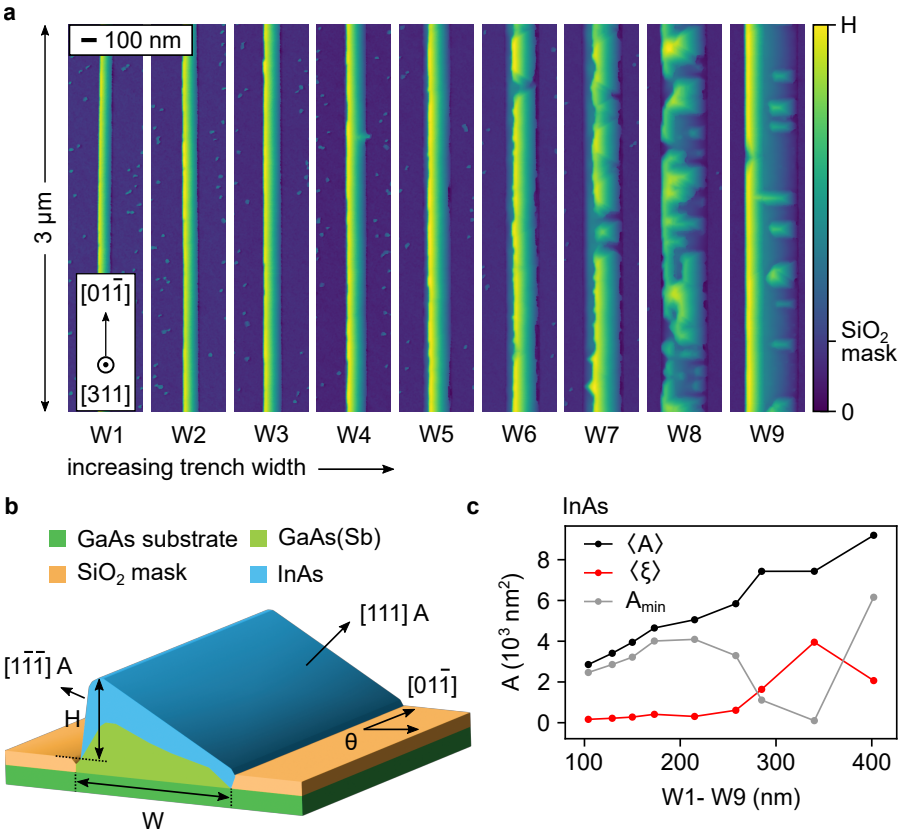

Figure 6.11: **a** Top-view AFM topography of the $3\,\mu$m long segments of NWs for widths $W1$ -$W9$ increasing from left to right. The color bar shows the height distribution where H represents the maximal height for all NWs. **b** Schematic of a typical $[0\bar{1}1]$-oriented InAs/GaAs(Sb) NW bound by $\{1\,1\,1\}$A facets, with the maximal NW height (H), width (W) and in-plane orientation (θ) as labelled. **c** Width dependence of the average cross-sectional area ($\langle A \rangle$) of the NWs, the minimum area (A_{min}) and the average of the variation in A, presented again for completeness.

Top-view AFM topography of $3\,\mu$m long segments of NWs with increasing trench width from $100 - 400\,\text{nm}$ is shown in Fig. 6.11a. The NWs with width $W1$ - $W5$ show the existence of a continuous InAs layer, however for wider NWs, the amount of InAs is not enough to

completely cover the underlying GaAs(Sb) layer. Figure 6.11b shows a schematic representation of a typical $[0\,\bar{1}\,1]$-orientated InAs/GaAs(Sb) NW corresponding to width $W4$ on a GaAs$(3\,1\,1)$A substrate. The asymmetric cross-section of the NW bound by $\{1\,1\,1\}$A facets (for the InAs region) is a result of the substrate and in-plane orientation of the NW. The underlying GaAs(Sb) layer is not bound by high-symmetry facets as a result of the use of Sb as a surfactant during GaAs buffer growth. The NW width is a measure of the width of the mask openings (and equivalently corresponds to the width of the GaAs(Sb) buffer) whereas the maximal height (H) is a measure of the highest point along the InAs channel with respect to the SiO_2 mask (see Fig. 6.11b).

To quantify the InAs coverage, the corresponding average cross-sectional area of the InAs region ($\langle A \rangle$), the minimum area (A_{min}) and the average of the variation in A along a length of $3\,\mu$m ($\langle \xi \rangle$), the values for GaAs(Sb) are subtracted from the InAs+GaAs(Sb) (see Fig. 6.12b) and plotted as a function of W in Fig. 6.11c. For $W1$ -$W5$, $\langle A \rangle$ and A_{min} scale linearly, while $\langle \xi \rangle$ remains very small. However, for wider NWs, A_{min} no longer scales as $\langle A \rangle$ and $\langle \xi \rangle$ increases significantly.

Cross-sectional area

The cross-sectional area A is extracted for InAs/GaAs(Sb) dual layer NWs (Fig. 6.12a, left) and GaAs(Sb) NWs (Fig. 6.12a, right) over a $3\,\mu$m long segment from approximately the central region, for widths $W1$ -$W9$. With increasing width, the variation in A for the InAs/GaAs(Sb) NWs increases significantly due to insufficient amount of InAs. The GaAs(Sb) NWs exhibit a homogeneous A along the length, however, there is an overall slope for all widths which arises from the decreasing material incorporation towards the ends of the NWs. This means that it is likely that the AFM data was acquired further away from the central region in this case. This variation along the length is further discussed below. The corresponding average cross-sectional area ($\langle A \rangle$) of the InAs/GaAs(Sb) and GaAs(Sb) NWs, the minimum area (A_{min}) and the average of the variation in A ($\langle \xi \rangle$) calculated from the data in Fig. 6.12a is presented in Fig. 6.12b, left and right respectively. It can be concluded that the GaAs(Sb) NWs are homogeneous since the values for $\langle A \rangle$ and A_{min} are essentially the same with a negligible $\langle \xi \rangle$.

This can be better visualized in Fig. 6.13 which shows the average cross-sectional NW profiles from samples with the InAs layer (solid lines) and without (dashed lines) and the standard deviation (colored bands) in the NW topography extracted from $3\,\mu$m long segments. Where shown, the corresponding HAADF-STEM micrographs confirm that the AFM topography is in good agreement, except for the regions with the $(1\,\bar{1}\,\bar{1})$A facet, which is expected to not be resolved using

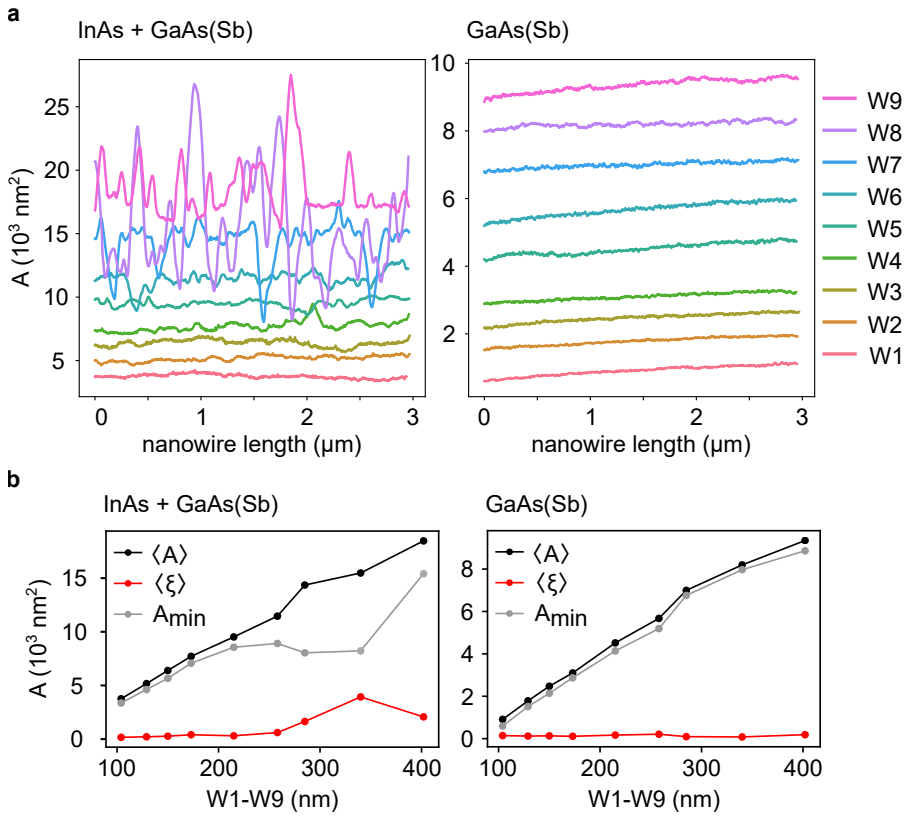

Figure 6.12: **a** left (right) Length dependence of cross-sectional area A of the InAs/GaAs(Sb) (GaAs(Sb)) NWs over 3 μm long segments, for widths $W1$ - $W9$. **b** left (right) Width dependence of the average cross-sectional area ($\langle A \rangle$) of the InAs/GaAs(Sb) (GaAs(Sb)) NWs, the minimum area (A_{min}) and the average of the variation in A ($\langle \xi \rangle$).

AFM due to its almost vertical inclination with respect to the substrate ($\sim 80°$). The NWs with widths $W1$ - $W5$ are bound by $\{1\,1\,1\}$A facets as confirmed by the HAADF-STEM micrographs. NWs with width $W6$ and $W7$ also exhibit similar faceting, in regions that contain a continuous layer of InAs. Upon comparing the evolution of the NW shape with increasing width, the tendency for the InAs layer to accumulate on the longer facet of the underlying GaAs(Sb) layer can be observed. It is illogical to define facets for NWs with width $W8$ since the InAs layer grows very inhomogeneously. However, NWs with width $W9$ show a shift in the nanowire geometry where the InAs forms a continuous layer on the shorter facet of the underlying GaAs(Sb) layer. The InAs NW still exhibits the $\{1\,1\,1\}$A facets, however, it now exhibits an almost symmetric cross-section (both facets have approximately the same length) that is inclined with respect to the substrate zone axis. It is possible that width $W9$ is so wide that the InAs growth on either sides of the underlying GaAs(Sb) facets and proceeds to grow independently due to the influx of adatoms from either side

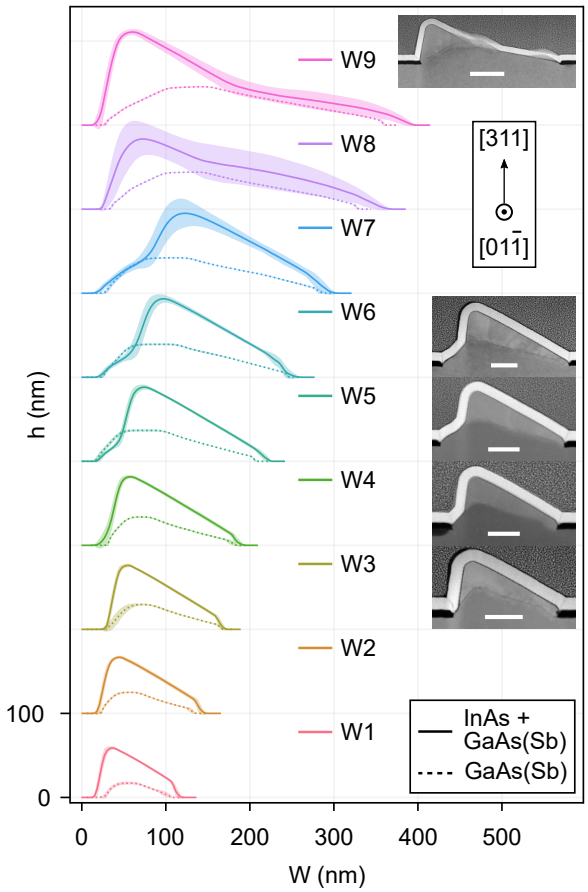

Figure 6.13: Topographical profiles extracted from AFM micrographs for all widths where the solid and dashed lines correspond to the average profiles of InAs/GaAs(Sb) and GaAs(Sb) NWs respectively. The colored bands depict the standard deviation in the NW topography extracted from 3 μm long segments. Cross-sectional TEM micrographs of the NWs are presented for widths $W3 - W6$ (scale bar is 50 nm) and $W9$ (scale bar is 100 nm).

of the NW. The amount of InAs supplied for this sample might not have been enough for NWs with this width to completely cover the underlying buffer layer, but it was enough to form a continuous layer on one side. Thus, individual islands are observed on the flatter facet which do not have a chance to merge due to insufficient material. This might also explain why NWs with widths $W8$ show some regions of a continuous InAs layer on the steep facet and some regions of island growth, implying that this width could be a transition width beyond which adatoms diffusing on top of the steep side of the buffer layer are able to preferentially incorporate into the growing InAs NW, instead of migrating towards the flatter facet. This could ensure that there was enough material for it for form a continuous NW with well-defined facets.

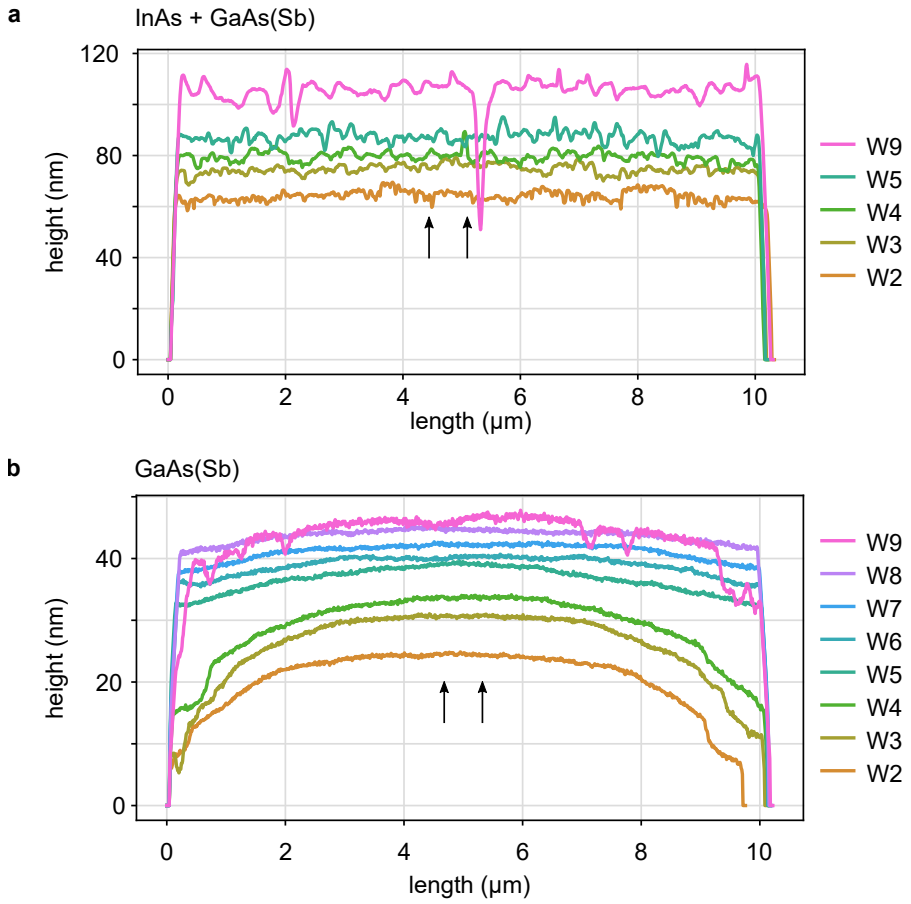

Figure 6.14: **a** (**b**) Height profiles of InAs/GaAs(Sb) (GaAs(Sb)) NWs along a the entire length of 10 μm for different widths. For InAs, only widths *W*2 - *W*5 and *W*9 are showed, whereas *W*2 - *W*9 are showed for the GaAs(Sb) NWs.

Height profile

The NWs used in this study are designed to be 10 μm long. In Fig. 6.14a (b), the NW maximal height extracted using AFM is plotted along the NW length for InAs/GaAs(Sb) (GaAs(Sb)) NWs. The maximal height is considered as a way to minimize contributions from different facets that might be present for different widths, however, these contributions cannot be excluded at the NW ends. Despite this, the GaAs(Sb) NWs show an inhomogeneous height profile, where beyond the 1 - 2 μm long segments towards the middle (highlighted by the black arrows), there is a constant decline in the height profile towards the ends. This can be attributed to an increase in surrounding SiO_2 mask area allowing the Ga adatoms to diffuse onto, rather than incorporating into the growing crystal. This has been observed in GaAs(Sb) NWs grown on GaAs(100) substrates and can be attributed to the decreasing adatom density at the NW ends. This has been modelled and presented in Martin Cachaza's PhD dissertation

[99]. Interestingly, after InAs growth, the NW height profiles show larger variation compared to the homoeptaxially grown GaAs(Sb) on the long range but the gradual decline towards the ends is not observed. This can be explained by the so-called 'sink' effect [22] where In adatoms are observed to have the opposite behaviour compared to Ga adatoms (see Section 2.5). It essentially means that at the growth conditions implemented in this experiment, the effective diffusion of In adatoms from the surrounding SiO_2 mask to the growing crystal is larger than from the crystal to the mask. It is thus possible that the In and Ga composition along the length of the NW is not constant, however, since the structural characterization using AFM and electrical measurements were conducted on 3 μm and 1 μm long segments from approximately the central region of the NWs, only a small difference in the group III incorporation is expected. The NWs considered for electrical characterization consist of 1 μm long segments, and thus the difference in composition along that channel length will be even smaller. It is however not possible to confirm this with EELS. This is because given the NW orientation, the surfaces that are exposed with longitudinal views are of very high order directions, which are not feasible for viewing along for TEM.

Varying in-plane orientation

For NW widths $W3$ - $W9$, the effect of in-plane misorientation with respect to the $[0\bar{1}1]$ direction, $\theta = \pm 4.5°$ with a step size of 0.5° is considered. The resulting topography of the NWs obtained by performing AFM and the top-view images of 1 μm long segments from approximately the middle of the NWs are presented in Fig. 6.15, where H denotes the maximal height of the NWs. As discussed, for NWs with width $W6$ - $W9$, the amount of InAs supplied is not enough to completely cover the underlying GaAs(Sb) layer and this results in increasingly broken segments of InAs on the longer facet. The latter causes an increased variation in the NW cross-section (ξ) along the length.

This average variation in the cross-sectional area of the NWs normalized to the average cross-sectional area ($\langle\xi\rangle_{\text{norm}} = \langle\xi\rangle / \langle A\rangle$) is presented as a function of W and θ in Fig. 6.16a. It should be noted that $\langle\xi\rangle$ was extracted from AFM data of arrays of NWs where the data for NWs with $\theta \neq 0$ was not corrected for the in-plane rotation. This will result in a very small additional variation caused due to the method of extracting ξ. Despite this, it is evident that the wider NWs exhibit a larger variation, both due to increasing W and θ. In order to make a meaningful correlation with transport measurements to the quantify the effect of mis-orientation of on the electrical characteristics of these NWs, longer InAs growth time is required so that there is enough material to form a continuous channel.

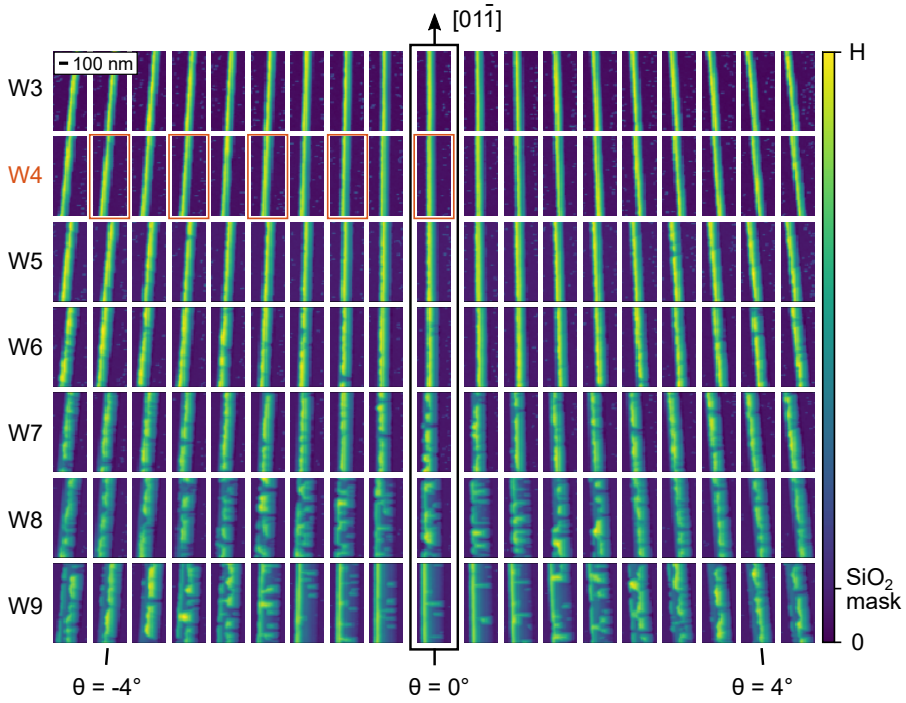

Figure 6.15: Top-view AFM micrographs of NWs with of varying width (*W*3 - *W*9) and varying in-plane orientation ($\theta = \pm 4.5°$) in steps of 0.5°. With increasing width, the amount of InAs is not enough to completely cover the GaAs(Sb) buffer. The close-up view of the NWs highlighted in the red boxes is presented in Fig. 6.16b.

For widths *W*3 - *W*5, the complete layer of InAs also results in increased variation with increasing θ. This can be observed in the close-up 3D AFM topography of NWs with width *W*4 (highlighted in red boxes in Fig. 6.15a) presented in Fig. 6.16b. Segments of the misoriented NWs tend to align with respect to the high-symmetry in-plane $[0\,\bar{1}\,1]$ orientation to maintain the $(1\,1\,1)$A facets, however, under the constraint of the underlying SiO_2 mask, with increasing θ, the segments become shorter due to the highly unfavourable epitaxial growth on an amorphous surface. Following the method adopted in Section 4.2, the effect of $\theta = \pm 4.5°$ on the quality of the NW morphology is quantified using the facet roughness (S_q) of the $(1\,1\,1)$A facet from 1 μm long segments of the NWs. This is presented in Fig. 6.16c, where S_q is minimized for $\theta = 0$ and increases with increasing θ. Thus, to minimize surface roughness, it is very important to align the NWs along the high-symmetry orientations. The effects of disorder in surface morphology on electrical transport is presented in the following Chapter 7 by conducting electrical transport experiments at cryogenic temperatures on NW based field effect transistor (NWFET) devices.

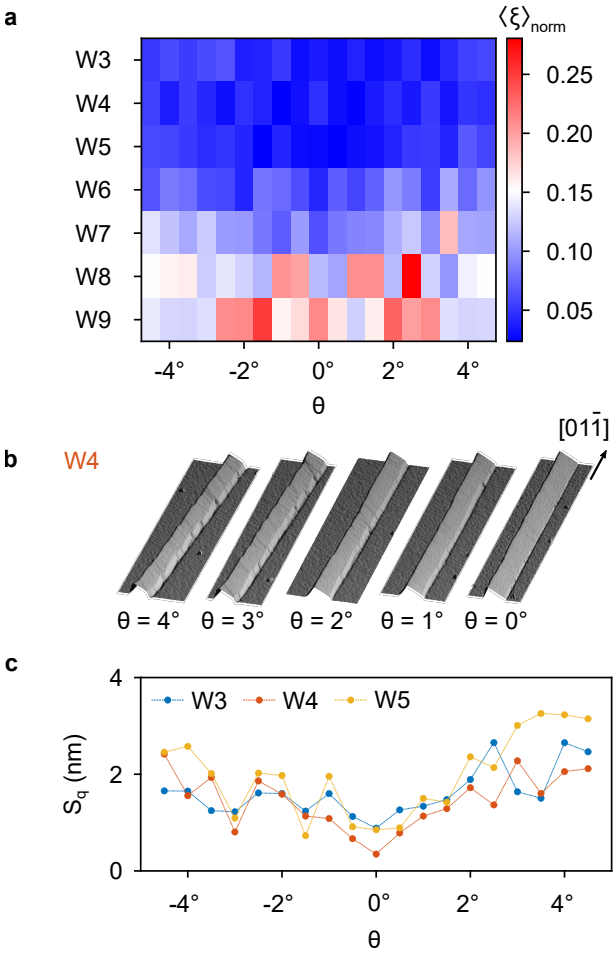

Figure 6.16: **a** Average variation in the cross-sectional area of the NWs normalized to the average cross-sectional area ($\langle\xi\rangle_{\text{norm}} = \langle\xi\rangle / \langle A\rangle$) for NWs with *W*3 - *W*9 and $\theta = \pm 4.5°$. **b** 3D AFM topography of NWs with width *W*4 showing steps along the NW facets for $\theta \neq 0$. **c** Facet roughness (S_q) along the $(1\,1\,\bar{1})$A facet of the NWs with width *W*3, *W*4 and *W*5 for $\theta = \pm 4.5°$, highlighting the effect of in-plane misalignment despite forming a complete InAs layer on top of the underlying GaAs(Sb) buffer.

6.4.2 *Composition and strain relaxation*

In this section, the InAs/GaAs interface is investigated for distribution of In and Ga composition within the NWs, along with the presence of crystal defects owing to the large lattice mismatch of $\sim 7.7\%$ between the two materials.

Chemical composition using EELS

Electron Energy Loss Spectroscopy (EELS) of the NWs presented in Fig. 6.17a for widths *W*3 - *W*6 and *W*9 is used to obtain the corresponding elemental composition. This is presented with respect

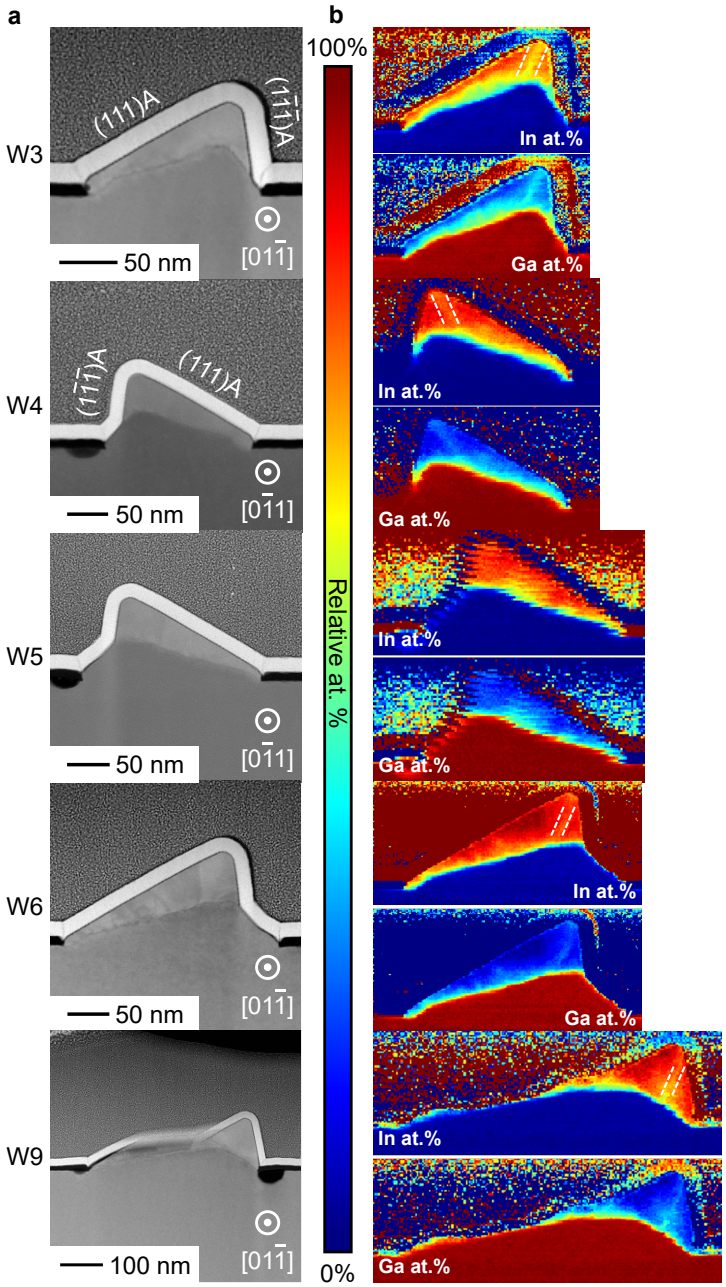

Figure 6.17: **a** HAADF-STEM micrographs of NWs with widths *W*3 - *W*6 and *W*9. **b** Corresponding In (top) and b Ga (bottom) relative atomic % compositional maps of NWs obtained by electron energy loss spectroscopy (EELS). The InAs region is found to be diluted with Ga. The white dashed lines show Ga-rich regions in the InAs channel.

to the In and Ga relative atomic % in Fig. 6.17b (top) and (bottom) respectively. There are some Ga traces within the InAs region of the NWs observed in the relative quantification maps, where a gradual change of composition from the GaAs(Sb) buffer to the edge of the

NW is observed. It can be seen that the In concentration is highest towards the edge of the NW for all widths presented.

For width *W*3, the measured In content at the outer edge of the NW is found to be 80 % and is the lowest compared to the all other widths. Widths *W*4 and *W*5 show a Ga diffusion of $\sim$ 8 - 10 % towards the outermost InAs region. For width *W*6, it is observed that the relative In atomic % reaches a saturation of 99 % in some parts of the NW close to the edge towards the longer $(1\,1\,1)$A facet. This is coincident with pure InAs taking into account the associated errors in the acquisition process. However, even with the higher concentration of In attained in these NWs, there is still some Ga diffusion towards the NW, which follows a gradual decrease from the GaAs(Sb) buffer to the large InAs top facet, as seen by a gradual color change at the InAs/GaAs(Sb) interface.

The NW with width *W*9 also shows some gradual Ga diffusion towards the longer GaAs(Sb) facet. However, in this case, the transition to InAs within the central region of the NW is more abrupt than in the other widths. The In vs. Ga ratio towards the $(1\,1\,1)$ facet reaches the maximum of the whole heterostructure, with a 95 % In vs 5 % Ga. For all widths presented here, a preferential diffusion of Ga is observed along the $[0\,0\,1]$ direction, identified from the Ga-rich regions highlighted in Fig. 6.17b (top) with white dashed lines. Such preferential diffusion has been reported in GaAs(Sb)/InGaAs/InAs NWs grown on GaAs$(0\,0\,1)$ substrates and is associated with a difference in the mobility of In and Ga species [21].

Overall diffusion from the underlying GaAs(Sb) buffer layer towards the InAs channel is probably caused by the high strain which builds up at the interface. Thus, it has been proposed that Ga diffusion arises as a strain minimization mechanism during growth of lattice-mismatched InAs and GaAs. The strain mechanism is discussed below.

Strain relaxation

Figure 6.18a shows the cross-sectional HAADF-STEM micrographs of NWs with width *W*3 - *W*6 and *W*9, along with the corresponding dilatation maps with respect to the $(1\,\bar{1}\,\bar{1})$ and $(1\,1\,1)$ planes presented in Fig. 6.18b. It should be noted that the zone axes for *W*3 and *W*6 and *W*9 are mirrored compared to the remaining images. The NWs for the widths presented here are bound by $\{1\,1\,1\}$A facets, as expected from the AFM analysis. For all widths, an array of misfit dislocations all along the InAs-GaAs(Sb) interface can be observed in the D$(1\,\bar{1}\,\bar{1})$ map, highlighted by black arrows only in the top row to preserve visibility of the maps. From the maps, it can be seen that the strain relaxation happens abruptly at the interface, highlighted by the sudden change in color going form the GaAs(Sb) buffer to the InAs region. In structures where ternary buffers are introduced in between the GaAs buffer

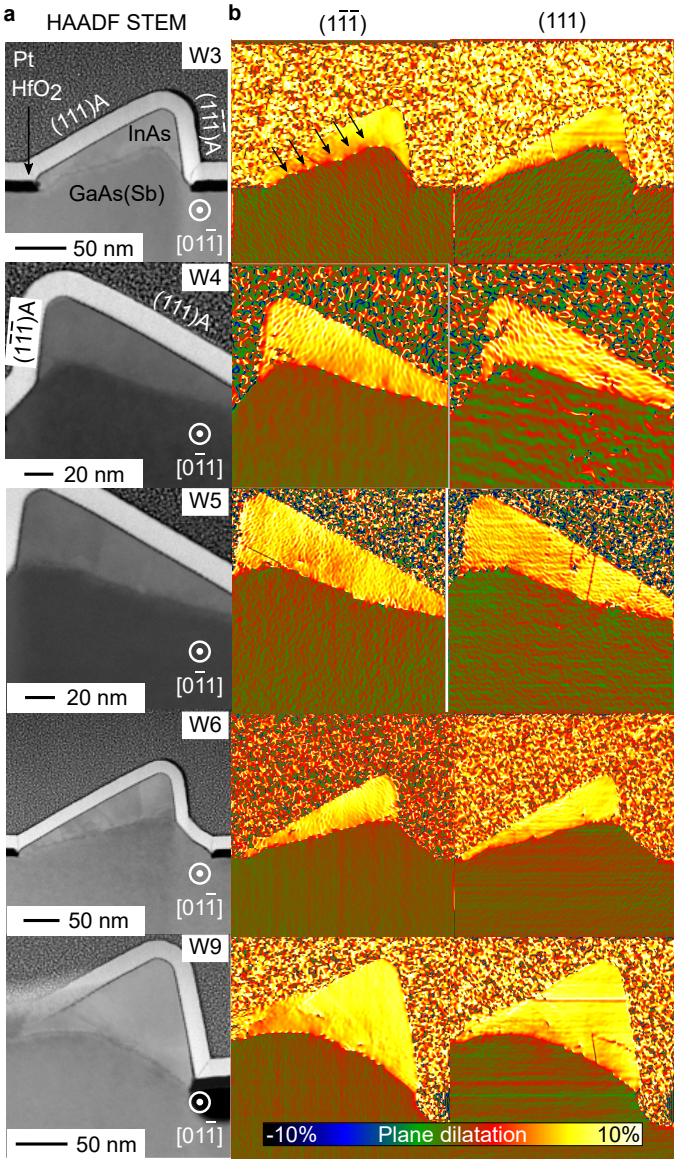

Figure 6.18: **a** High-angle annular dark field scanning transmission (HAADF-STEM) micrographs show a cross-sectional view of the GaAs(Sb) and InAs regions of the NWs roughly from the middle of an array of 50 NWs oriented along the $[0\bar{1}1]$ direction on a GaAs$(3\,1\,1)$A substrate, for widths *W*3 - *W*6 and *W*9. The morphology of all NWs shows that the InAs channel exhibits $\{1\,1\,1\}$A facets. **b** Dilatation maps of all NWs show an array of dislocations at the GaAs(Sb)/InAs interface. Scale bars are consistent in **a** and **b**.

and the InAs channel [21], the strain relaxation is observed to be much more gradual. Here, the interface exhibits an array of misfit dislocations visible via the discontinuity in color at the interface for all widths.

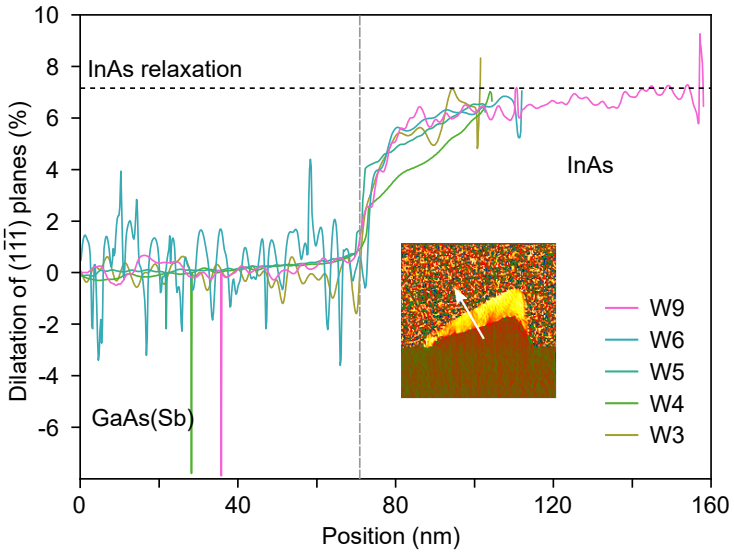

Figure 6.19: Dilatation of the $(1\bar{1}\bar{1})$ planes for widths *W*3, *W*4, *W*5, *W*6, *W*9 which shows that all NWs except *W*9 only reach the InAs lattice parameter for the outermost layers of the NW (white arrow in the inset represents the directions along with the profile was extracted for all widths). For *W*9, there exists a larger region for which the lattice constant approaches the relaxed value.

Relative dilatation is extracted for NWs with widths *W*3, *W*4, *W*5, *W*6, *W*9. Figure 6.19 compares the dilatation %. For *W*3, the values of dilatation get close to relaxation i.e., get close to 7.7% (though slightly under it) just at the very top of the NW, but this value is reached gradually across the interface over a distance of $\sim$ 30 nm. The same applies for widths *W*4, *W*5 and *W*6. However, for *W*9 the InAs, the lattice constant approaches the relaxed value of 7% for large region, unlike for NWs with smaller widths. The relaxation happens a little more abruptly over a distance of $\sim$ 10 nm. EELS maps displayed earlier (see Fig. 6.17) reveal that there exists some Ga diffusion to the InAs region, which explains the gradual increase in dilatation. Thus the In content is not exactly 100% at the outermost regions, meaning the relaxed InAs value will not be achieved and the NWs are rather InGaAs very rich in In content, even if it is relaxed.

To understand if the strain is fully relaxed via formation of misfit dislocations, rotational maps are also plotted in Fig. 6.20. For all widths presented here, the following observations are common: the $\{1\,1\,1\}$A planes show a splitting visible as a color change, indicating the presence of an asymmetric in-plane rotation at the NW edges. The rotation is stronger ($\sim 3°$) on the shorter $\{1\,1\,1\}$A planes covering the more inclined regions of the GaAs(Sb) buffer than on the other side that sits atop the longer facet. Rotation on the side covering the large GaAs(Sb) facet shows a strong difference between widths *W*3 - *W*6 going from $\sim 0.65°$ to $\sim 2°$ for *W*9. Even though the plane splitting exist

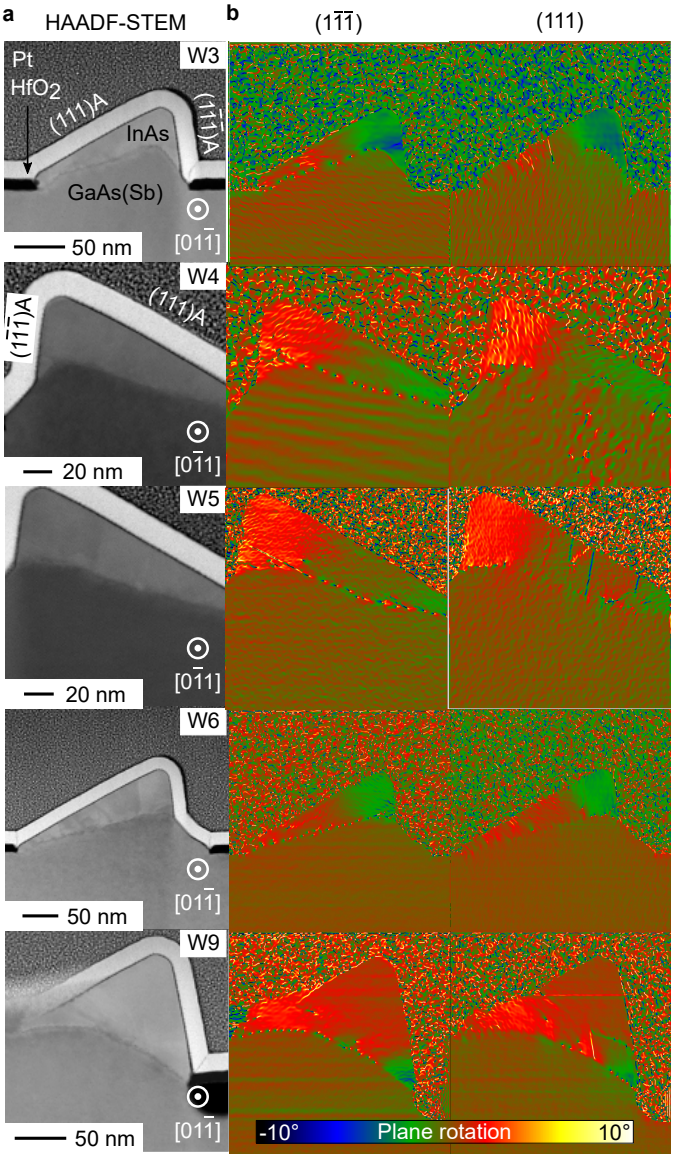

Figure 6.20: a High-angle annular dark field scanning tunneling (HAADF-STEM) micrographs show a cross-sectional view of the GaAs(Sb) and InAs regions of the NWs roughly from the middle of an array of 50 NWs oriented along the $[0\bar{1}1]$ direction on a GaAs$(3\,1\,1)$A substrate, for widths *W*3 - *W*6 and *W*9. **b** The rotational maps indicate asymmetric rotation of the $\{1\,1\,1\}$A crystal planes between the GaAs(Sb) buffer and the InAs channel. Scale bars are consistent in **a** and **b**.

for width *W*9, interestingly, the region with towards the steep facet (in green) is much smaller. This could align with the hypothesis that for this large width, the continuous InAs channel grows independently on one side of the underlying buffer, resulting in more homogeneous plane rotation. Therefore, the morphology of the heterostructure likely has a strong influence on the plane rotation relaxation mechanism.

The relaxation mechanism involves the formation of an array of misfit dislocations (plastic relaxation) and asymmetric elastic plane rotation the NWs.

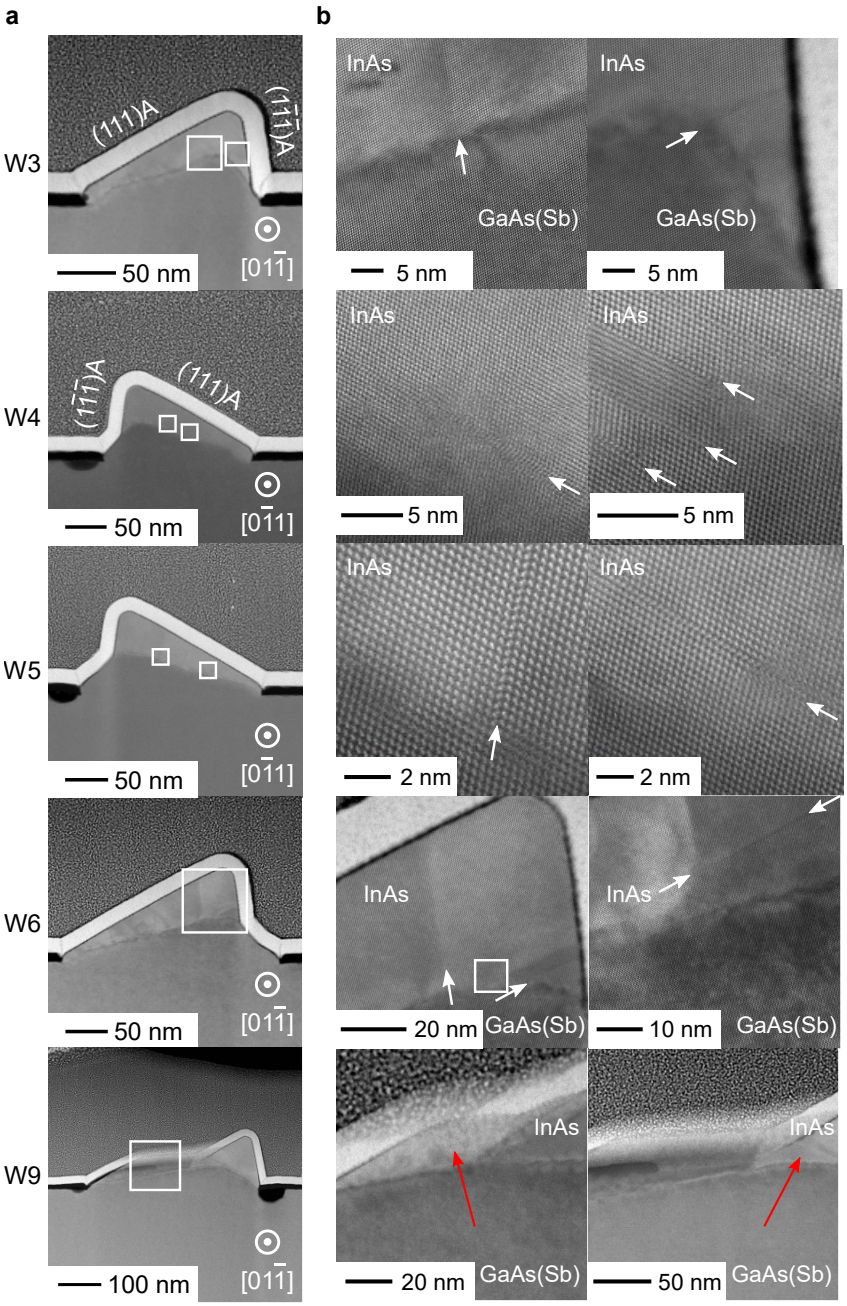

Figure 6.21: **a** High resolution HAADF-STEM micrographs of NWs with widths *W*3 - *W*6 and *W*9. **b** Zoomed-in regions indicated by the white boxes, white arrows indicate the stacking faults, which always occurs parallel to either of the {1 1 1}A facets. Red arrows highlight the multiple nucleation sites for the case of *W*9.

Another way of strain relaxation, in addition to misfit dislocations at the InAs/GaAs(Sb) interface, are stacking faults. Figure 6.21

shows high resolution HAADF-STEM micrographs of select NWs with widths $W3$ - $W6$ and $W9$. The stacking faults are highlighted with white arrows, and are always seen to occur parallel to either of the $\{1\,1\,1\}$A facets. They could indicate the the interface of multiple different islands that merge together. Additionally, for $W9$, the micrographs also show the occurrence of multiple nucleation sites (highlighted by red arrows) originating from the short and long GaAs(Sb) facets confirming that for this dimension, InAs growth starts independently on either facets of the underlying buffer. Stacking faults emerging in almost all the NWs observed here, is an indication of non-optimized growth parameters. InAs-GaAs is highly lattice mismatched and the resulting heterostructure growth is possible only at the cost of lowering the crystal quality. Introducing ternary buffers, changing the InAs growth time to deposit less material to reduce strain in the system might a possible solution, but requires a careful design of the SAG substrate.

6.5 Conclusions

A systematic study of the structural characteristics of InAs/GaAs(Sb) SAG NWs grown on GaAs$(3\,1\,1)$A substrates, primarily using AFM, has been presented. The relevant parameters such as NW height (H), facet length (F), cross-sectional area (A) have been extracted from the AFM data and are used to represent the quality of the NW morphology. They have been presented along with a statistical significance for 180 NWs (of a fixed width) spread across a 512×18 array and show that H has a variability of 1.55% and F has a variability of 2.56%. Next, the effect of varying SAG mask dimensions such as width (W) allows to map a temporal study of the InAs growth from a single sample. It is found that for the growth conditions implemented here, NWs with $W = 100 - 220\,\text{nm}$ result in the formation of a continuous layer of InAs, bound by $\{1\,1\,1\}$A type facets, almost covering the entirety of the underlying GaAs(S) buffer layer. Increasing W has a detrimental effect of the NW facet roughness (S_q) due to increasing discontinuities in the InAs layer. However, a further increase to $W = 400\,\text{nm}$ leads to the formation of a continuous InAs channel primarily on one side of the underlying GaAs(Sb) buffer layer, bound by the same facets but exhibits a symmetric cross-section. The effect of in-plane mis-orientation with respect to the high-symmetry in-plane direction on the NW morphology for different W has also been quantified in terms of facet roughness S_q. It is found that S_q increases with increasing mis-orientation for all W but increases even more for larger W due to the insufficient amount of InAs. The AFM data for NWs with different W has also been supplemented with relevant crystal structure, strain and composition analysis and gives insight into the quality of the

InAs/GaAs interface and the crystal quality of the InAs channel. It is found that the NWs with width *W9* have show the highest In content and approach the InAs lattice constant more abruptly than for other NWs. The large scale structural characterization confirms the feasibility of using SAG as a scalable, reproducible platform for NW based circuits. The study of the effect of varying SAG mask dimensions on the NW morphology and crystal structure allows us to determine the optimal dimensions to obtain high quality NWs. The importance of the study of NW morphology to understand the corresponding electronic transport behaviour will be seen in the following Chapter 7.

7

Electrical Characteristics

The results presented in this chapter partially overlap with manuscripts [3] and [4], respectively:

Cryogenic multiplexing with bottom-up nanowires
D Olsteins, G Nagda, D J Carrad, D Beznasyuk, C E N Petersen, S M-Sánchez, J Arbiol, T S Jespersen
In review

Dimension dependent electrical transport in planar InAs nanowires
G Nagda, D Olsteins, S M-Sánchez, D Beznasyuk, D J Carrad, J Nygård, J Arbiol, T S Jespersen
In preparation

The device fabrication and electrical transport measurements were carried out by **Dags Olsteins** affiliated with the Center for Quantum Devices, Niels Bohr Institute, University of Copenhagen, 2100 Copenhagen, Denmark. The subsequent data analysis was performed in collaboration with **Dags Olsteins** and **Damon Carrad**, affiliated with the Department of Energy Conversion and Storage, Technical University of Denmark (DTU), 2800 Kgs. Lyngby, Denmark.

7.1 Introduction

InAs (and InSb [100]) NW-based FETs are promising candidates for ultra-low-power electronics and quantum information processing applications due to their high carrier mobility when compared to NWs based on other materials [101–104] and intrinsic confinement [105] making it particularly attractive for use in cryogenic electronics. Continued efforts are being made to improve the quality of InAs NWs in this regard [106–108]. The development of large scale integrated (LSI) circuits incorporating many interacting such devices requires potential materials to exhibit high-precision reproducibility and scalability. However, large scale characterization of electronic transport properties has not been as feasible as optical techniques such as μ-photoluminescence [109]. To demonstrate that the NWs developed in this study are a promising platform for quantum electronics due to the possibility of controlled growth of large-scale arrays, the first demonstration of LSI circuits based on InAs SAG has been made.

A multiplexer-demultiplexer (MUX/d-MUX) set-up is realized for a statistical characterization of nanowire field effect transistor (NWFET) devices. Electrical characteristics such as the threshold voltage (V_{TH}) and field effect mobility (μ_{FE})of 256 nominally identical NWFET devices are quantified with a statistical significance. The correlation between these parameters after performing a thermal cycle is also analyzed to understand the significance of contributions from structural variability to the device performance. Further, the dependence of electrical transport characteristics on the NW dimensions such as width (W) and in-plane orientation (θ) in terms of structure and morphology is discussed and a correlation with the structural characteristics demonstrated in Chapter 6 has been found. Briefly, the results from a large array of nominally identical SAG NW quantum dot devices which show that multiple NWs can be simultaneously tuned to Coulomb blockade using only a small number of shared gates, have been presented.

7.2 Field effect transistors

A field-effect transistor (FET) is an electronic device that controls the flow of current through the semiconductor channel by varying the voltage applied to a gate electrode. The basic structure of an InAs NW-based FET consists of a single InAs NW with source and drain electrodes at either end and a gate electrode placed on top of the NW (see inset in Fig. 7.2a). The source and drain electrodes are typically made of a metal such as gold, while the gate electrode is separated from the semiconducting channel with an insulator. When a voltage is applied between the source and drain electrodes (V_{SD}), electrons flow through the InAs NW channel. The gate voltage (V_{G}) applied to

the gate electrode modulates the electron density in the channel and hence the current (I_{SD}) flowing through the channel.

At cryogenic temperatures, the carrier mobility in InAs NWs is enhanced due to reduced phonon scattering. This results in a higher transconductance (G), which is the rate of change of drain current (I_{SD}) with respect to gate voltage (V_G). The reduced background carrier density at cryogenic temperatures also leads to a lower gate capacitance, which enhances the gate control over the channel. In addition to enhanced carrier mobility and gate control, InAs NW-based FETs operating at cryogenic temperatures can also exhibit unique transport properties due to the formation of one-dimensional subbands in the NW channel. These subbands arise due to quantum confinement of electrons in the radial direction of the NW. The number and energy spacing of these subbands can be controlled by varying the diameter of the NW.

Thus InAs NW-based FETs operating at cryogenic temperatures offer several advantages over conventional FETs, including enhanced carrier mobility, gate control, and unique transport properties due to quantum confinement. These devices have great potential for use in ultra-low-power electronics and quantum information processing applications.

7.3 Multiplexers for large-scale characterization

The MUX/d-MUX circuit is based on InAs SAG NWs grown in a 512×16 array. The NW dimensions correspond the width $W4$ (see Section 6.3), with an inter-wire distance $P = 2\,\mu$m and a channel length $L = 1\,\mu$m. It is built on a hierarchical MUX structure depicted in Fig. 7.1, composed of devices on different rows of the array, with two gate electrodes spanning the entirety of each row. The gated segment positions alternate between a functional and a screened gate (described later in Fig. 7.2). Addition of each level (in this case a level corresponds to a row in the array) in the MUX circuit doubles the number of outputs for the level below, requiring $2n$ gates for operation for the n^{th} level. Thus an 8-level MUX circuit connected to a corresponding 8-level d-MUX incorporates 8192 individual SAG NWs, allowing for the individual addressing of 512 devices under test (DUT) using 37 control lines, demonstrating the vast scalability of this set-up.

Before probing the performance of varying NWs with different properties, it is imperative to check for the reproducibility important metrics that defines an FET device, the transconductance (G) response and the threshold voltage (V_{TH}) [110]. For demonstrating this, the conductance response of devices comprising of increasing number of NWs connected in parallel was measured. The SEM in Fig. 7.2a inset shows a typical device consisting 4 NWs connected in parallel by Ti/Au source/drain ohmic contacts to control V_{SD}, and a $1\,\mu$m long

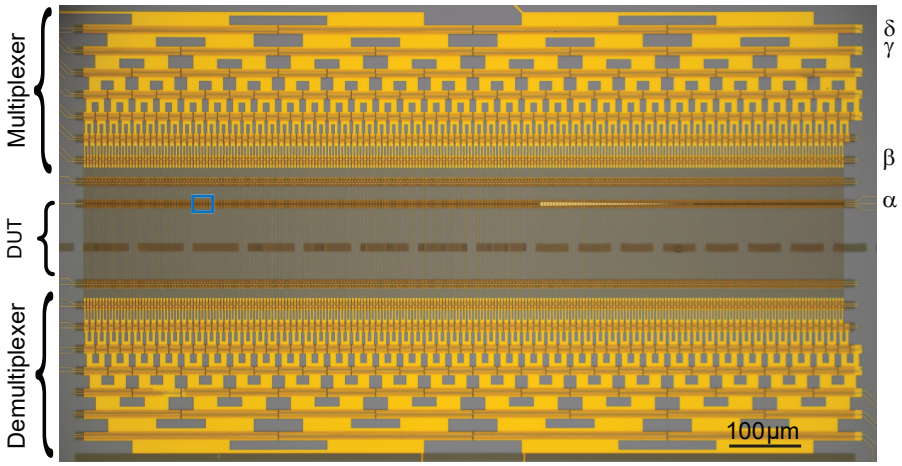

Figure 7.1: An optical microscope image of a multiplexer-demultiplexer (MUX/d-MUX) circuit set-up based on InAs SAG NWs grown in a 512×16 arrays. The circuit includes devices under test (DUTs) indicated as α. The DUT level shows connections to 500 lines, and the number of DUTs was doubled from 256 (2^8 in the row above) by using two source/drain pairs. Device fabrication and optical image credit: ***Dags Olsteins***.

gated segment operated by V_G. The device uses two gates: one controlling the G of the exposed InAs NWs (blue), and another screened by the Ti/Au metallic contact with no effect on the NW (grey). G is measured at a base temperature of $T = 20\,\text{mK}$ for 5 devices with varying numbers of NWs (M = 1, 4, 16, 32, 64) and plotted against gate voltage (VG), with a common fit to the relation $G = KM(V_G - V_{TH})$ where K is a fitting parameter. The devices act as normally-on, n-type FETs with identical VTH. Under the fair assumption that the devices operate in a linear regime, G is found to be proportional to M as expected for nominally identical NWs. The fit failure for $M = 64$ may be due to a high sensitivity to the estimate of series resistance R_S when the device resistance is low, details of which can be found in publication [3] [111]. The reproducible V_{TH} thus enables the use of large-M SAG NWFETs as building blocks of LSI circuits.

7.4 Reproducibility

The characteristics of NW FETs are dependent on their structure, and therefore the distribution of transport parameters reflects the structural variability discussed in Section 6.3. In order to assess the amount of variation in the transport properties and the degree of reproducibility,

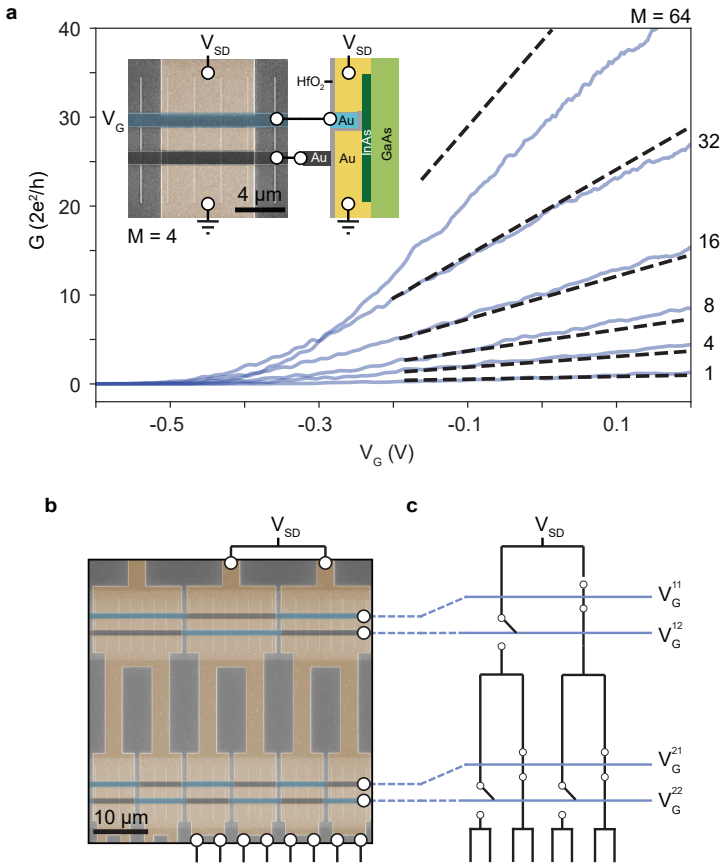

Figure 7.2: **a** Conductance (G) as function of gate voltage V_G for NWFETs based on M = 1, 4, 16, 32, 64 SAG NWs in connected in parallel, with corresponding linear fit indicated by dashed lines. Inset shows an SEM micrograph of a NWFET $M = 4$, where Ti/Au Ohmic contacts are indicated in gold, and the Ti/Au gate in blue. The gate in dark gray is screened by the underlying ohmic contact as illustrated by the adjacent schematic of a cross-sectional view of the device. **b** An SEM micrograph of NWFETs arranged in an MUX circuit. Gates are screened in alternating elements as indicated by the blue/gray. **c** A schematic representation of the circuit in b, indicating the device operation using 2 alternating functional gate electrodes. Device fabrication, figure and data credit: ***Dags Olsteins***.

the MUX/d-MUX set-up was employed for individual characterization of 256 nominally identical NWFETs. The transfer characteristics of the devices were measured at $T = 20\,\text{mK}$, then repeated after warming to $T = 100\,\text{K}$, and finally again at $T = 20\,\text{mK}$ after a thermal cycle to room temperature. The measurements were conducted in both V_G sweep directions, resulting in a total of 1536 traces that were acquired and analyzed. Figure 7.3 displays a representative selection of these traces. Consistent with the behavior shown in Fig. 7.2b, normally-on n-

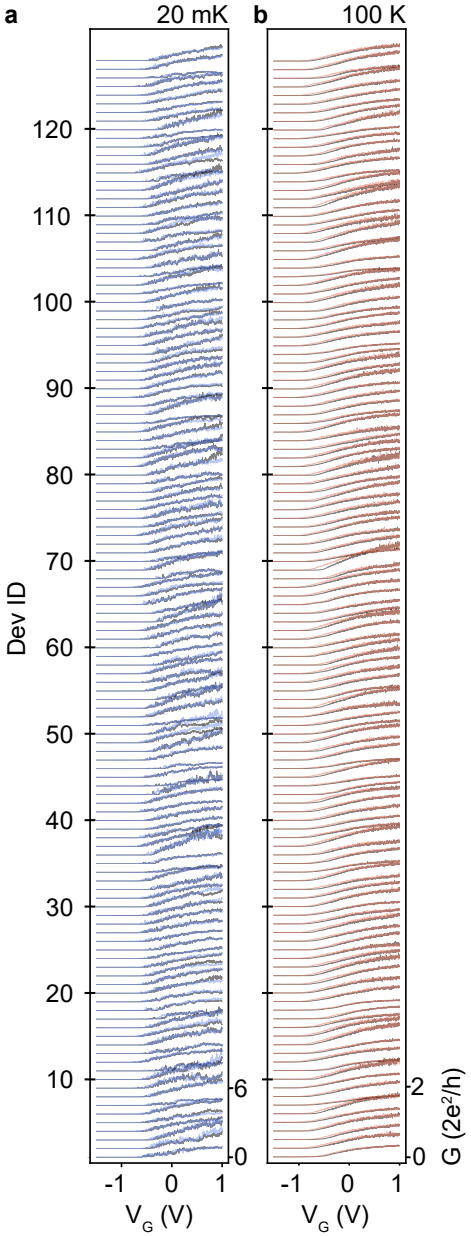

Figure 7.3: a Pinch-off curves of 128 NWFET devices offset in G for clarity. V_G is swept from positive to negative (black) and from negative to positive (blue/red) taken at $T = 20\,\text{mK}$ (blue) and $T = 100\,\text{K}$ (red). Series resistance (R_s) is estimated from the fit and subtracted. Figure and data credit: ***Dags Olsteins***.

type FET transport characteristics are observed for all NWFET devices. By fitting the measured data to the expression [100]

$$G(V_G) = \left(R_s + \frac{L^2/}{\mu_{FE}\ C\ (V_G - V_{TH})} \right) \tag{7.1}$$

field effect mobility, μ_{FE}, threshold voltage, V_{TH}, and series resistance, R_s, which accounts for circuit and contact resistances are extracted. An estimate for the gate capacitance $C = 5.3\,fF$ based on numerical simulations and the automatic fitting procedure developed to deal with the very large datasets is beyond the scope of this thesis and is discussed in detail in publication [3] [111].

Apart from the contributions from structural variations, the characteristics of NW FETs also depend on processes such as electron scattering and screening from charged impurities, which are in turn a result of processing and experimental conditions. Comparing measurements before and after thermal cycling can thus provide insight into the effects of charged impurities and structural variations. The corresponding distributions of electron mobility μ_{FE}, V_{TH}, and ΔV_{TH} at $T = 20\,mK$ and $T = 100\,K$ are presented in Fig. 7.4a-c. $\Delta V_{TH} = V_{TH}^{dwn} - V_{TH}^{up}$ for positive (up) or negative (dwn) V_G sweep directions is used as a measure of hysteresis. The average V_{TH} is $\approx -570\,mV$ at $T = 20\,mK$, and decreases to $\approx -900\,mV$ at $T = 100\,K$ due to a decrease in charge trap lifetime [112]. In Fig. 7.4b, the corresponding ΔV_{TH} shows an increase at $T = 100\,K$. At higher temperatures, the thermal energy of the impurities is increased, allowing them to move more freely and rearrange themselves more readily in response to the applied electric field. This rearrangement of charged impurities near the NW channel is possibly leads to a larger hysteresis effect in the device characteristics. Next, Fig. 7.4c presents μ_{FE} since it is a crucial parameter that characterizes the efficiency of the device, as it determines how fast electrons can move in response to an applied electric field. Higher μ_{FE} translates to faster device switching, which is important for high-performance electronics. Mobility can also indicate the level of disorder in a system, as electron scattering [113] due to defects, impurities, and phonons can hinder it. The average μ_{FE} is found to be approximately $125\,cm^2/V\,s$ at $T = 20\,mK$. This is particularly low when compared to other research based on InAs SAG NWs [19, 106], and the reason can be attributed to the crystal quality of the InAs channel. As seen in Chapter 6, there exist a lot of misfit dislocations, stacking faults in addition to a high elastic strain in the InAs channel. The mobility further reduces to 45 $cm^2/V\,s$ when the temperature is increased to $T = 100\,K$. This can be attributed to the thermal activation of charged surface scattering [114] and an increased phonon scattering [115].

Figure 7.5 shows correlation between these parameters before and after thermal cycling. This is done by calculating the Pearson's correlation coefficient ρ as a measure of the strength and direction of the linear relationship between the parameters at both temperatures, along with the corresponding p-value as a measure of the statistical significance of the observed ρ. The values for V_{TH} at $T = 20\,mK$ and $T = 100\,K$ in Fig. 7.5a-d show a significant correlation, indicating contributions from the structural variations across the SAG array. A

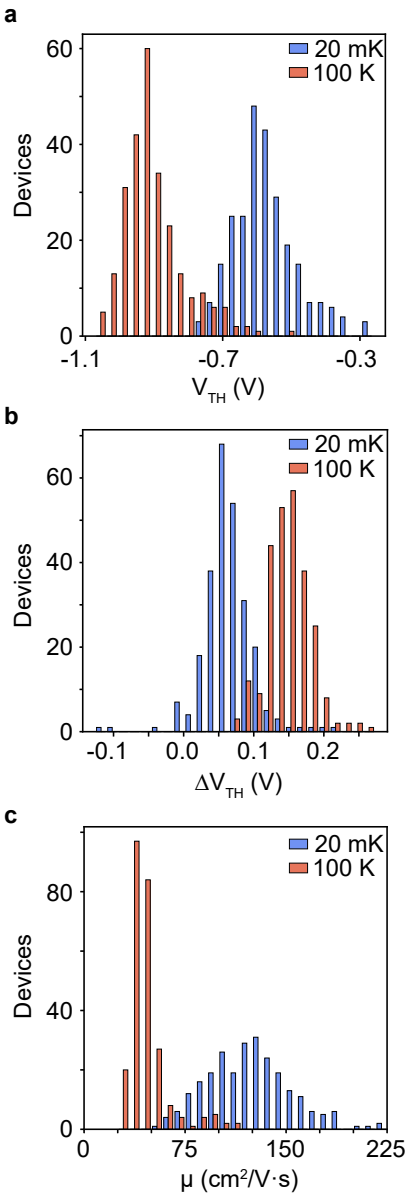

Figure 7.4: Histograms of **a** V_{TH}: $\langle V_{\mathrm{TH}}^{20\,\mathrm{mK}} \rangle = -572\,\mathrm{mV}$, $\sigma_{V_{\mathrm{TH}}}^{20\,\mathrm{mK}} = 91\,\mathrm{mV}$; $\langle V_{\mathrm{TH}}^{100\,\mathrm{K}} \rangle = -905\,\mathrm{mV}$, $\sigma_{V_{\mathrm{TH}}}^{100\,\mathrm{K}} = 87\,\mathrm{mV}$, **b** ΔV_{TH}: $\langle \Delta V_{\mathrm{TH}}^{20\,\mathrm{mK}} \rangle = 64\,\mathrm{mV}$, $\sigma_{\Delta V_{\mathrm{TH}}}^{20\,\mathrm{mK}} = 37\,\mathrm{mV}$; $\langle \Delta V_{\mathrm{TH}}^{100\,\mathrm{K}} \rangle = 148\,\mathrm{mV}$, $\sigma_{\Delta V_{\mathrm{TH}}}^{100\,\mathrm{K}} = 31\,\mathrm{mV}$, **c** μ_{FE}: $\langle \mu_{\mathrm{FE}}^{20\,\mathrm{mK}} \rangle = 127\,\mathrm{cm}^2/\mathrm{V}\cdot\mathrm{s}$, $\sigma_{\mu_{\mathrm{FE}}}^{20\,\mathrm{mK}} = 40\,\mathrm{cm}^2/\mathrm{V}\cdot\mathrm{s}$; $\langle \mu_{\mathrm{FE}}^{100\,\mathrm{K}} \rangle = 46\,\mathrm{cm}^2/\mathrm{V}\cdot\mathrm{s}$, $\sigma_{\mu_{\mathrm{FE}}}^{100\,\mathrm{K}} = 15\,\mathrm{cm}^2/\mathrm{V}\cdot\mathrm{s}$, representing 256 devices measured at 20 mK (blue) and 100 K (red).

significant dispersion across two cooldowns to $T = 20\,\mathrm{mK}$ also indicates that charged impurities must contribute to the variability in V_{TH}. Figure 7.5b-e shows that the hysteresis (ΔV_{TH}) values at both temperatures and between cooldowns are uncorrelated. It suggests that the hysteresis is likely due to external factors such as nearby charge

impurities rather than internal device specific properties such as NW structural variations. Finally, considering the positive correlations for μ_{FE} in Fig. 7.5c-f indicate that both structural variation and charge impurities contribute significantly to the performance of the NWFET devices.

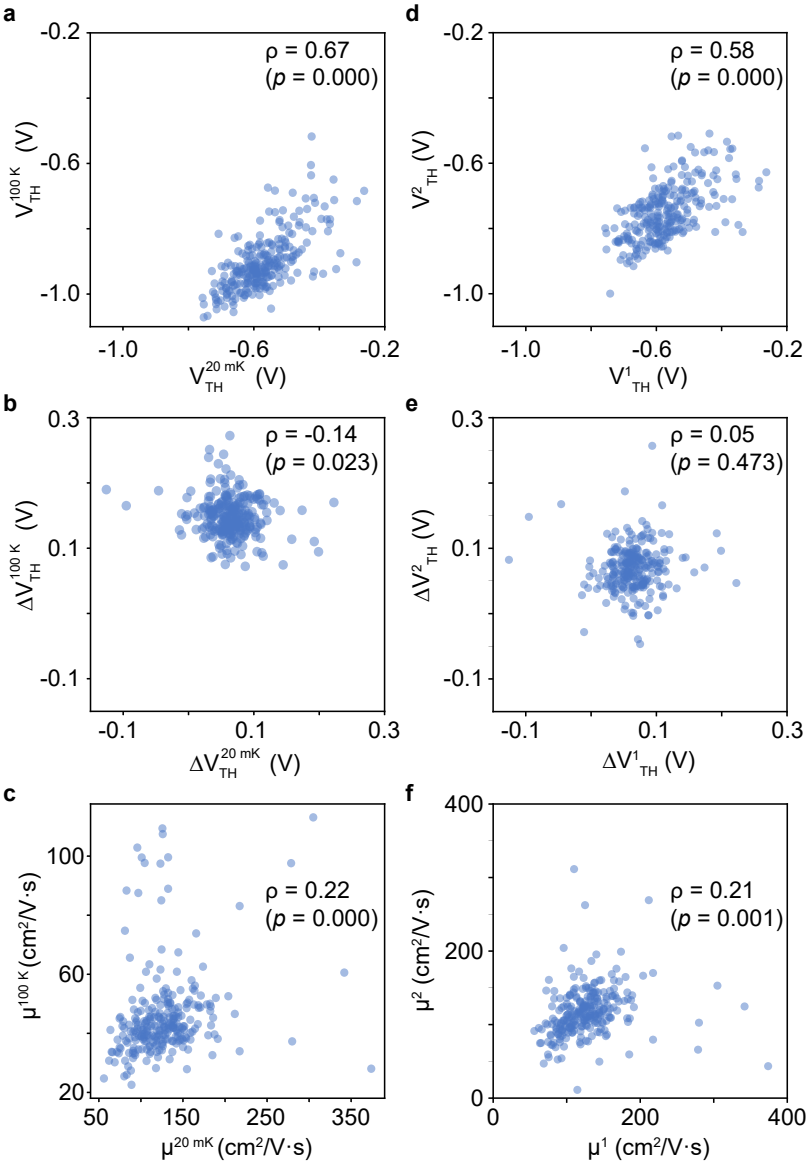

Figure 7.5: a, b, c Correlations between parameters at 20 mK and 100 K V_{TH}, ΔV_{TH}, and μ_{FE} respectively. Pearson's correlation coefficient ρ and the corresponding p-value shown in each panel. **d, e, f** Correlations between two cooldowns to 20 mK for V_{TH}, ΔV_{TH}, and μ_{FE} respectively. Figure and data credit: ***Dags Olsteins***.

7.5 Dimension dependent electrical transport

Using the MUX/d-MUX set-up, it has now been possible to conduct transport measurements of various NWs and map the transport characteristics of different NW dimensions. The structural characteristics of the InAs/GaAs(Sb) NWs as described in Chapter 6 show that simply varying the NW width W results is significant variations in the shape and crystal structure of the InAs channel. Thus, NWFET devices are fabricated and transport characteristics are measured to understand the influence of a few select parameters.

Figure 7.6a shows an SEM micrograph of the devices fabricated based on NWs with varying widths using the MUX/d-MUX set-up. The NW arrays share a single gate electrode that controls V_G over the same channel length of $L = 1\,\mu$m, and V_{SD} is controlled individually by MUX outputs. Transport measurements were performed on several nominally identical NWFET devices based on widths $W3$, $W6$ and $W9$, and the circuits from the red rectangle are depicted in Fig.7.6b. The circuit of the DUTs consists of not only the NW under investigation, but also NWs in series from the MUX/d-MUX above and below. Adjacent to the DUT, we place a shorted line to measure the series resistance of the MUX/d-MUX circuit. This enables us to estimate circuit series resistance R_s.

In Fig. 7.7a-c, the $G(V_G)$ of $[0\,\bar{1}\,1]$ oriented NWFETs with widths $W3$, $W6$ and $W9$ are presented. Width $W4$ which corresponds to the NW dimensions of the MUX itself, are all functional. For width $W6$, four devices are non-functional (red arrows in Fig. 7.7b), but for $W9$, all devices are functional. This is correlated with the NW morphology showing a continuous InAs channel for $W3$ and $W9$ but not for $W6$ (see Section6.4.1). All functional devices consistently show normally-on n-type behaviour. The dependence of V_{TH} on the NW width are discussed further below.

Also, from Section 4.3, it is known that a typical mis-orientation related to fabrication tolerances of the SAG substrate is of the order of $\theta = 0.5°$. Thus, the FETs based on NWs with widths $W3$ - $W8$ mis-oriented with respect to the $[0\,\bar{1}\,1]$ direction, $\theta = \pm 4.5°$ were measured using the circuit shown in Fig. 7.8a. Although the SAG mask was designed to vary θ, with a step size of 0.5°, since the alternating NW devices were shorted, it was only possible to measure NWFETs with a step-size of 1°. SEM micrographs of the NWFET devices are presented in Fig. 7.8b, corresponding to the black rectangle in Fig. 7.8a. The measurement set-up remains the same as for the experiments described above.

Figures 7.9a-f depict G(V_G) for each θ for NWFETs based on NWs defined by mask openings $W3$ -$W8$. It should be noted that unfortunately, for the in-plane orientation dependent study, it has not been possible to measure the nominally aligned NWs for widths $W4$, $W5$,

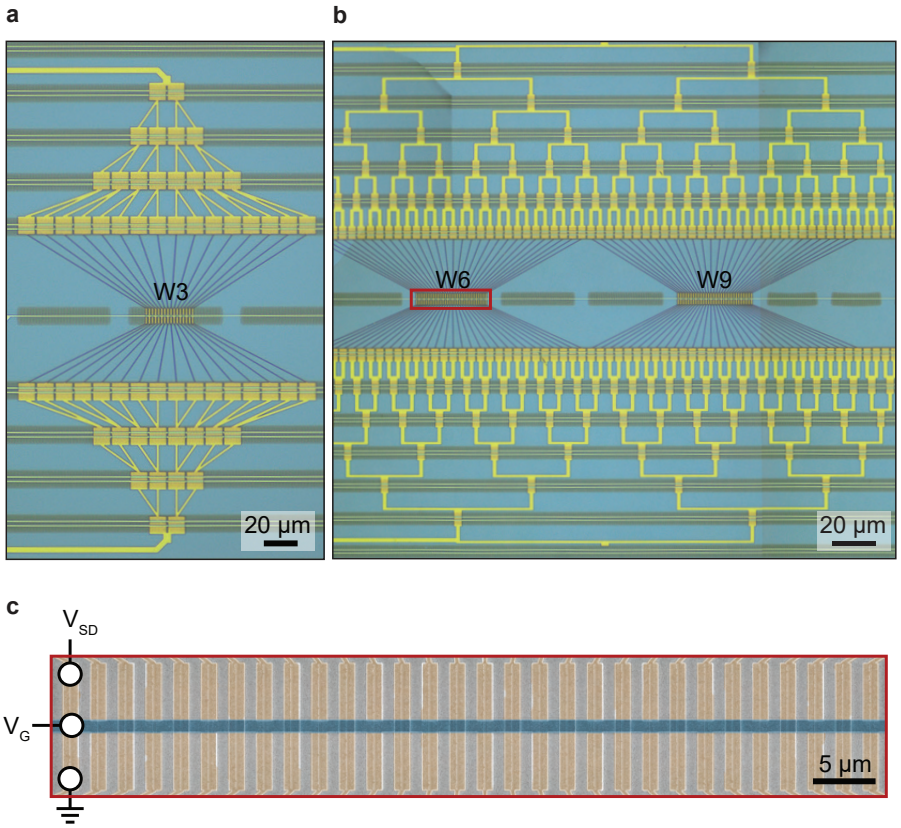

Figure 7.6: a,b Optical microscope micrographs of MUX circuits used to measure NWFET devices based on nominally aligned NWs ($[0\,\bar{1}\,1]$ direction) with widths *W*3, *W*6 and *W*9. **c** SEM micrograph of the of the device circuit from the region highlighted in the red rectangle **b**. Figure and data credit: ***Dags Olsteins***

*W*7 and *W*8, because the choice of the shorted devices. For NWs defined by mask openings *W*6 - *W*8, nonfunctional devices are common and indicated by the red arrows in Fig. 7.9d-f. This correlates very well with what is observed from the structural analysis (see Section6.4.1), where ξ is proceeds to increase for widths *W*6 - *W*8 due to the discontinuous InAs layer. Figures 7.9g-i show V_{TH}^{θ}, $\mu_{\mathrm{FE}}^{\theta}$, and $G_{1.5\mathrm{V}}^{\theta}$ (at fixed $V_{\mathrm{G}} = V_{\mathrm{TH}} + 1.5\,\mathrm{V}$) respectively, with data from non-functional devices eliminated. There is no systematic dependence on θ found for the widths *W*3 - *W*8, although some outliers are identified and indicated with black arrows in Fig. 7.9. These outliers only appear for *W*6 and *W*7, and a likely explanation is that the inconsistent or bad morphology for the InAs layer might result in thin constrictions (A_{min} in Fig. 6.11c) that could act as a bottleneck for electron transport. Interestingly, since the misaligned NWs do not show a trend with increasing mis-orientation, it is very likely that the misalignment of $\theta = \pm 0.5°$ is already detrimental for electron transport, unlike what

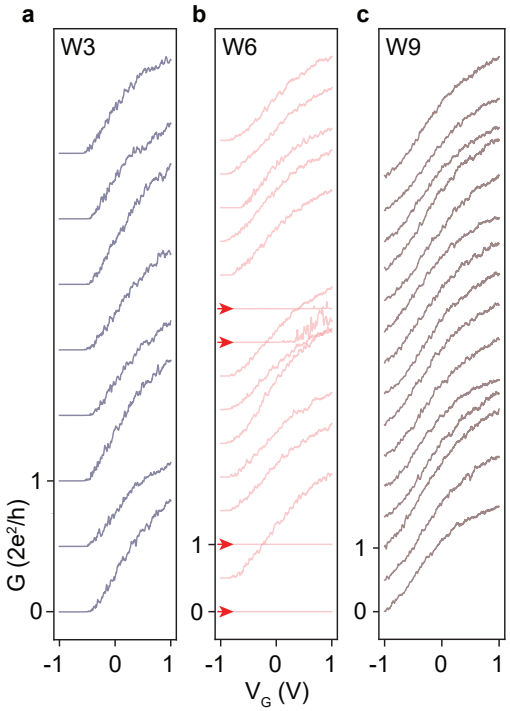

Figure 7.7: a, b, c $G(V_G)$ after subtraction of series resistance (R_s) from alternating shorted devices for nominally oriented NWs with width $W3$, $W6$ and $W9$ respectively. Conductance traces are offset by e^2/h for clarity. The red arrows in **b** correspond to non-functional devices. Figure and data credit: ***Dags Olsteins***

was observed for the structural characteristics such as facet roughness S_q (see Fig. 6.16) where increasing θ continued to increase S_q.

Finally, the transport characteristics for nominally aligned NWs with widths $W3$, $W6$ and $W9$ along with misaligned NWs with width $W3$ and $W6$ are compared and presented in Fig. 7.10. Comparing the V_{TH} and μ_{FE} of the FETs based on nominally aligned NWs to the misoriented NWs (Fig. 7.10a and b) reveals a V_{TH} offset of $+0.2\,\mathrm{mV}$ and a doubling of μ_{FE} for the NWFETs aligned with the high-symmetry crystal direction. This confirms that the alignment of NWs to the high symmetry in-plane orientations is of importance, and even a misorientation as small as $\theta = 0.5°$ can reduce μ_{FE} significantly.

In Fig. 7.10c and d, the electron transport properties of multiple nominally aligned NWFETs based on NWs defined by $W3$, $W6$ and $W9$ are compared, showing V_{TH} and μ_{FE}. From Fig. 7.10c, it is observed that the V_{TH} of the NWFETs decreases from $\approx -0.45\,\mathrm{V}$ to $\approx -0.90\,\mathrm{V}$, which can be attributed to the decreasing channel width. For smaller widths, V_{TH} increases due to quantum confinement effects that have been observed already in narrow channels [116–118]. An increase in μ_{FE} with increasing width is also observed in Fig. 7.10d. As the NW dimensions are proportional to the width, a possible explanation is

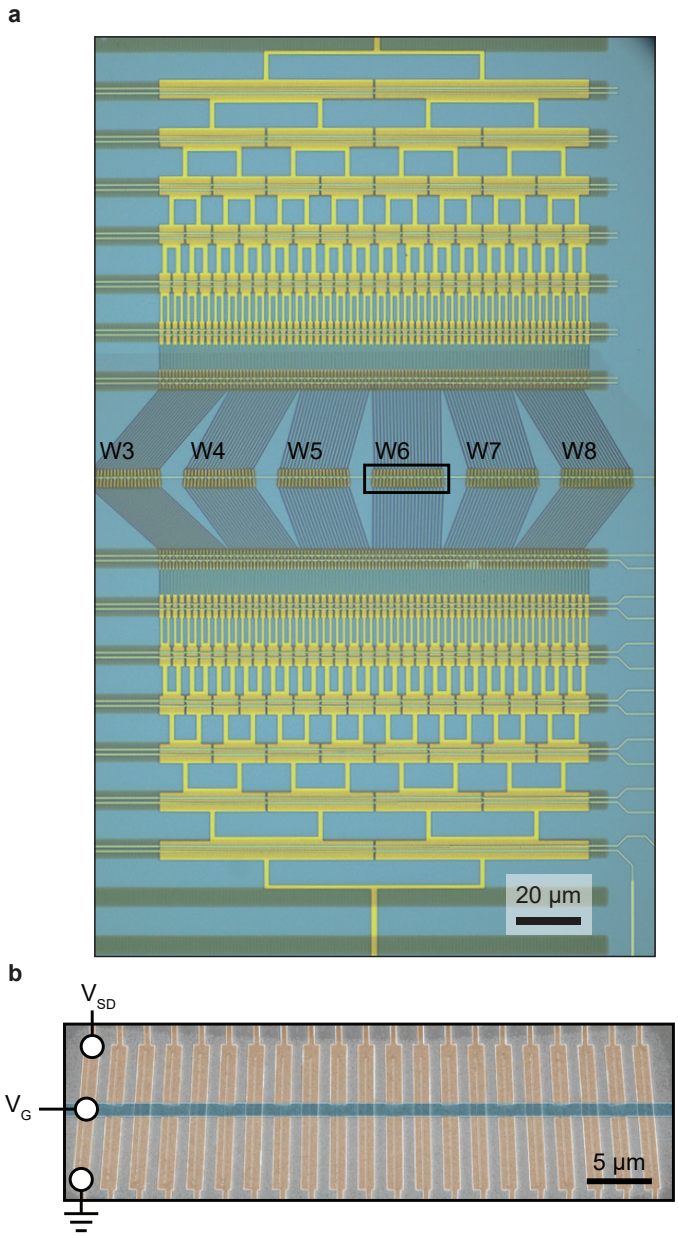

Figure 7.8: a,b Optical microscope micrographs of MUX circuits used to measure NWFET devices based on misaligned NWs, $\theta = \pm 4.5°$ from the $[0\,\bar{1}\,1]$ direction, in steps of $\theta = 1°$ for widths *W*3, *W*4, *W*5 *W*6, *W*7 and *W*8. **c** SEM micrograph of the of the device circuit from the region highlighted in the black rectangle **b**. Figure and data credit: ***Dags Olsteins***.

that for smaller NW widths, scattering at the NW surface plays a more important role [119–121]. The structural study presented in Section6.4.2 shows that strain relaxation is more confined to the vicinity of the InAs/GaAs interface for NWs defined by mask opening *W*9, which may further reduce electron scattering rate and improve μ_{FE}. However, it is important to note that the accuracy of the extracted μ_{FE}

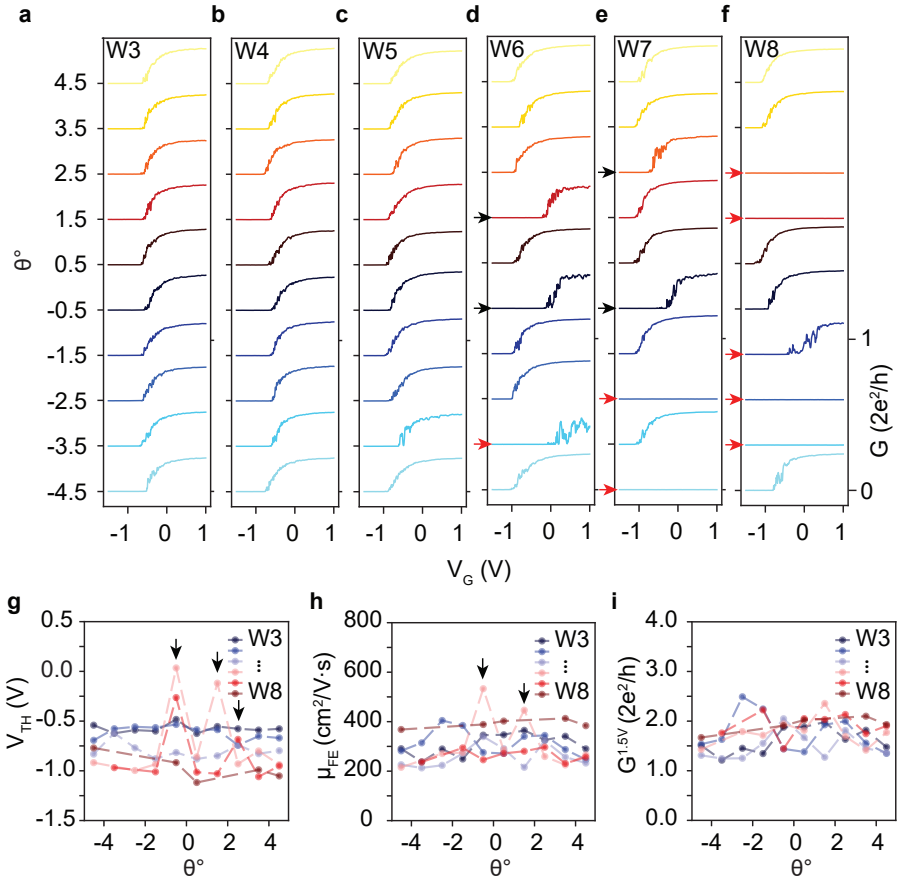

Figure 7.9: a-f Conductance as a function of V_G for $\theta = \pm 4.5°$ and $W3$ - $W8$. Conductance traces a offset in G by $0.3 \times 2e^2/h$ for better visibility. **g-i** V_{TH}, μ_{FE} and $G^{1.5V}$ respectively as function of θ for widths $W3$ - $W8$. Figure and data credit: ***Dags Olsteins***

depends on the estimate of the gate capacitance (details presented in the Supplementary information of publication [3] [111]). Change in NW morphology might have a significant impact on the estimated capacitance. This in turn can affect the observed trend of μ_{FE}. Despite these uncertainties, the strong correlation between the structural and crystal quality of the NWs with width $W9$ with the enhanced μ_{FE} emphasizes the need for a simultaneous systematic study of both aspects of the NWs.

7.6 Gate defined quantum dots

While it is not within the scope of this thesis to describe the physics behind gate defined quantum dots in NWs, the following results are meant as a demonstration of the ability to use InAs SAG NWs as a basis for defining advanced quantum electronics. Going beyond the proof-of-principle demonstrations of single NW devices, it has

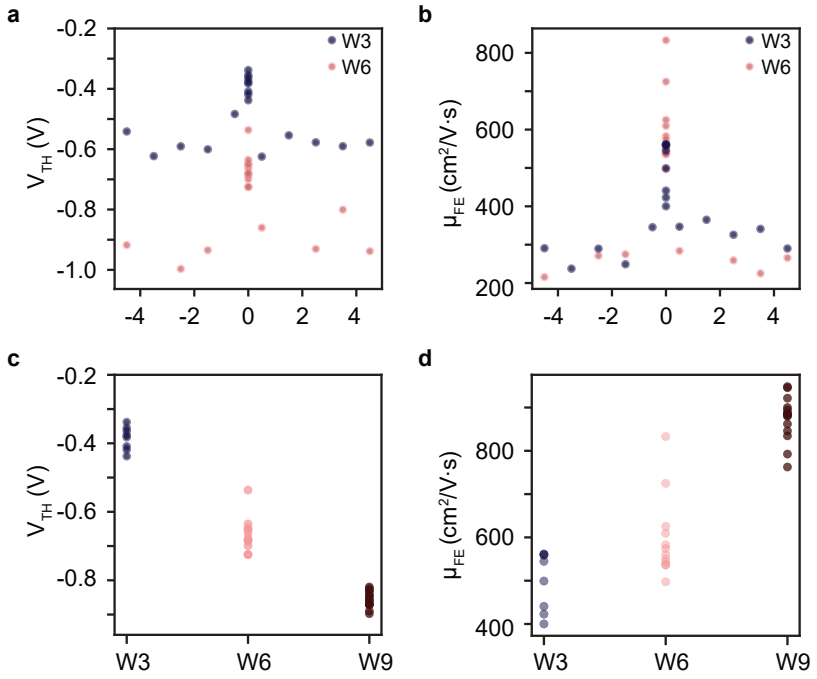

Figure 7.10: **a** $V_{\mathrm{TH}}(\theta)$ for $W3$ and $W6$, along with data from 8 and 15 nominally aligned NWs ($\theta = 0$), respectively. **b** $\mu_{\mathrm{FE}}(\theta)$ for the same set of NWs as in **a**. **c** and **d** present the V_{TH} and μ_{FE} of the nominally aligned NWs for comparison. Figure and data credit: ***Dags Olsteins***

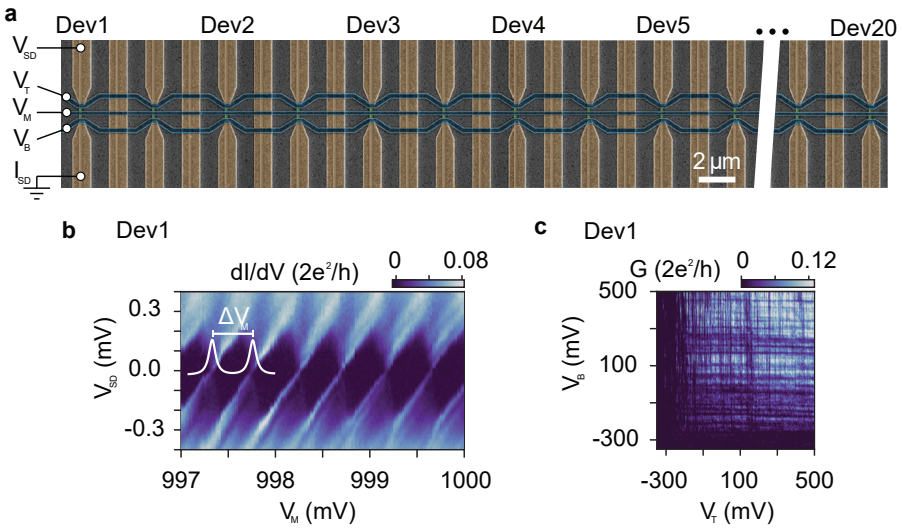

Figure 7.11: An SEM micrograph of a NW array which was used to fabricate gate define quantum dots at every alternate NW. The overlaid colors help identify the three cross-bar gate electrodes (in blue), top (V_{T}), middle (V_{M}) and bottom (V_{B}). Figure and data credit: ***Dags Olsteins***

been possible to scale the device geometry to define quantum dots in 50 individual NW devices and concurrently tune them to Coulomb blockade using only 3 gate electrodes. Figure 7.11a shows an SEM micrograph of an array of NWs where the three gate electrodes (in blue), top (V_T), middle (V_M) and bottom (V_B) were used to confine quantum dots. Each device is alternated with a shorted line for estimating series resistance as reference. The gates are commonly shared across 50 NWs, and data from 1 of them has been presented in Fig. 7.11b and c. Figure 7.11b shows the differential conductance as a function of V_{SD} and V_M for Device 1 which shows Coulomb diamonds. A statistical study for all devices has also been performed ([111]) but is beyond the scope of this thesis.

7.7 Conclusions

In this chapter, the InAs/GaAs(Sb) dual layer SAG NWs have been successfully fabricated into large scale FET devices. The MUX-d/MUX set-up developed has made it possible to address a large number individual (nominally identical) NWs and extract parameters such as the threshold voltage and electron mobility obtain a corresponding statistical significance to them. This also demonstrates that the NWs of the MUX-d/MUX set-up itself are robust and allow for addressing the devices under test. It should be noted that apart from introducing the GaAs(Sb) buffer layer prior to InAs growth, there were no other attempts made to improve the quality of the InAs channel for e.g., to have a higher mobility. Instead, the aim has been to confirm the claims of SAG as a scalable and reproducible method for growing materials that can form the basis of quantum electronics. Despite the lack of optimization, the possibility of being able to address multiple individual NWs, has been utilized to characterize NWs with different dimensions and in-plane orientations. The lower μ_{FE} for NWs misaligned by 0.5° from the high-symmetry in-plane orientation confirms the findings from Chapter 4 that small scale misalignment induced structural disorder indeed has a detrimental effect on electron transport in SAG NWs. The effect of varying NW width on the corresponding V_{TH} and μ_{FE} is directly correlated with the crystal structure of the NWs that were characterized in detail in Chapter 6. NWs with *W*9 show the highest μ_{FE}, which is well correlated with the their crystal structure since these NWs also exhibit the purest InAs channel. Thus, even with a single sample, it has been possible to determine the optimal dimension for the SAG mask design to obtain NWs with a higher μ_{FE}. This method has allowed for a correlation between device geometry and performance that was previously unattainable and opens new possibilities for advancements in electronic devices. The findings are important for optimizing the performance of electronic devices and

understanding the role of scattering mechanisms in limiting electron mobility.

Part IV

Final remarks

8

Conclusions and Outlook

Throughout this thesis, the use of high-index substrates for selective area growth (SAG) of GaAs, GaAs(Sb) and InAs nanowires (NWs) has been explored. These substrate orientations open up the possibility of tailoring the cross-sectional shape of the NWs simply based on the associated symmetry. However, almost all the other results obtained on this endeavour, can be extended to more general studies of growing semiconductor materials (or perhaps other materials too) using SAG.

Effect of in-plane alignment of GaAs NWs

The first study presented the effect of aligning NWs in-plane on the substrate using atomic force microscopy (AFM). Due to the large NW-substrate interface for in-plane NWs, it is imperative to align NWs exactly. It was found that due to fabrication related tolerances, it is not possible to be able to perfectly align the mask openings on the SAG substrate. Consequently, the NW growth which is dictated by surface energy minimization, results in NWs with increased surface roughness on the facets due to not being aligned exactly along the high-symmetry in-plane direction. Structural disorder in the material systems is been known to be a seriously limiting factor in desired transport based applications, and thus, it has be realised in this study that controlling the length of the NWs allows for accommodating a certain small degree of misalignment, thus reducing structural disorder. These considerations would be necessary while designing a device based on SAG NWs.

As a way to furthering the understanding of the tolerance, it would be interesting to see if the NW width plays are role in allowing to accommodate a larger misalignment. Subsequent growth of transport active InAs layers in this thesis already demonstrate that the underlying facet roughness of the buffer layer is carried forward to the next layer, however this was only demonstrated for highly lattice-mismatched system. For example, growth of a ternary InGaAs buffer where the In and Ga composition is adjusted to better match the GaAs, or gradually changed to match InAs even, the effect of this misalignment remains to be seen. Finally, on a more optimistic note,

intentionally misaligned NWs maybe not structurally the best to look at, they have the potential for growth of quantum dots selectively at the stepped facets. This has been demonstrated some time ago [122], where InGaAs dots were grown on intentionally misoriented mesas. Adjusting the growth time to deposit very thin layers of InAs on the misaligned NWs might result is selectively grown InAs quantum dots smaller than what can be obtained using standard SAG.

Engineering NW shapes

This study addressed the previously unexplored use of high-index substrates for SAG of NWs. Due to the epitaxial registry of the SAG NW with the substrate, the resulting NW facets are mostly dictated by the symmetry of the underlying substrate. The high-index surfaces result in NWs with a asymmetric cross-sections, with a combination of steep and flat facets. Moreover, the use of Sb as a surfactant, also influences NWs in certain orientations more than the other by possibly altering the growth rate and adatom kinetics. Even for a fixed growth time, the SAG mask design plays an important role in determining the shape of the NWs since the amount of material available to the NW is dependent on the width of the mask opening, the inter-wire distance, which in turn decides its shape. This highlights the importance of careful design of the SAG mask and simultaneously highlights the benefits of using this bottom-up approach with regards to flexibility and scalability of the material growth.

The results obtained here demonstrate the need for varying the mask dimensions in an even larger parameter space so that analyzing one sample with a variety of designs can help us select the exact NW dimensions desired for an experiment. The asymmetric cross-sections might also be interesting to enable electrical control of spin-orbit interaction in the system [123], where theoretical considerations predict the orientations along which the effective Rashba and Dresselhaus spin-orbit coupling could be tailored depending on the NW cross-sections.

Structural characteristics of InAs/GaAs(Sb) SAG NWs

Large scale structural characterization of InAs/GaAs(Sb) SAG NWs has been demonstrated and the associated variations have been quantified. Moreover, the effect of SAG mask dimensions on the morphology of both the InAs channel and GaAs(Sb) buffers has been studied using AFM. It is found that for the same set of growth conditions, the shape of the NWs and the material incorporation changes with the mask dimensions. The results are supported by the study of the crystal structure and the InAs/GaAs interface. The mask dimensions are also found to affect the In and Ga composition in the NWs along

with varying strain relaxation mechanisms for this lattice-mismatched heterostructure.

As a outlook, it will be very interesting to study the growth of ternary buffers on these NWs geometries in an effort to improve the crystal quality of the InAs layer. The NWs used in the structural reproducibility study were placed close to each other such that there was adatom diffusion across the NWs in the large arrays. It might useful to study NWs spaced far apart from each other, so that the growth is independent and then compare the structural characteristics to determine what leads to a more homogeneous and reproducible growth: independent growth or growth including material being shared.

Electrical characteristics of InAs/GaAs(Sb) SAG NWs

The first demonstration of a very large integration of NW based field effect transistors operating at cryogenic temperatures based on the InAs/GaAs(Sb) SAG NWs has been demonstrated. The ability to address a large number of individual NW devices using a handful of gate electrodes has been possible using a multiplexer/de-multiplexer set-up. Despite no efforts made towards optimizing the material quality, it was found that at least 8192 nominally identical InAs/GaAs(Sb) SAG NWs were operational and allowed for addressing NWs with varying dimensions to study their electrical properties. This allowed for a direct correlation with the structural and crystal quality of the NWs to determine the effect of the material imperfections. The measurements confirmed the detrimental effect of even a 0.5° in-plane misalignment on the mobility of the NWs. Finally, it was also possible to fabricate gate defined quantum dots on 50 individual InAs/GaAs(Sb) SAG NWs using 3 gate electrodes. This demonstrates the realization of the promise of SAG to be able to scale and reproduce.

This thesis did not address the possibility to make NW junctions or networks or grids. Moreover, the list of unanswered questions related to SAG NWs is quite long. For e.g, it is not known whether over-growth of the SAG NWs on the mask oxide introduces structural disorder in the material. The possibility of coupling SAG NWs with geometrically defined quantum dots is also promising. However, to approach these questions, it was essential to first demonstrate the structural and electrical reproducibility of the materials via the SAG approach. Thus, future experiments have been designed using the multiplexer/de-multiplexer set-up, where a vast parameter space of the SAG mask dimensions will be tested. With results obtained with statistical significance, it will be possible to work towards optimization of materials using feedback from the transport characteristics.

Part V

Appendix

A

SAG substrate

- **SiO_2 mask deposition**
  1. The substrates for SAG used in this thesis were undoped semi-insulating GaAs which were 2 inch in diameter and 350 μm thick, all from WaferTech.
  2. Using the PECVD (model SPTS Multiplex) located in the Nanolab cleanroom at the Danish Technical University, deposition of nominally 10 nm thick SiO_2 with the recipe "Std HF SiO_2" for 10 s at 300° C was carried out.
  3. The SiO_2 layer thickness is confirmed by ellipsometry.
- **EBL for SAG mask**
  1. CSAR13 is used as the e-beam resist to spin-coat over the GaAs substrate at 4000 RPM for 45 s.
  2. The substrate covered with resist is then baked for 120 s at 185° C.
  3. Electron beam lithography is performed in an Elionix F-125 with a 125 kV acceleration voltage. Fine structures are expose with an electron dose of 385 $\mu C/cm^2$ and beam current of 1 nA.
  4. Course structures such as alignment markers are exposed with an electron dose of 600 $\mu C/cm^2$ and a beam current of 10 nA.
  5. The exposed resist is then developed in a solution of MIBK:IPA with a 1 : 3 concentration for 30 s.
  6. This is followed with an O_2 plasma ashing for 2 min to rid the substrate of resist residues and possible contaminants.
- **ICP-RIE etch**
  1. The tool used for dry etching of the SiO_2 layer is the III-V ICP-RIE located in the Nanolab cleanroom at the Danish Technical University. First, a chamber cleaning is performed by using O_2 plasma for 30 min with a dummy wafer inside.

2. Next, a recipe titled "NBI/SiO_2 slow" including CF4 and H2 is run for 1 min is run.
3. Following this standard chamber cleaning procedure, the recipe is first run on a calibration GaAs wafer with a thick SiO_2 layer to determine the precise etch rate prior to etching the SAG substrate.
4. The etch rate is determined by measuring the SiO_2 thickness on the calibration wafer using ellipsometry.
5. Next, the SAG substrate is introduced to the chamber and the recipe titled "NBI/SiO_2 slow" is used to etch the exposed SiO_2 regions for $\approx 10 - 30$ s depending on the etch rate.
6. After unloading the SAG substrate, a 30 min chamber cleaning recipe is run with a dummy wafer with a recipe titled "clean/chamber clean O_2".

- **Pre-MBE substrate cleaning**

1. Now the substrate is ready for stripping off of the resist. This is performed by submerging the substrate in N-Methyl-2-pyrrolidone (NMP) for 3 h in a heat-bath at a temperature of 80° C.
2. Next, the substrate is placed in the untrasonicator for 1 min at 30 % power and 80 kHz frequency.
3. It is then transferred to acetone and sonicated with the same recipe as before.
4. It is then transferred to isopropyl alcohol (IPA) and sonicated with the same recipe as before.
5. It is then transferred to MQ water and sonicated with the same recipe as before.
6. Finally, it is rinsed under running MQ water and dried with the N_2 gun.

B

Growth recipes

The MBE beam equivalent pressures are calibrated by conducting planar GaAs and InGaAs growth on GaAs(1 0 0) substrates using RHEED oscillations under conditions where desorption of group III can be ignored. The V:III ratio corresponding to a Ga and As flux for which the GaAs growth is dictated equivalently by both species (i.e., a 1:1 ratio) is calibrated by identifying the surface reconstruction of the GaAs(1 0 0) surface using RHEED [124, 125].

Prior to MBE growth, the substrate is thermally annealed twice: at 400° C in the transfer module for 60 min to remove organic contaminants, and at 620° C under As_4 over-pressure in the growth chamber for ≈ 18 min to remove the native oxide from the GaAs surface. The growth parameters listed below are based on a previously established range of parameters ensuring growth on the exposed GaAs substrate without parasitic growth on the SiO_2 mask [55]. The Ga and In growth rates correspond to planar growth on a GaAs(1 0 0) substrate.

- **GaAs or GaAs(Sb) growth**

  $T_{GaAs} = 600°\,C$
  As/Ga ratio = 9
  Sb/Ga ratio = 3 (for GaAs(Sb) growths)
  Ga growth rate = 0.1 ML/s
  Growth time = 30 min

- **GaAs + $In_xGa_{1-x}As$ growth (high T)**

  1. $T_{GaAs} = 622°\,C$
     As/Ga ratio = 9
     Sb/Ga ratio = 3
     Ga growth rate = 0.1 ML/s
     Growth time = 30 min
  2. $T_{InAs} = 537°\,C$
     As/In ratio = 9
     In growth rate = 0.04 ML/s
     Growth time = 30 min

- **GaAs + $In_xGa_{1-x}As$ growth (low T)**

1. $T_{\mathrm{GaAs}} = 602°\,\mathrm{C}$
   As/Ga ratio = 9
   Sb/Ga ratio = 3
   Ga growth rate = 0.1 ML/s
   Growth time = 30 min
2. $T_{\mathrm{InAs}} = 522°\,\mathrm{C}$
   As/In ratio = 9
   In growth rate = 0.04 ML/s
   Growth time = 30 min

- **GaAs(Sb) + InAs growth**

1. $T_{\mathrm{GaAs}} = 600°\,\mathrm{C}$
   As/Ga ratio = 9
   Sb/Ga ratio = 3
   Ga growth rate = 0.1 ML/s
   Growth time = 30 min
2. $T_{\mathrm{InAs}} = 500°\,\mathrm{C}$
   As/In ratio = 9
   In growth rate = 0.06 ML/s
   Growth time = (varied) 5 min, 10 min and 18 min

C

AFM operating parameters

We use the Bruker Dimension Icon AFM system in the ScanAsyst Air mode which is a topographical intermediate contact mode [75]. The optimal choice of the cantilever for imaging NWs was a SiN probe with a nominal spring constant of $\sim 0.4\,\mathrm{N/m}$, a nominal resonance frequency of $\sim 75\,\mathrm{kHz}$ and a nominal tip radius of $\sim 2\,\mathrm{nm}$. It is possible to modulate the tip motion of a soft cantilever through this mode and thus tip wear is reduced compared to tapping mode resulting in an accurate acquisition of topographical data. All scans are performed using a scan rate of $0.3 - 0.4\,\mathrm{Hz}$ with 1024 or 2048 samples per line (for high resolution images required to calculate running average of P and H). The choice of scan rate is such that the trace and retrace overlap is minimized. NWs were scanned across the length for volume incorporation measurements and along the length for the facet roughness (S_q) measurements.

D

TEM operating parameters

FIB-lamellae were prepared mainly using a FEI Dual-Beam Helios Nanolab 650 located at Instituto de Nanociencia de Aragon, Zaragoza. The lamellae were extracted directly from regions of interest on the substrate containing the as-grown nanowires. First there is a electron deposition of Pt-C followed by an ion deposition of Pt-C for adding a protective layer, then the region of interest is milled and a slice of it is extracted with a needle, which is then attached to the TEM grid and thinned by ion milling until it is electron transparent.

Aberration corrected TEM data was acquired in a probe corrected TITAN operated at 300 kV, which is located in the Laboratorio de Microscopías Avanzadas of the Instituto de Nanociencia de Aragon (INA-LMA). EELS maps were acquired in a TECNAI F20 microscope located in the Catalan Institute of Nanoscience and Nanotechnology (ICN2) operated at 200 kV.

Bibliography

[1] Richard P. Feynman. "There's plenty of room at the bottom [data storage]." In: *J. Microelectromech. Syst.* 1.1 (Mar. 1992), pp. 60–66. ISSN: 1941-0158. DOI: 10.1109/84.128057.

[2] R. R. Schaller. "Moore's law: past, present and future." In: *IEEE Spectr.* 34.6 (June 1997), pp. 52–59. ISSN: 1939-9340. DOI: 10.1109/6.591665.

[3] Martin Fuechsle, Jill A. Miwa, Suddhasatta Mahapatra, Hoon Ryu, Sunhee Lee, Oliver Warschkow, Lloyd C. L. Hollenberg, Gerhard Klimeck, and Michelle Y. Simmons. "A single-atom transistor." In: *Nat. Nanotechnol.* 7 (Apr. 2012), pp. 242–246. ISSN: 1748-3395. DOI: 10.1038/nnano.2012.21.

[4] Rashmit Patel, Yash Agrawal, and Rutu Parekh. "Single-electron transistor: review in perspective of theory, modelling, design and fabrication." In: *Microsyst. Technol.* 27.5 (May 2021), pp. 1863–1875. ISSN: 1432-1858. DOI: 10.1007/s00542-020-05002-5.

[5] Jin Zhang, Hailin Peng, Hua Zhang, Shigeo Maruyama, and Li Lin. "The Roadmap of Graphene: From Fundamental Research to Broad Applications." In: *Adv. Funct. Mater.* 32.42 (Oct. 2022), p. 2208378. ISSN: 1616-301X. DOI: 10.1002/adfm.202208378.

[6] F. Pelayo García de Arquer, Dmitri V. Talapin, Victor I. Klimov, Yasuhiko Arakawa, Manfred Bayer, and Edward H. Sargent. "Semiconductor quantum dots: Technological progress and future challenges." In: *Science* 373.6555 (Aug. 2021), eaaz8541. ISSN: 0036-8075. DOI: 10.1126/science.aaz8541.

[7] Feliciano Giustino et al. "The 2021 quantum materials roadmap." In: *J. Phys.: Mater.* 3.4 (Jan. 2021), p. 042006. ISSN: 2515-7639. DOI: 10.1088/2515-7639/abb74e.

[8] Galan Moody et al. "2022 Roadmap on integrated quantum photonics." In: *J. Phys.: Photonics* 4.1 (Jan. 2022), p. 012501. ISSN: 2515-7647. DOI: 10.1088/2515-7647/ac1ef4.

[9] Gage Hills et al. "Modern microprocessor built from complementary carbon nanotube transistors." In: *Nature* 572 (Aug. 2019), pp. 595–602. ISSN: 1476-4687. DOI: 10.1038/s41586-019-1493-8.

[10] Aaron D. Franklin, Mark C. Hersam, and H.-S. Philip Wong. "Carbon nanotube transistors: Making electronics from molecules." In: *Science* 378.6621 (Nov. 2022), pp. 726–732. ISSN: 0036-8075. DOI: 10.1126/science.abp8278.

[11] Christoph Becher et al. "2023 roadmap for materials for quantum technologies." In: *Mater. Quantum Technol.* 3.1 (Jan. 2023), p. 012501. ISSN: 2633-4356. DOI: 10.1088/2633-4356/aca3f2.

[12] Ting-Wei Yeh, Yen-Ting Lin, Byungmin Ahn, Lawrence S. Stewart, P. Daniel Dapkus, and Steven R. Nutt. "Vertical nonpolar growth templates for light emitting diodes formed with GaN nanosheets." In: *Appl. Phys. Lett.* 100.3 (Jan. 2012). ISSN: 0003-6951. DOI: 10.1063/1.3671182.

[13] Julia Winnerl, Max Kraut, Sabrina Artmeier, and Martin Stutzmann. "Selectively grown GaN nanowalls and nanogrids for photocatalysis: growth and optical properties." In: *Nanoscale* 11.10 (Mar. 2019), pp. 4578–4584. ISSN: 2040-3364. DOI: 10.1039/C8NR09094G.

[14] Naiyin Wang, Xiaoming Yuan, Xu Zhang, Qian Gao, Bijun Zhao, Li Li, Mark Lockrey, Hark Hoe Tan, Chennupati Jagadish, and Philippe Caroff. "Shape Engineering of InP Nanostructures by Selective Area Epitaxy." In: *ACS Nano* 13.6 (June 2019), pp. 7261–7269. ISSN: 1936-0851. DOI: 10.1021/acsnano.9b02985.

[15] Marco Albani, Lea Ghisalberti, Roberto Bergamaschini, Martin Friedl, Marco Salvalaglio, Axel Voigt, Francesco Montalenti, Gözde Tütüncüoglu, Anna Fontcuberta i. Morral, and Leo Miglio. "Growth kinetics and morphological analysis of homoepitaxial GaAs fins by theory and experiment." In: *Phys. Rev. Mater.* 2.9 (Sept. 2018), p. 093404. ISSN: 2475-9953. DOI: 10.1103/PhysRevMaterials.2.093404.

[16] Chun-Yung Chi, Chia-Chi Chang, Shu Hu, Ting-Wei Yeh, Stephen B. Cronin, and P. Daniel Dapkus. "Twin-Free GaAs Nanosheets by Selective Area Growth: Implications for Defect-Free Nanostructures." In: *Nano Lett.* 13.6 (June 2013), pp. 2506–2515. ISSN: 1530-6984. DOI: 10.1021/nl400561j.

[17] J. Seidl, J. G. Gluschke, X. Yuan, S. Naureen, N. Shahid, H. H. Tan, C. Jagadish, A. P. Micolich, and P. Caroff. "Regaining a Spatial Dimension: Mechanically Transferrable Two-Dimensional InAs Nanofins Grown by Selective Area Epitaxy." In: *Nano Lett.* 19.7 (July 2019), pp. 4666–4677. ISSN: 1530-6984. DOI: 10.1021/acs.nanolett.9b01703.

[18] Xiaoming Yuan, Dong Pan, Yijin Zhou, Xutao Zhang, Kun Peng, Bijun Zhao, Mingtang Deng, Jun He, Hark Hoe Tan, and Chennupati Jagadish. "Selective area epitaxy of III–V nanostructure arrays and networks: Growth, applications, and future directions." In: *Appl. Phys. Rev.* 8.2 (June 2021), p. 021302. ISSN: 1931-9401. DOI: 10.1063/5.0044706.

[19] Filip Krizek et al. "Field effect enhancement in buffered quantum nanowire networks." In: *Phys. Rev. Mater.* 2.9 (Sept. 2018), p. 093401. ISSN: 2475-9953. DOI: 10.1103/PhysRevMaterials.2.093401.

[20] Joon Sue Lee et al. "Selective-area chemical beam epitaxy of in-plane InAs one-dimensional channels grown on InP(001), InP(111)B, and InP(011) surfaces." In: *Phys. Rev. Mater.* 3.8 (Aug. 2019), p. 084606. ISSN: 2475-9953. DOI: 10.1103/PhysRevMaterials.3.084606.

[21] Daria V. Beznasyuk et al. "Doubling the mobility of InAs/InGaAs selective area grown nanowires." In: *Phys. Rev. Mater.* 6.3 (Mar. 2022), p. 034602. ISSN: 2475-9953. DOI: 10.1103/PhysRevMaterials.6.034602.

[22] Martin Espiñeira Cachaza, Anna Wulff Christensen, Daria Beznasyuk, Tobias Særkjær, Morten Hannibal Madsen, Rawa Tanta, **Gunjan Nagda**, Sergej Schuwalow, and Peter Krogstrup. "***Selective area growth rates of III-V nanowires***." In: *Phys. Rev. Mater.* 5.9 (Sept. 2021), p. 094601. ISSN: 2475-9953. DOI: 10.1103/PhysRevMaterials.5.094601.

[23] Akihiko Ishitani, Hiroshi Kitajima, Nobuhiro Endo, and Naoki Kasai. "Facet Formation in Selective Silicon Epitaxial Growth." In: *Jpn. J. Appl. Phys.* 24.Part 1, No. 10 (Oct. 1985), pp. 1267–1269. ISSN: 0021-4922. DOI: 10.1143/jjap.24.1267.

[24] Takumi Yamada Takumi Yamada and Yoshiji Horikoshi Yoshiji Horikoshi. "Comparison of GaAs Facet Formation on Patterned Substrate during Molecular Beam Epitaxy and Migration Enhanced Epitaxy." In: *Jpn. J. Appl. Phys.* 33.Part 2, No. 7B (July 1994), pp. L1027–L1030. ISSN: 0021-4922. DOI: 10.1143/jjap.33.l1027.

[25] Hiroaki Kuriyama Hiroaki Kuriyama, Masahiro Ito Masahiro Ito, Keita Suzuki Keita Suzuki, and Yoshiji Horikoshi Yoshiji Horikoshi. "Determination of the Facet Index in Area Selective Epitaxy of GaAs." In: *Jpn. J. Appl. Phys.* 39.Part 1, No. 4B (Apr. 2000), pp. 2457–2459. ISSN: 0021-4922. DOI: 10.1143/jjap.39.2457.

[26] Isao Tamai, Taketomo Sato, and Hideki Hasegawa. "Cross-Sectional Evolution and Its Mechanism during Selective Molecular Beam Epitaxy Growth of GaAs Quantum Wires on (111)B Substrates." In: *Jpn. J. Appl. Phys.* 44.4B (Apr. 2005), pp. 2652–2656. ISSN: 0021-4922. DOI: 10.1143/jjap.44.2652.

[27] Taketomo Sato, Isao Tamai, and Hideki Hasegawa. "Growth kinetics and theoretical modeling of selective molecular beam epitaxy for growth of GaAs nanowires on nonplanar (001) and (111)B substrates." In: *Journal of Vacuum Science & Technology*

B: Microelectronics and Nanometer Structures Processing, Measurement, and Phenomena 23.4 (July 2005), p. 1706. ISSN: 1071-1023. DOI: 10.1116/1.1949222.

[28] Mattias Borg et al. "Facet-selective group-III incorporation in InGaAs template assisted selective epitaxy." In: *Nanotechnology* 30.8 (Dec. 2018), p. 084004. ISSN: 0957-4484. DOI: 10.1088/1361-6528/aaf547.

[29] L. Desplanque, M. Fahed, X. Han, V. K. Chinni, D. Troadec, M.-P. Chauvat, P. Ruterana, and X. Wallart. "Influence of nanoscale faceting on the tunneling properties of near broken gap InAs/AlGaSb heterojunctions grown by selective area epitaxy." In: *Nanotechnology* 25.46 (Oct. 2014), p. 465302. ISSN: 0957-4484. DOI: 10.1088/0957-4484/25/46/465302.

[30] Lunjie Zeng, Christoph Gammer, Burak Ozdol, Thomas Nordqvist, Jesper Nygård, Peter Krogstrup, Andrew M. Minor, Wolfgang Jäger, and Eva Olsson. "Correlation between Electrical Transport and Nanoscale Strain in InAs/Ino.6Gao.4As Core–Shell Nanowires." In: *Nano Lett.* 18.8 (Aug. 2018), pp. 4949–4956. ISSN: 1530-6984. DOI: 10.1021/acs.nanolett.8b01782.

[31] **Gunjan Nagda**, Daria V. Beznasyuk, Jesper Nygård, and Thomas Sand Jespersen. "***Effect of in-plane alignment on selective area grown homo-epitaxial nanowires***." In: *Nanotechnology* (Apr. 2023). ISSN: 0957-4484. DOI: 10.1088/1361-6528/acca27.

[32] Karl W Böer and Udo W Pohl. *Semiconductor physics*. Springer Nature, 2023.

[33] K. Momma and F. Izumi. "VESTA 3 for three-dimensional visualization of crystal, volumetric and morphology data." In: *J. Appl. Crystallogr.* 44.6 (Dec. 2011), pp. 1272–1276. ISSN: 0021-8898. DOI: 10.1107/S0021889811038970.

[34] J. Platen, C. Setzer, P. Geng, W. Ranke, and K. Jacobi. "Geometric and electronic structure of molecular beam epitaxy-prepared GaAs (112) and (113) surfaces." In: *Microelectron. J.* 28.8 (Oct. 1997), pp. 969–976. ISSN: 0026-2692. DOI: 10.1016/S0026-2692(96)00136-X.

[35] L. Geelhaar, J. Márquez, K. Jacobi, A. Kley, P. Ruggerone, and M. Scheffler. "A scanning tunneling microscopy study of the GaAs(112) surfaces." In: *Microelectron. J.* 30.4 (Apr. 1999), pp. 393–396. ISSN: 0026-2692. DOI: 10.1016/S0026-2692(98)00141-4.

[36] J. Platen, A. Kley, C. Setzer, K. Jacobi, P. Ruggerone, and M. Scheffler. "The importance of high-index surfaces for the morphology of GaAs quantum dots." In: *J. Appl. Phys.* 85.7 (Apr. 1999), pp. 3597–3601. ISSN: 0021-8979. DOI: 10.1063/1.369720.

[37] Y. Hsu. "Molecular beam epitaxial heterostructures in the (311)A orientation." In: *Journal of Vacuum Science Technology B: Microelectronics and Nanometer Structures* 12.4 (1994), p. 2584. ISSN: 0734211X. DOI: 10.1116/1.587806.

[38] M. Wassermeier, J. Sudijono, M. D. Johnson, K. T. Leung, B. G. Orr, L. Däweritz, and K. Ploog. "Reconstruction of the GaAs (311)A surface." In: *Physical Review B* 51.20 (1995), pp. 14721–14724. ISSN: 01631829. DOI: 10.1103/PhysRevB.51.14721.

[39] Z. M. Wang, V. R. Yazdanpanah, J. L. Shultz, and G. J. Salamo. "GaAs(311) templates for molecular beam epitaxy growth: Surface morphologies and reconstruction." In: *Applied Physics Letters* 81.16 (2002), pp. 2965–2967. ISSN: 00036951. DOI: 10.1063/1.1514822.

[40] Makoto Kawase, Yasuhiko Ishikawa, and Takashi Fukui. "Atomic structure studies of (113)B GaAs surfaces grown by metallorganic vapor phase epitaxy." In: *Applied Surface Science* 130-132 (1998), pp. 457–463. ISSN: 01694332. DOI: 10.1016/S0169-4332(98)00101-9.

[41] Udo W. Pohl. *Epitaxy of Semiconductors*. Berlin, Germany: Springer, 2013. ISBN: 978-3-642-32970-8. URL: https://link.springer.com/book/10.1007/978-3-642-32970-8.

[42] C. J. Palmstrom. "Epitaxy of Dissimilar Materials." In: *Annu. Rev. Mater. Sci.* 25.1 (Aug. 1995), pp. 389–415. ISSN: 0084-6600. DOI: 10.1146/annurev.ms.25.080195.002133.

[43] J. W. Matthews. "Defects associated with the accommodation of misfit between crystals." In: *Journal of Vacuum Science and Technology* 12.1 (Jan. 1975), pp. 126–133. ISSN: 0022-5355. DOI: 10.1116/1.568741.

[44] Jan H. van der Merwe. "Misfit dislocation generation in epitaxial layers." In: *Crit. Rev. Solid State Mater. Sci.* 17.3 (Jan. 1991), pp. 187–209. ISSN: 1040-8436. DOI: 10.1080/10408439108243751.

[45] Brian W. Dodson and Jeffrey Y. Tsao. "Relaxation of strained-layer semiconductor structures via plastic flow." In: *Appl. Phys. Lett.* 51.17 (Oct. 1987), pp. 1325–1327. ISSN: 0003-6951. DOI: 10.1063/1.98667.

[46] Frank Frederick Charles and H. Van Der Merwe J. "One-dimensional dislocations. II. Misfitting monolayers and oriented overgrowth." In: *Proc. R. Soc. London A - Math. Phys. Sci.* 198.1053 (Aug. 1949), pp. 216–225. ISSN: 2053-9169. DOI: 10.1098/rspa.1949.0096.

[47] M. Volmer and . Weber. "Keimbildung in übersättigten Gebilden." In: *Z. Phys. Chem.* 119U.1 (Jan. 1926), pp. 277–301. ISSN: 2196-7156. DOI: 10.1515/zpch-1926-11927.

[48] I. N. Stranski and L. Krastanow. "Zur Theorie der orientierten Ausscheidung von Ionenkristallen aufeinander." In: *Monatshefte für Chemie* 71.1 (Dec. 1937), pp. 351–364. ISSN: 1434-4475. DOI: 10.1007/BF01798103.

[49] Marcia H. Grabow and George H. Gilmer. "Thin film growth modes, wetting and cluster nucleation." In: *Surf. Sci.* 194.3 (Jan. 1988), pp. 333–346. ISSN: 0039-6028. DOI: 10.1016/0039-6028(88)90858-8.

[50] J. A. Floro, S. J. Hearne, J. A. Hunter, P. Kotula, E. Chason, S. C. Seel, and C. V. Thompson. "The dynamic competition between stress generation and relaxation mechanisms during coalescence of Volmer–Weber thin films." In: *J. Appl. Phys.* 89.9 (May 2001), pp. 4886–4897. ISSN: 0021-8979. DOI: 10.1063/1.1352563.

[51] Jason Jung, Sander G. Schellingerhout, Orson A. H. van der Molen, Wouter H. J. Peeters, Marcel A. Verheijen, and Erik P. A. M. Bakkers. "Single-crystalline PbTe film growth through reorientation." In: *Phys. Rev. Mater.* 7.2 (Feb. 2023), p. 023401. ISSN: 2475-9953. DOI: 10.1103/PhysRevMaterials.7.023401.

[52] D. Fricker, P. Atkinson, X. Jin, M. Lepsa, Z. Zeng, A. Kovács, L. Kibkalo, R. E. Dunin-Borkowski, and B. E. Kardynał. "Effect of surface gallium termination on the formation and emission energy of an InGaAs wetting layer during the growth of InGaAs quantum dots by droplet epitaxy." In: *Nanotechnology* 34.14 (Jan. 2023), p. 145601. ISSN: 0957-4484. DOI: 10.1088/1361-6528/acabd1.

[53] J. J. Zhang et al. "Monolithic Growth of Ultrathin Ge Nanowires on Si(001)." In: *Phys. Rev. Lett.* 109.8 (Aug. 2012), p. 085502. ISSN: 1079-7114. DOI: 10.1103/PhysRevLett.109.085502.

[54] Fei Gao et al. "Site-Controlled Uniform Ge/Si Hut Wires with Electrically Tunable Spin–Orbit Coupling." In: *Adv. Mater.* 32.16 (Apr. 2020), p. 1906523. ISSN: 0935-9648. DOI: 10.1002/adma.201906523.

[55] Pavel Aseev et al. "Selectivity Map for Molecular Beam Epitaxy of Advanced III–V Quantum Nanowire Networks." In: *Nano Lett.* 19.1 (Jan. 2019), pp. 218–227. ISSN: 1530-6984. DOI: 10.1021/acs.nanolett.8b03733.

[56] Roy LM Op het Veld, Di Xu, Vanessa Schaller, Marcel A Verheijen, Stan ME Peters, Jason Jung, Chuyao Tong, Qingzhen Wang, Michiel WA de Moor, Bart Hesselmann, et al. "In-Plane Selective Area InSb–Al Nanowire Quantum Networks." In: *Communications Physics* 3.1 (2020), pp. 1–7.

[57] A. Okamoto and K. Ohata. "Selective epitaxial growth of gallium arsenide by molecular beam epitaxy." In: *Appl. Phys. Lett.* 51.19 (Nov. 1987), pp. 1512–1514. ISSN: 0003-6951. DOI: 10.1063/1.98619.

[58] Akihiko Okamoto and Keiichi Ohata. "Selective Epitaxial Growth of InAs on GaAs by Molecular Beam Epitaxy." In: *Jpn. J. Appl. Phys.* 26.7A (July 1987), p. L1174. ISSN: 1347-4065. DOI: 10.1143/JJAP.26.L1174.

[59] G. Tutuncuoglu, M. de la Mata, D. Deiana, H. Potts, F. Matteini, J. Arbiol, and A. Fontcuberta i. Morral. "Towards defect-free 1-D GaAs/AlGaAs heterostructures based on GaAs nanomembranes." In: *Nanoscale* 7.46 (2015), pp. 19453–19460. DOI: 10.1039/C5NR04821D.

[60] M. Fahed, L. Desplanque, C. Coinon, D. Troadec, and X. Wallart. "Impact of P/In flux ratio and epilayer thickness on faceting for nanoscale selective area growth of InP by molecular beam epitaxy." In: *Nanotechnology* 26.29 (July 2015), p. 295301. ISSN: 0957-4484. DOI: 10.1088/0957-4484/26/29/295301.

[61] Peter Krogstrup, Henrik I. Jørgensen, Erik Johnson, Morten Hannibal Madsen, Claus B. Sørensen, Anna Fontcuberta i. Morral, Martin Aagesen, Jesper Nygård, and Frank Glas. "Advances in the theory of III–V nanowire growth dynamics." In: *J. Phys. D: Appl. Phys.* 46.31 (July 2013), p. 313001. ISSN: 0022-3727. DOI: 10.1088/0022-3727/46/31/313001.

[62] In Won Yeu, Gyuseung Han, Jaehong Park, Cheol Seong Hwang, and Jung Hae Choi. "Equilibrium crystal shape of GaAs and InAs considering surface vibration and new (111)B reconstruction: ab-initio thermodynamics." In: *Scientific Reports* 9.1 (2019), pp. 1–9. ISSN: 20452322. DOI: 10.1038/s41598-018-37910-y.

[63] Richard Tran, Zihan Xu, Balachandran Radhakrishnan, Donald Winston, Wenhao Sun, Kristin A. Persson, and Shyue Ping Ong. "Surface energies of elemental crystals." In: *Sci. Data* 3.160080 (Sept. 2016), pp. 1–13. ISSN: 2052-4463. DOI: 10.1038/sdata.2016.80.

[64] Qian Sun, Christopher D. Yerino, Benjamin Leung, Jung Han, and Michael E. Coltrin. "Understanding and controlling heteroepitaxy with the kinetic Wulff plot: A case study with GaN." In: *J. Appl. Phys.* 110.5 (Sept. 2011). ISSN: 0021-8979. DOI: 10.1063/1.3632073.

[65] W. Ranke and K. Jacobi. "Structure and reactivity of GaAs surfaces." In: *Prog. Surf. Sci.* 10.1 (Jan. 1981), pp. 1–52. ISSN: 0079-6816. DOI: 10.1016/0079-6816(81)90005-8.

[66] Yoshihiro Kangawa, Toru Akiyama, Tomonori Ito, Kenji Shiraishi, and Takashi Nakayama. "Surface Stability and Growth Kinetics of Compound Semiconductors: An Ab Initio-Based Approach." In: *Materials* 6.8 (Aug. 2013), pp. 3309–3360. ISSN: 1996-1944. DOI: 10.3390/ma6083309.

[67] Xiaoming Yuan, Jiabao Yang, Jun He, Hark Hoe Tan, and Chennupati Jagadish. "Role of surface energy in nanowire growth." In: *J. Phys. D: Appl. Phys.* 51.28 (June 2018), p. 283002. ISSN: 0022-3727. DOI: 10.1088/1361-6463/aac9f4.

[68] *WinWULFF (Stereogram, Stereographic Projection, Wulff-net, Simulation Software)*. [Online; accessed 17. May 2022]. Sept. 2018. URL: http://www.jcrystal.com/products/winwulff.

[69] *E-Beam Resist AR-P 6200 series (CSAR 62) - Allresist EN*. [Online; accessed 31. May 2022]. Sept. 2021. URL: https://www.allresist.com/portfolio-item/e-beam-resist-ar-p-6200-series-csar-62/#tab-id-3.

[70] K. Y. Cheng. "Development of molecular beam epitaxy technology for III–V compound semiconductor heterostructure devices." In: *J. Vac. Sci. Technol., A* 31.5 (Sept. 2013). ISSN: 0734-2101. DOI: 10.1116/1.4816932.

[71] B. A. Joyce. "Molecular beam epitaxy-fundamentals and current status." In: *Contemp. Phys.* 31.3 (May 1990), pp. 195–197. ISSN: 0010-7514. DOI: 10.1080/00107519008222015.

[72] Yoshimi Horio, Yasuyuki Hashimoto, and Ayahiko Ichimiya. "A new type of RHEED apparatus equipped with an energy filter." In: *Appl. Surf. Sci.* 100-101 (July 1996), pp. 292–296. ISSN: 0169-4332. DOI: 10.1016/0169-4332(96)00229-2.

[73] *File:AFM schematic (EN).svg - Wikipedia*. Schematic of an atomic force microscope with optical detection of the deflection of the microcantilever. Apr. 2023. URL: https://en.wikipedia.org/wiki/File:AFM_schematic_(EN).svg.

[74] Bert Voigtländer. "Forces Between Tip and Sample." In: *Scanning Probe Microscopy*. Berlin, Germany: Springer, Feb. 2015, pp. 145–155. DOI: 10.1007/978-3-662-45240-0_11.

[75] *Dimension Icon AFM*. [Bruker Systems]. URL: https://www.bruker.com/en/products-and-solutions/microscopes/materials-afm/dimension-icon-afm.html.

[76] B. Cappella and G. Dietler. "Force-distance curves by atomic force microscopy." In: *Surf. Sci. Rep.* 34.1 (Jan. 1999), pp. 1–104. ISSN: 0167-5729. DOI: 10.1016/S0167-5729(99)00003-5.

[77] Anna Wulff Christensen. "Statistical Analysis of Selective Area Grown Nanowire Crystal Morphologies." Master's thesis. University of Copenhagen, 2019. URL: https://qdev.nbi.ku.dk/calender/2019/masters-defense-anna-wulff-christensen.

[78] *The Scanning Electron Microscope | Engineering Atoms*. Schematic of a scanning electron microscope. Apr. 2023. URL: https://www.eng-atoms.msm.cam.ac.uk/RoyalSocDemos/SEM.

[79] S. Amelinckx, Dirk van Dyck, J. van Landuyt, and Gustaaf van Tendeloo. *Electron Microscopy: Principles and Fundamentals*. Weinheim, Germany: Wiley, Sept. 2008. ISBN: 978-3-527-61455-4. URL: https://www.wiley.com/en-us/Electron+Microscopy%3A+Principles+and+Fundamentals-p-9783527614554.

[80] David B. Williams and C. Barry Carter. *Transmission Electron Microscopy*. Springer US, 2009. ISBN: 978-0-387-76501-3. URL: https://link.springer.com/book/10.1007/978-0-387-76501-3.

[81] L.A. Giannuzzi and N.C.S. University. *Introduction to Focused Ion Beams: Instrumentation, Theory, Techniques and Practice*. Springer US, 2004. ISBN: 9780387231167. URL: https://books.google.dk/books?id=h1sM6iwg4-wC.

[82] Karl W. Böer and Udo W. Pohl. "Crystal Defects." In: *Semiconductor Physics*. Cham, Switzerland: Springer, Aug. 2017, pp. 1–54. DOI: 10.1007/978-3-319-06540-3_15-4.

[83] I. Markov and S. Stoyanov. "Mechanisms of epitaxial growth." In: *Contemp. Phys.* 28.3 (May 1987), pp. 267–320. ISSN: 0010-7514. DOI: 10.1080/00107518708219073.

[84] M. Quirk and J. Serda. *Semiconductor Manufacturing Technology*. Prentice Hall, 2001. ISBN: 9780130815200. URL: https://books.google.dk/books?id=O2eGQgAACAAJ.

[85] *scikit-image: Image processing in Python — scikit-image*. [Online; accessed 2. Jan. 2023]. Dec. 2022. URL: https://scikit-image.org.

[86] David Nečas, Miroslav Valtr, and Petr Klapetek. "How levelling and scan line corrections ruin roughness measurement and how to prevent it." In: *Sci. Rep.* 10 (2020). DOI: 10.1038/s41598-020-72171-8.

[87] Contributors to Wikimedia projects. *Savitzky–Golay filter - Wikipedia*. [Online; accessed 23. May 2022]. Jan. 2022. URL: https://en.wikipedia.org/w/index.php?title=Savitzky-Golay_filter&oldid=1066338331.

[88] Ivan Markov. "Nucleation and step-flow growth in surfactant mediated homoepitaxy with exchange/de-exchange kinetics." In: *Surf. Sci.* 429.1 (June 1999), pp. 102–116. ISSN: 0039-6028. DOI: 10.1016/S0039-6028(99)00342-8.

[89] Y. Nomura, Y. Morishita, S. Goto, Y. Katayama, and T. Isu. "Surface diffusion length of Ga adatoms on (111)B surfaces during molecular beam epitaxy." In: *Appl. Phys. Lett.* 64.9 (Feb. 1994), pp. 1123–1125. ISSN: 0003-6951. DOI: 10.1063/1.110826.

[90] T. L. Einstein. "Equilibrium Shape of Crystals." In: *Handbook of Crystal Growth: Second Edition* 1 (2015), pp. 215–264. DOI: 10.1016/B978-0-444-56369-9.00005-8. arXiv: 1501.02213.

[91] In Won Yeu, Gyuseung Han, Jaehong Park, Cheol Seong Hwang, and Jung-Hae Choi. "Equilibrium crystal shape of GaAs and InAs considering surface vibration and new (111)B reconstruction: ab-initio thermodynamics." In: *Sci. Rep.* 9.1127 (Feb. 2019), pp. 1–9. ISSN: 2045-2322. DOI: 10.1038/s41598-018-37910-y.

[92] Ivan V Markov. *Crystal Growth for Beginners*. 2017. ISBN: 9789813143425. DOI: 10.1142/10127.

[93] C. Y. Fong, M. D. Watson, L. H. Yang, and S. Ciraci. "Surfactant-mediated growth of semiconductor materials." In: *Model. Simul. Mater. Sci. Eng.* 10.5 (Aug. 2002), R61–R77. ISSN: 0965-0393. DOI: 10.1088/0965-0393/10/5/201.

[94] Roy L. M. Op het Veld et al. "In-plane selective area InSb–Al nanowire quantum networks." In: *Commun. Phys.* 3.59 (Mar. 2020), pp. 1–7. ISSN: 2399-3650. DOI: 10.1038/s42005-020-0324-4.

[95] E. Tournié, N. Grandjean, A. Trampert, J. Massies, and K. H. Ploog. "Surfactant-mediated molecular-beam epitaxy of III–V strained-layer heterostructures." In: *J. Cryst. Growth* 150 (May 1995), pp. 460–466. ISSN: 0022-0248. DOI: 10.1016/0022-0248(95)80254-A.

[96] Chan Wuk Oh, Eunja Kim, and Young Hee Lee. "Kinetic Role of a Surfactant in Island Formation." In: *Phys. Rev. Lett.* 76.5 (Jan. 1996), pp. 776–779. ISSN: 1079-7114. DOI: 10.1103/PhysRevLett.76.776.

[97] Filip Krizek, Joachim E Sestoft, Pavel Aseev, Sara Marti-Sanchez, Saulius Vaitiekėnas, Lucas Casparis, Sabbir A Khan, Yu Liu, Tomaš Stankevič, Alexander M Whiticar, et al. "Field effect enhancement in buffered quantum nanowire networks." In: *Physical review materials* 2.9 (2018), p. 093401.

[98] X. Q. Shen and T. Nishinaga. "Inter-surface diffusion of In on (111)A-(001) InAs nonplanar substrates in molecular beam epitaxy." In: *J. Cryst. Growth* 146.1 (Jan. 1995), pp. 374–378. ISSN: 0022-0248. DOI: 10.1016/0022-0248(94)00550-8.

[99] Martin Cachaza. "Selective Area Growth Modes of Semiconductor Networks and Defect Characterization." Doctoral dissertation. University of Copenhagen, 2021. URL: https://nbi.ku.dk/english/theses/phd-theses/martin-espieira-cachaza.

[100] Önder Gül, David J Van Woerkom, Ilse van Weperen, Diana Car, Sébastien R Plissard, Erik PAM Bakkers, and Leo P Kouwenhoven. "Towards High Mobility InSb Nanowire Devices." In: *Nanotechnology* 26.21 (2015), p. 215202.

[101] Aniruddha Konar, John Mathew, Kaushik Nayak, Mohit Bajaj, Rajan K. Pandey, Sajal Dhara, K. V. R. M. Murali, and Mandar M. Deshmukh. "Carrier Transport in High Mobility InAs Nanowire Junctionless Transistors." In: *Nano Lett.* 15.3 (Mar. 2015), pp. 1684–1690. ISSN: 1530-6984. DOI: 10.1021/nl5043165.

[102] T. Bryllert, L.-E. Wernersson, L. E. Froberg, and L. Samuelson. "Vertical high-mobility wrap-gated InAs nanowire transistor." In: *IEEE Electron Device Lett.* 27.5 (May 2006), pp. 323–325. ISSN: 1558-0563. DOI: 10.1109/LED.2006.873371.

[103] Hyunhyub Ko et al. "Ultrathin compound semiconductor on insulator layers for high-performance nanoscale transistors." In: *Nature* 468 (Nov. 2010), pp. 286–289. ISSN: 1476-4687. DOI: 10.1038/nature09541.

[104] Cezar B. Zota, David Lindgren, Lars-Erik Wernersson, and Erik Lind. "Quantized Conduction and High Mobility in Selectively Grown InxGa1–xAs Nanowires." In: *ACS Nano* 9.10 (Oct. 2015), pp. 9892–9897. ISSN: 1936-0851. DOI: 10.1021/acsnano.5b03318.

[105] S. Upadhyay, T. S. Jespersen, M. H. Madsen, P. Krogstrup, and J. Nygård. "Low temperature transport in p-doped InAs nanowires." In: *Appl. Phys. Lett.* 103.16 (Oct. 2013). ISSN: 0003-6951. DOI: 10.1063/1.4825275.

[106] Daria V Beznasyuk, Sara Martí-Sánchez, Jung-Hyun Kang, Rawa Tanta, Mohana Rajpalke, Tomaš Stankevič, Anna Wulff Christensen, Maria Chiara Spadaro, Roberto Bergamaschini, Nikhil N Maka, et al. "Doubling the mobility of InAs/InGaAs selective area grown nanowires." In: *Physical Review Materials* 6.3 (2022), p. 034602.

[107] James L. Webb, Johan Knutsson, Martin Hjort, Sepideh Gorji Ghalamestani, Kimberly A. Dick, Rainer Timm, and Anders Mikkelsen. "Electrical and Surface Properties of InAs/InSb Nanowires Cleaned by Atomic Hydrogen." In: *Nano Lett.* 15.8 (Aug. 2015), pp. 4865–4875. ISSN: 1530-6984. DOI: 10.1021/acs.nanolett.5b00282.

[108] Kristian Storm, Gustav Nylund, Lars Samuelson, and Adam P. Micolich. "Realizing Lateral Wrap-Gated Nanowire FETs: Controlling Gate Length with Chemistry Rather than Lithography." In: *Nano Lett.* 12.1 (Jan. 2012), pp. 1–6. ISSN: 1530-6984. DOI: 10.1021/nl104403g.

[109] Z. Yang, A. Surrente, G. Tutuncuoglu, K. Galkowski, M. Cazaban-Carrazé, F. Amaduzzi, P. Leroux, D. K. Maude, A. Fontcuberta i. Morral, and P. Plochocka. "Revealing Large-Scale Homogeneity and Trace Impurity Sensitivity of GaAs Nanoscale

Membranes." In: *Nano Lett.* 17.5 (May 2017), pp. 2979–2984. ISSN: 1530-6984. DOI: 10.1021/acs.nanolett.7b00257.

[110] Shadi A. Dayeh, David P. R. Aplin, Xiaotian Zhou, Paul K. L. Yu, Edward T. Yu, and Deli Wang. "High electron mobility InAs nanowire field-effect transistors." In: *Small* 3.2 (Feb. 2007), pp. 326–332. ISSN: 1613-6829. DOI: 10.1002/smll.200600379. eprint: 17199246.

[111] Dāgs Olšteins, **Gunjan Nagda**, Damon J. Carrad, Daria V. Beznasiuk, Christian E. N. Petersen, Sara Martí-Sánchez, Jordi Arbiol, and Thomas Sand Jespersen. "***Cryogenic Multiplexing with Bottom-Up Nanowires***." In: *arXiv* (Apr. 2023). DOI: 10.48550/arXiv.2304.12765. eprint: 2304.12765.

[112] AJ Valois, GY Robinson, Kwyro Lee, and MS Shur. "Temperature dependence of the I–V characteristics of modulation-doped FETs." In: *Journal of Vacuum Science & Technology B: Microelectronics Processing and Phenomena* 1.2 (1983), pp. 190–195.

[113] Samuel Poncé, Wenbin Li, Sven Reichardt, and Feliciano Giustino. "First-principles calculations of charge carrier mobility and conductivity in bulk semiconductors and two-dimensional materials." In: *Reports on Progress in Physics* 83.3 (2020), p. 036501.

[114] Nupur Gupta, Yipu Song, Gregory W Holloway, Urbasi Sinha, Chris M Haapamaki, Ray R LaPierre, and Jonathan Baugh. "Temperature-dependent electron mobility in InAs nanowires." In: *Nanotechnology* 24.22 (2013), p. 225202.

[115] Alexander Vasilev, Markus Jech, Alexander Grill, Gerhard Rzepa, Christian Schleich, Stanislav Tyaginov, Alexander Makarov, Gregor Pobegen, Tibor Grasser, and Michael Waltl. "TCAD Modeling of Temperature Activation of the Hysteresis Characteristics of Lateral 4H-SiC MOSFETs." In: *IEEE Transactions on Electron Devices* 69.6 (2022), pp. 3290–3295.

[116] Yang-Kyu Choi, Daewon Ha, Tsu-Jae King, and Chenming Hu. "Threshold voltage shift by quantum confinement in ultra-thin body device." In: *Device Research Conference. Conference Digest (Cat. No.01TH8561)*. IEEE, June 2001, pp. 85–86. ISBN: 978-0-7803-7014. DOI: 10.1109/DRC.2001.937884.

[117] Yu Yuan, Bo Yu, Jooyoung Song, and Yuan Taur. "An analytic model for threshold voltage shift due to quantum confinement in surrounding gate MOSFETs with anisotropic effective mass." In: *Solid-State Electron.* 53.2 (Feb. 2009), pp. 140–144. ISSN: 0038-1101. DOI: 10.1016/j.sse.2008.10.010.

[118] Ralf Granzner, Frank Schwierz, and Vladimir M. Polyakov. "An Analytical Model for the Threshold Voltage Shift Caused by Two-Dimensional Quantum Confinement in Undoped Multiple-

Gate MOSFETs." In: *IEEE Trans. Electron Devices* 54.9 (Aug. 2007), pp. 2562–2565. DOI: 10.1109/TED.2007.902167.

[119] Wei Feng, Chen Peng, Shuang Li, and Xin-Qi Li. "Low-field electron mobility of InSb nanowires: Numerical efforts to larger cross sections." In: *Sci. Rep.* 7.2576 (May 2017), pp. 1–8. ISSN: 2045-2322. DOI: 10.1038/s41598-017-02536-z.

[120] Jared J. Hou, Fengyun Wang, Ning Han, Haoshen Zhu, KitWa Fok, WaiChak Lam, SenPo Yip, TakFu Hung, Joshua E.-Y. Lee, and Johnny C. Ho. "Diameter dependence of electron mobility in InGaAs nanowires." In: *Appl. Phys. Lett.* 102.9 (Mar. 2013), p. 093112. ISSN: 0003-6951. DOI: 10.1063/1.4794414.

[121] Alexandra C. Ford, Johnny C. Ho, Yu-Lun Chueh, Yu-Chih Tseng, Zhiyong Fan, Jing Guo, Jeffrey Bokor, and Ali Javey. "Diameter-Dependent Electron Mobility of InAs Nanowires." In: *Nano Lett.* 9.1 (Jan. 2009), pp. 360–365. ISSN: 1530-6984. DOI: 10.1021/nl803154m.

[122] Michio Kihara, Hajime Fujikura, and Hideki Hasegawa. "Effect of mis-orientation of mesa-stripes on the growth of InGaAs quantum wires by selective molecular beam epitaxy." In: *Appl. Surf. Sci.* 117-118 (June 1997), pp. 695–699. ISSN: 0169-4332. DOI: 10.1016/S0169-4332(97)80166-3.

[123] Miguel J. Carballido, Christoph Kloeffel, Dominik M. Zumbühl, and Daniel Loss. "Low-symmetry nanowire cross-sections for enhanced Dresselhaus spin-orbit interaction." In: *Phys. Rev. B* 103.19 (May 2021), p. 195444. ISSN: 2469-9969. DOI: 10.1103/PhysRevB.103.195444.

[124] J. H. Neave, B. A. Joyce, P. J. Dobson, and N. Norton. "Dynamics of film growth of GaAs by MBE from Rheed observations." In: *Appl. Phys. A* 31.1 (May 1983), pp. 1–8. ISSN: 1432-0630. DOI: 10.1007/BF00617180.

[125] L. Däweritz and R. Hey. "Reconstruction and defect structure of vicinal GaAs(001) and AlxGa1-xAs(001) surfaces during MBE growth." In: *Surf. Sci.* 236.1 (Oct. 1990), pp. 15–22. ISSN: 0039-6028. DOI: 10.1016/0039-6028(90)90756-X.